New model of a thunderstorm downburst and its effect on structures

Auteur : Flament, Clément
Promoteur(s) : Denoel, Vincent; 3900
Faculté : Faculté des Sciences appliquées
Diplôme : Master en ingénieur civil des constructions, à finalité spécialisée en "civil engineering"
Année académique : 2018-2019
URI/URL : http://hdl.handle.net/2268.2/8549

Université de Liège - Politecnico di Milano
Faculty of Applied Science

New model of a thunderstorm downburst and its effect on structures

Graduation work done in order to obtain the Master's degree "Civil Engineer of Constructions" realised by FLAMENT Clément

Academic Supervisors:

Vincent DENOËL (ULiège)
Francesco FOTI (Politecnico di Milano)

Jury:

Thomas ANDRIANNE
Vincent DE VILLE DE GOYET
Luca MARTINELLI

Academic year 2018-2019

Acknowledgements

Firstly, I would like to thanks Politecnico di Milano for giving me the opportunity to realise my thesis there.

Secondly, I want to emphasize that I received a great follow and availability from Professor Luca Martinelli as well as Dr. Francesco Foti. The same could be said of Professor Vincent Denoël in Liège Université. Also, in addition of the great knowledge they shared with me, they showed great interest in the work and regularly discussed with me the potential interesting approaches to follow in my work.

At last, I want to thanks my family and my friends for all the support they brought me during these long months of work as well as during the previous years of study in engineering.

Abstract

Recent history has shown that downburst thunderstorm can be devastating especially for transmission lines composed of towers relied by an electric cable with numerous reported failures of these structures. The literature is very active in the domain of downburst but failed until now to produce a model that predicts the structural response to downburst solicitation. This paper proposes a new approach of downburst modelling based on physical thought and applies it to Andrews A.F.B. downburst event simulation. This model stands on a new decomposition of downburst wind velocity which makes appear a synoptic background wind velocity component to combine with the classic downburst-related velocity component.

In the aim of applying this new model to transmission lines structures in the future, the response of one known case of vertical structure (CAARC building) and one known case of cable structure (iced cable) is studied. The iced cable case is discussed further by simulating different downburst trajectories and a random sampling of the downburst wind field is processed in order to get statistics data from the structural response of the cable such as the correlation coefficients.

Contents

List of Tables

Page

List of Figures

Page

Chapter 3

CHAPTER

1 Introduction

1.1 Description of downburst phenomenon

Downburst thunderstorm is a very localised event first identified by Ted Fujita. Fujita (1990) gives the following definition of a downburst: '*A natural event that occurs due to thunderstorms produced by a cumulonimbus cloud causing a strong downdraft which induces an outburst of damaging winds on or near the ground*'. In other words, this meteorological event is caused by evaporation in a thunderstorm cloud and the consequent rain trains a column of air of negative buoyancy towards the ground with which the impact engenders radial high intensity velocities. The configration of a downburst is represented in FIGURE 1.1 below. Two categories of downbursts can be distinguished based on their size (diameter):

- Macrobursts: diameter larger than 4km.
- Microbursts: diameter smaller than 4km.

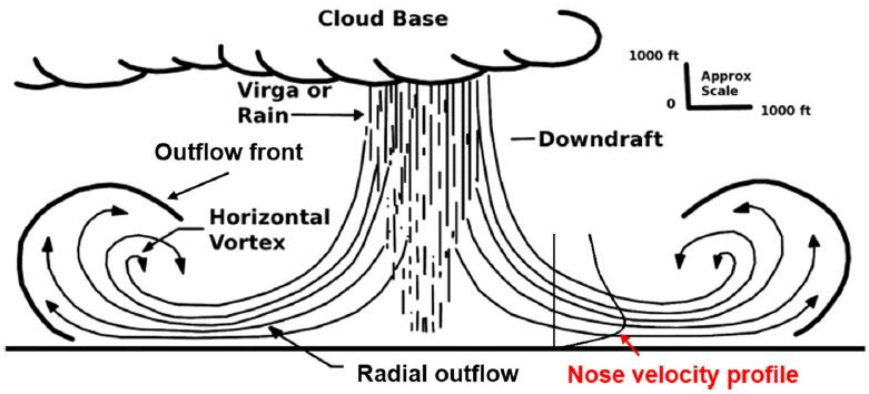

FIGURE 1.1: Scheme of a thunderstorm downburst and nosed velocity profile in the radial outflow, adapted from Solari et al. (2017)

Pictures of microburst outflows are shown in FIGURE 1.2 hereafter.

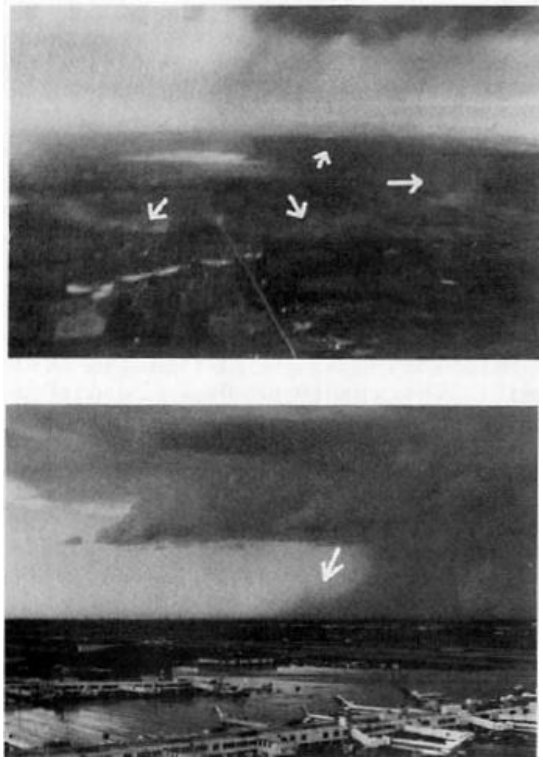

FIGURE 1.2: Photographs of microburst outflows observed in the Denver area, adapted from Hjelmfelt (1987)

1.2 Context

This subject is crucial in recent years as can attest it the numerous articles published on the matter since 1980. The reason of this interest in downburst is that this type of thunderstorm can engender important damages, especially for overhead transmission lines which consists in mid-height slender structures particularly vulnerable to wind loading. As an example, in September 1996, Manitoba Hydro Company reported a failure of 19 transmission towers in Canada due to a downburst thunderstorm occurrence (McCarthy and M, 1996). It was reported in Li (1993) that downburst thunderstorms have engendered more than 90% of the failures linked to weather condition in Australia. Accordingly to Hawes and Dempsey (1993), the transmission lines failures were caused by downburst in 90% of the cases. Also, in China, failures of 18 transmission towers linked to high intensity wind events such as downbursts were reported (Zhang, 1993). Zhang [4]

Due to the transient nature of downburst as well as their very localised occurrence which makes it difficult to capture in the field, it is a challenge to model it with precision in order to predict the response of vulnerable structures such as the electric transmission lines.

1.3 Purposes of the thesis

The first objective of this work is to set an approach of downburst wind field modelling that comes the closest to the one of a real downburst in nature. Next, it is needed to apply the wind

field simulated to a structure keeping in mind that the final goal is to apply it to transmission lines structure composed of towers relied by electric cables. In the present work, the structure of which the responses are studied are a simple vertical cantilever and a cable. Those are based on examples that constitutes known cases that have already been studied in different articles of wind engineering:

- CAARC building for the vertical cantilever (Le and Caracoglia (2017),Alminhana et al. (2018)).
- Iced-Cable for the horizontal cable (Foti and Martinelli (2018b),Foti and Martinelli (2018a)).

These structures are considered as 'flexible'. It is important because they present non-linearity even in their static response (especially for the cable). This fact justifies the use of a non-linear finite element software (Nonda) developed in Politecnico di Milano. Non-linearity that allows to run numerical simulations leading to the response to a downburst solicitation applied to the mesh of the structure.

Finally, based on the structural responses of the cable obtained, statistics of rank 1 and 2 are retrieved from the time histories of the response samples for the cable case in order to identify patterns in the response.

CHAPTER

2 State of the art

The subject of downburst and wind engineering related to it are still at the state of research as can attest it the numerous articles published in recent times on the matter (Solari et al. (2015), Solari et al. (2017), Haines and Taylor (2019),Zhang et al. (2019),...). Downburst are very localised event that happens during a short range of time in addition of their complex behaviour which makes them difficult to be well understood. For those reasons, the response of structures to a downburst event is not defined in norms as opposed to the response to synoptic winds which is well established. In this chapter, some of the approaches of downburst modelling found in the literature are summarised briefly as well as applications of these existing models to a structure. It is worth noting that the following models presented constitute a non exhaustive list of the existing models but are aiming to introduce the main developments made in the downburst modelling.

2.1 Approaches for downburst modelling

Among the various models defining the downburst wind field that can be found in the literature, three important categories of models can be identified:

- Computational fluid dynamics (CFD) based models
- Wind tunnel simulation based models
- Empirical models

These are described in the following.

2.1.1 CFD based models

Numerical models based on CFD has been introduced in order to palliate to the lack of downburst field measurements or the difficulties encountered to obtain them. These models constitutes an alternative way to recreate downburst wind field. Three numerical models can be found in the literature :

- Vortex ring model.

- Cooling source model.
- Impinging jet model.

These models are represented in FIGURE 2.1 and explained below.

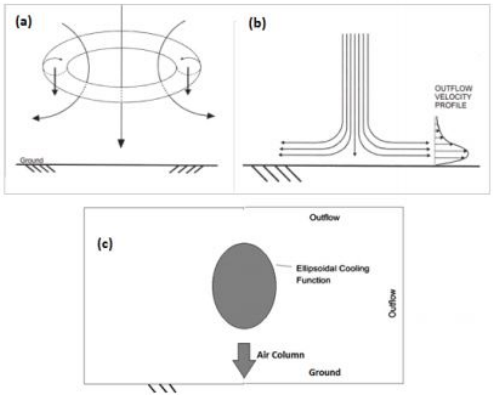

FIGURE 2.1: Representation of: (a) Vortex ring model, (b) Impinging jet model, (c) Cooling source model (Savory 2001 modified from Vermeire et al. (2011).

2.1.1.a) Vortex ring model

The vortex ring model, introduced by **Caracena et al. 1989**, is used to simulate the formation of a ring vortex caused by the downdraft of air and it allows then to explain the formation of a low-pressure ring around the descending column of air. That implies that a vortex ring is surrounding the downdraft circulating downward in the centre of the ring and going upward outside the ring. However, when applied to reproduce downburst thunderstorm, the main drawback of this model is that, according to Savory et al. 2001, it does not represent accurately the wind field of the downburst thunderstorm near the ground after the downdraft hits the ground.

2.1.1.b) Cooling source approach Vermeire et al. (2011)

Selvam and Holmes (1992) Hangan et al. (2003) Mason et al. (2009) Zhang et al. (2013)

This type of CFD model consists in adding a spatial and time dependent forcing function in the energy conservation equation. This function is used as an artificial cooling source that drives the downdraft formed during a downburst thunderstorm. This function is the following:

$$Q(x,y,z,t) = \begin{cases} g(t)\cos^2(\pi R) & for \;\; R \leq 1/2 \\ 0 & for \;\; R > 1/2 \end{cases} \tag{2.1}$$

Where R is a normalised distance from the centre of forcing and g(t) is a time-gradient of temperature. Mason et al. (2009) Zhang et al. (2013) (Anderson et al origin) Representations of the computational domain of the cooling source model of Zhang et al. (2013) as well as the temperature field evolution in time resulting form the numerical simulation based on this model are proposed in FIGURE 2.2 and 2.3 respectively.

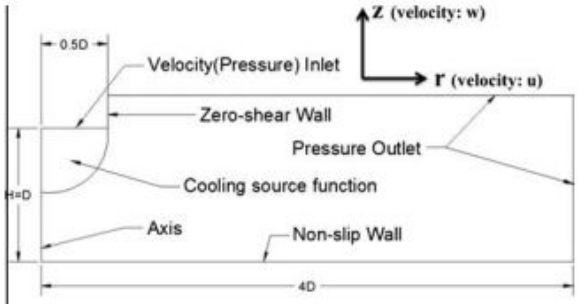

FIGURE 2.2: Computational domain of cooling source model, adapted from Zhang et al. (2013).

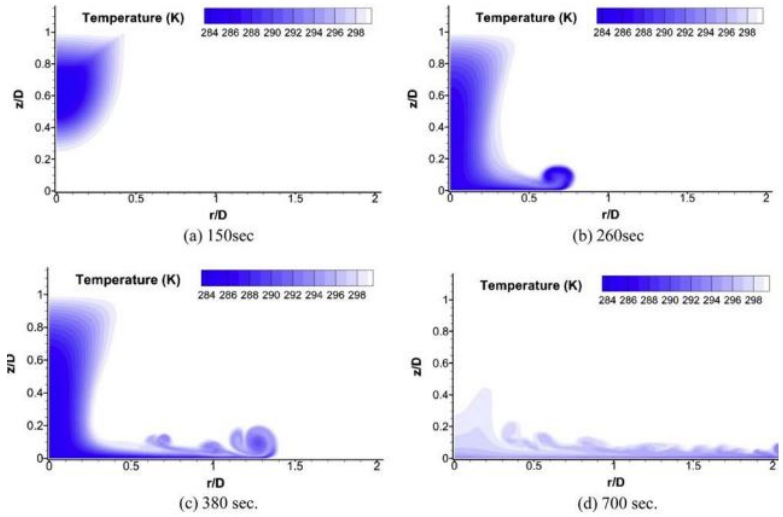

FIGURE 2.3: Evolution of the temperature field in time after numerical simulation based on the cooling source model, adapted from Zhang et al. (2013).

The numerical simulation based on this model uses a large size domain compared to the size of the zone of interest when looking at the interaction between downburst thunderstorm and structure, which results in large time of calculation.

2.1.1.c) Impinging jet model

The idea of an impinging jet model was first brought by Fujita (1985) in which a parallel was made between the downdraft of the downburst and the impact of an impinging jet on a flat surface. By then, Selvam and Holmes (1992) developed a two dimensional steady impinging jet model. However, it did not take into account the transient nature of downburst. After, Holmes and Oliver (2000) used impinging jet model to simulate the radial wind velocities engendered by downburst after the descending air of the downdraft hits the ground. This model is appreciated also for its simplicity and is often found in literature for simulating downburst wind field such as in Zhang et al. (2013) which compares the different CFD based models. Here is a preview of the vertical radial velocity profile of downburst obtained for different CFD models:

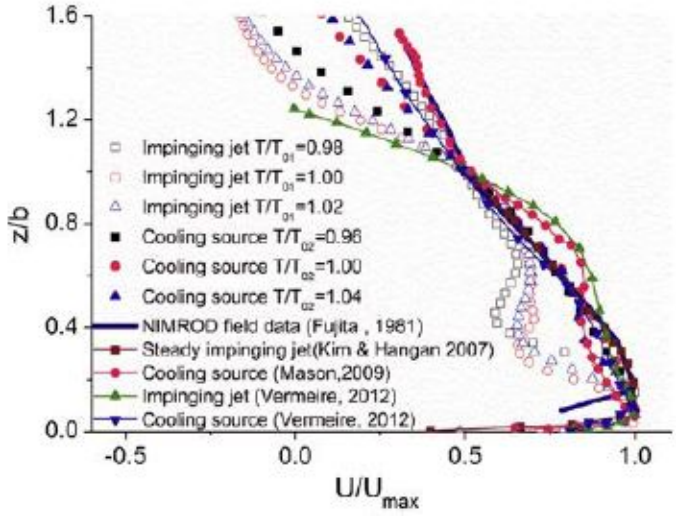

FIGURE 2.4: Comparison of the radial velocity vertical profiles at the vicinity of the maximum velocity time, adapted from Zhang et al. (2013).

2.1.2 Wind tunnel based models

Models based on wind tunnel testing can be considered as "physical" models and these require specific infrastructure in order to reproduce downburst event artificially on large scale as opposed to the simulation of synoptic wind (or boundary layer wind) which is common. In fact, there is only a few of wind tunnel infrastructure that are capable of doing such tests (high wind velocities allowed and full-scale experiments made possible), among them, the Wall of Wind at Florida International University and the Windstorm facility at IBHS. However, the most suitable wind tunnel existing to effectuate downburst testing on structures is the WindEEE (Wind Engineering Energy and Environment) dome situated at Western University of Ontario in Canada (FIGURE 2.5). It consists in a 3D wind testing chamber that allows time-dependence and has an hexagonal shape of 25m diameter surrounded by another hexagon of 40m diameter (Hangan et al. (2017)). The WindEEE dome is composed of 106 fans allowing to differ the wind direction and wind velocity for suitability.

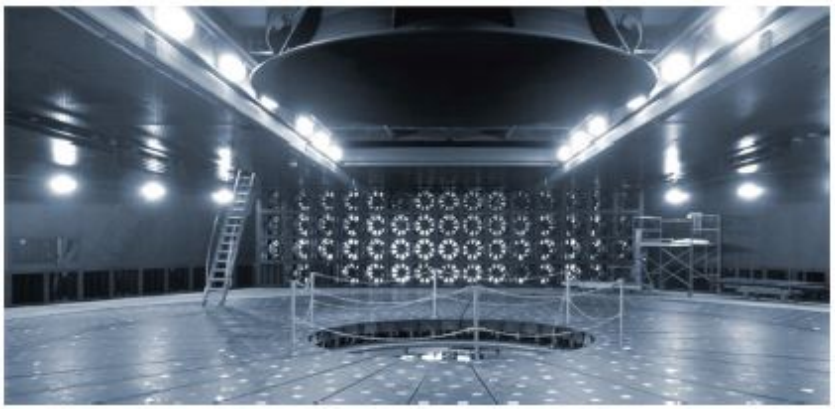

FIGURE 2.5: Insight of the inner chamber of WindEEE dome, adapted from Hangan et al. (2017).

2.1.3 Empirical models

Empirical models are, by definition, models that are validated through comparison with example of real experiments or events. Here are some examples of meaningful examples of empirical models applied to downburst that can be found in the literature.

2.1.3.a) Holmes and Oliver 2000

The model they implemented is combining the downburst speed of displacement in the horizontal plane and the radial velocity generated by the downburst thunderstorm itself and is focused only on the horizontal velocity component. It was aiming to simulate the Andrews Air Force Base downburst event that happened in 1983 in Maryland.

In this model, the definition of the radial velocity is based on the impinging jet theory that has been validated through comparison with the measurements of radial velocity made by Hjelmfelt (1987) when experimenting an impinging jet as it can be seen on FIGURE 2.6. The formula of radial velocity derived from an axisymmetric impinging jet is the following for a given height (5m in the case of Andrews A.F.B. wind velocity recordings):

$$V_r = \begin{cases} V_{r,max}(r/r_{max}) & for \;\; r < r_{max} \\ V_{r,max}\left[\exp -\left(\frac{r-r_{max}}{R}\right)^2\right] & for \;\; r \geq r_{max} \end{cases} \tag{2.2}$$

Where r is the radial distance from the centre of the thunderstorm downburst, , V_{max} is the maximum radial velocity, r_{max} is the radial distance corresponding to the maximum radial wind velocity and R is a radial scale taken approximatively equal to $r_{max}/2$ in FIGURE 2.6. In order to simulate a real downburst event, the formula above is modulated by an exponential time decay function ($\exp -t/T$) where t is the time and T is a time constant to define in such a way that it approaches the velocity time history of Andrews A.F.B. event. A more detailed description of this radial velocity distribution is given further in this work.

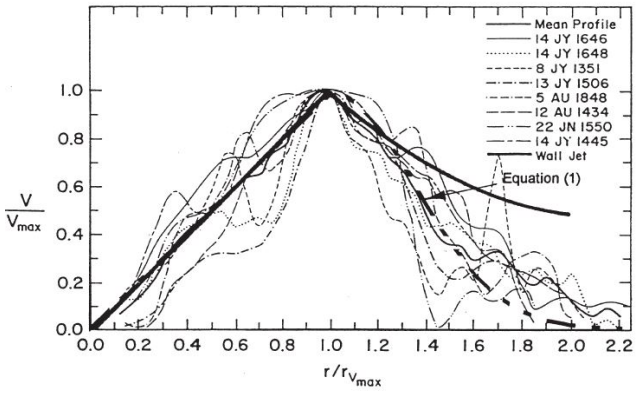

FIGURE 2.6: Comparison between the radial velocity profiles from Hjelmfelt experiments (Hjelmfelt (1987)) and the impinging jet formula (noted Equation (1) on the graph) , adapted from Holmes and Oliver (2000).

For the simulation of the Andrews A.F.B. event, the value of the translation speed was set as a parameter and then chosen by trial and error (12 m/s) to approach the better recordings of this same event. In any case, this value constitutes a non-negligible part of the maximum gust velocity measured at observation stations (Bankstown and Mascot, both situated in the region of Sydney) as it can be seen on TABLE 2.1.

Storm translation speeds

Date	Time (and value) of max. gust at Bankstown	Time (and value) of max. gust at Mascot	Translation speed (m/s) from gust times	Upper level wind speed (m/s)
29/3/1975	15.35 EST (24.7 m/s)	15.53 EST (28.8 m/s)	17	11
23/11/1975	17.45 EDT (26.7m/s)	18.00 EDT (42.2m/s)	20	12
21/1/1977	16.07 EDT (34.5 m/s)	16.25 EDT (25.7 m/s)	16	15

TABLE 2.1: Summary of data collected in the region of Sydney for three downburst events and estimation of the translation speed for the very same events, adapted from Holmes and Oliver (2000).

Then, the model combines the speed of translation and the radial velocity as a vector summation. This means that a point of observation positioned on the downburst thunderstorm trajectory is submitted to a change of horizontal wind velocity orientation of 180°. However, the observer is generally off the downburst path and in this case the change of wind velocity orientation at this point is less 180°. This change of wind orientation explained the difference between the horiaontal wind velocity peaks on FIGURES 2.7 (a) and (b). Indeed, for the second peak, the translation velocity vector is oriented in an opposite direction to the one of the radial velocity.

The horizontal wind velocity time history generated by the empirical model of Holmes and Oliver matches reasonably with the wind velocity history data from the Andrews Air Force Base (Andrews A.F.B.) downburst event that happened in 1983, as it is shown in FIGURE 2.7. It is important to note that this model is based on the maximum horizontal velocity and therefore it does not take into account the variation of the horizontal wind velocity along the height from ground level (vertical profile).

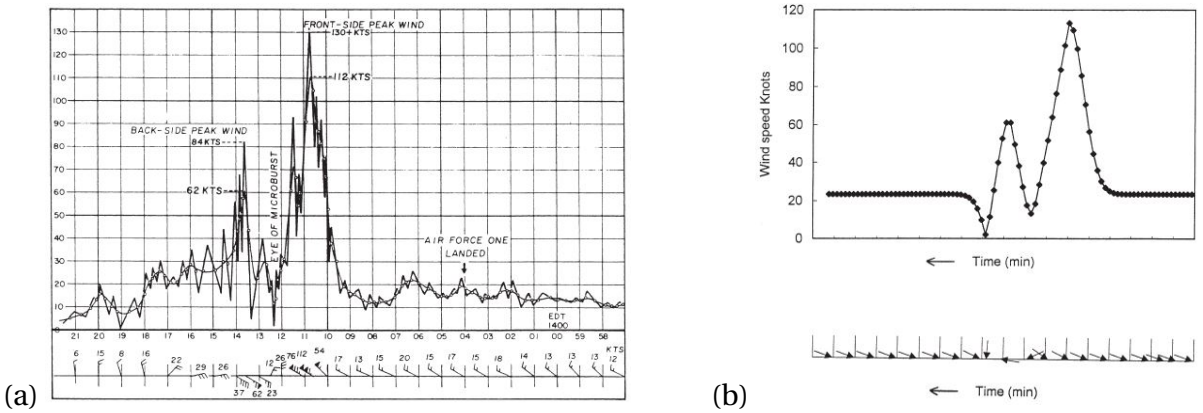

(a) (b)

FIGURE 2.7: Horizontal wind velocity and orientation time history: (a) recorded from Andrews A.F.B. downburst event with the time axis going from right to left, (b) simulated with Holmes and Oliver model for Andrews A.F.B. downburst event (Holmes and Oliver, 2000).

2.1.3.b) Chen and Letchford 2004

In Chen and Letchford (2004a), an empirical model aiming to simulate the wind velocities related to downburst thunderstorm event (i.e. Andrews A.F.B. event in this case) was brought. This model consists in the decomposition of the horizontal wind velocity generated by a downburst thunderstorm into a deterministic mean part and a stochastic fluctuating part, such that the wind velocity at height z and time t generated can be obtained as:

$$U(z,t) = \overline{U}(z,t) + u(z,t) \tag{2.3}$$

Where $\overline{U}(z,t)$ the moving average mean wind velocity set as deterministic and $u(z,t)$ the fluctuating term of the wind velocity determined by zero mean stochastic process assumed to be a Gaussian. As it can be seen in FIGURE 2.7 page 9, the downburst wind velocity is a non-stationary process. The same can be said concerning the rapidly time-varying wind velocity that remains when removing the mean component of the time history. To represent the slowly time-varying mean wind velocity $\overline{U}(z,t)$, a maximum mean wind speed vertical profile noted as V(z) is modulated by a time function with a maximum value of 1 which is assumed to be achieved when the wind velocity reaches its maximum value. It can be written as:

$$\overline{U}(z,t) = f(t)V(z) \tag{2.4}$$

The vertical profile V(z) used above can be evaluated either by three existing empirical models:

- Oseguera and Bowles 1988.
- Vicroy 1992.
- Wood and Kwok 1998.

The formulae of these models are detailed further in this work and a comparison of these laws is shown on FIGURE 2.8 with parameters chosen to generate the same maximum radial wind velocity V_{max} ($80 m/s$).

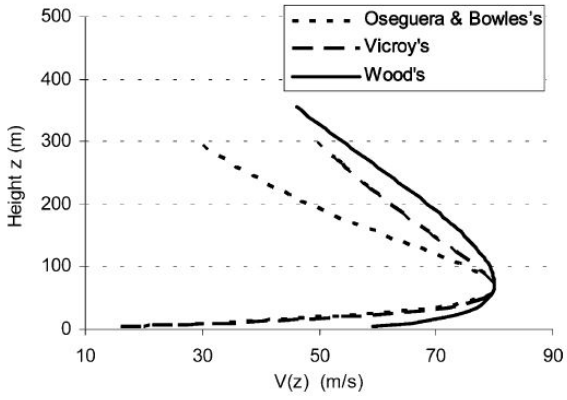

FIGURE 2.8: Comparison of models of vertical wind velocity profiles, adapted from Chen and Letchford (2004a).

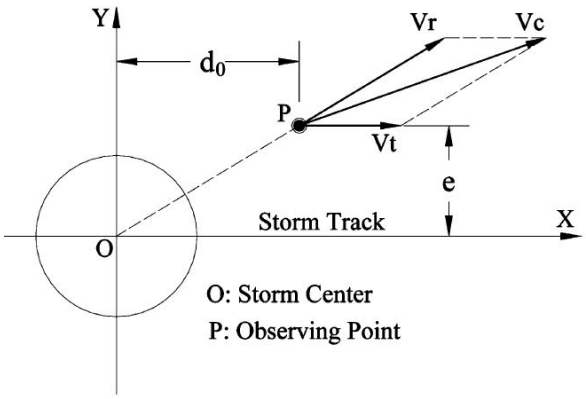

FIGURE 2.9: Vector combination of wind velocities related to downburst, adapted from Chen and Letchford (2004a).

Then the simulation is proceeded as in the model of Holmes and Oliver presented above, i.e. the impinging jet model is used to formulate the radial wind velocity vector ($\underline{V}_r(t)$) which is summed with a time-constant translation velocity vector ($\underline{V}_t$) to obtain the resultant wind velocity vector($\underline{V}_c(t)$) as it can be seen on FIGURE 2.9. The time function f(t) is then defined as:

$$f(t) = \frac{|\underline{V}_c(t)|}{max|\underline{V}_c(t)|} \tag{2.5}$$

The time function and the resultant wind velocity time history are shown in FIGURE 2.10.

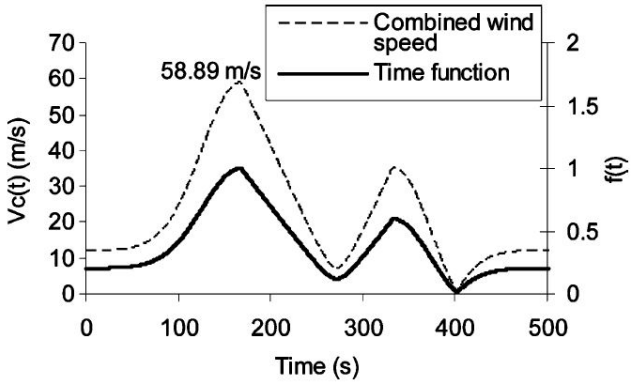

FIGURE 2.10: Example of simulated resultant wind velocity and time function time history, adapted from Chen and Letchford (2004a).

An add-on compared to the model of Holmes and Oliver leads in the definition of a stochastic fluctuating wind velocity term assumed to be Gaussian. In this model, this term is assessed through the fluctuations evolutionary power spectral density function (EPSD).

2.1.3.c) Solari et al. (2017)

Solari et al. (2017) also uses the classic transient downburst wind velocity decomposition into a slowly time-varying mean velocity and a turbulence velocity. In this model, the turbulence and the mean velocity are modelled by the intermediate of modulating functions, evaluated from real downburst wind data recordings. The turbulence velocity v' and the slowly time-varying mean wind $\overline{v}$ velocity are expressed respectively as:

$$v'(z,t) = \sigma_v(z,t)\overline{v}'(z,t) \tag{2.6}$$

$$\overline{v}(z,t) = \overline{v_{max}}\alpha(z)\gamma(t) \tag{2.7}$$

Where σ_v is the slowly-varying standard deviation of the turbulence velocity, $\overline{v}'$ is the reduced turbulent fluctuation assumed to be a zero mean stationary Gaussian random process, $\overline{v_{max}}$ is the maximum value of mean velocity in the simulation duration, $\gamma(t)$ is a non-dimensional time modulating function with maximum value of 1 representing the time variation of $\overline{v}$ and $\alpha(z)$ is a non-dimensional spatial (height) modulating function with maximum value of 1 determining the vertical profile of $\overline{v}$.

Introducing the slowly-varying turbulence intensity as:

$$I_v(z,t) = \frac{\sigma_v(z,t)}{\overline{v}(z,t)} = \overline{I_v}(h)\beta(z)\mu(t) \tag{2.8}$$

Where h is the reference height, β is a non-dimensional spatial (height) modulating function with maximum value of 1 determining the vertical profile of I_v and μ is is a non-dimensional time modulating function with maximum value of 1 responsible of time variation of I_v.

Finally, the total wind velocity generated by downburst can be rewritten as:

$$v(z,t) = \overline{v_{max}}\alpha(z)\gamma(t)\left(1 + \overline{I_v}(h)\beta(z)\mu(t)\overline{v}'(z,t)\right) \tag{2.9}$$

The modulating time function $\gamma(t)$ and $\mu(t)$ are determined by the intermediate of downburst wind recordings as it is shown on FIGURE 2.11 below.

Difficulties encountered with this model are due to the dependence on suitable downburst recordings data.

2.2 Applications of downburst models: Response of structures

Once the downburst wind field is created, it is needed to apply it on a structure as a load to evaluate the response of a structure to such a solicitation. The main problem that can be identified in the search of structural response to downburst is that the wind field of downburst is a non-stationary process as can attest the rapid variations of wind velocity in a short period of time (cfr. FIGURE 2.7 page 9), on the contrary of a synoptic wind field. That non-stationarity changes

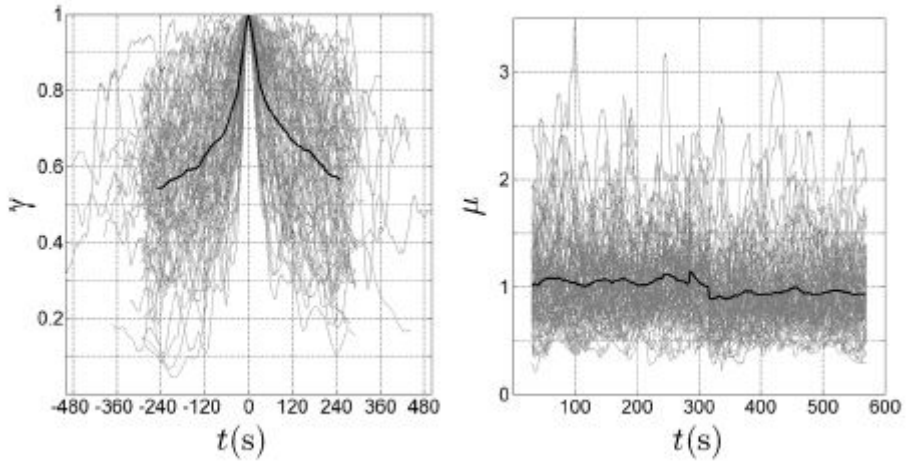

FIGURE 2.11: Time histories of $\gamma(t)$ and $\mu(t)$ for all set of recordings and their mean value in black font, adapted from Solari et al. (2017).

the loading applied to the structure and therefore it makes the structural response more complex and show that there is interest in developing models to predict the response of a structure to a downburst thunderstorm solicitation. Then, various potential approaches to respond to that problematic has been studied in the literature of which some are presented below in this section.

2.2.1 Gust-Front factor approach

(Kwon and Kareem, 2009)

In this approach, a formulation of the downburst wind field similar to which of a synoptic wind is employed in order to keep a relatively simple formulation. The approach adopted is based on the gust loading factor. This factor allows to adapt the existing procedure (dedicated to synoptic wind) to gust-front winds whiwh can be produced during a downburst event and has the advantage of being used in the existing norms such as ASCE (2005). The design wind load F_{design} resulting from gust-front winds is evaluated by simply apply the following formula:

$$F_{design} = K_{z,G-F} G_{G-F} F_{ASCE7} \tag{2.10}$$

Where F_{ASCE7} is the wind load recommended by ASCE (2005) for synoptic winds, $K_{z,G-F}$ is a coefficient accounting for the vertical wind velocity profile difference and G_{G-F} is the gust-front factor to pass from synoptic winds load to gust-front winds load. This gust-front factor can be divided into four underlying coefficients with physical meaning (Kwon and Kareem, 2007):

$$G_{G-F} = I_1 I_2 I_3 I_4 \tag{2.11}$$

Where I_1 represents the kinematics effects factor, I_2 is the pulse dynamics factor , I_3 is the structural dynamics factor and I_4 is the load modification factor. All these factors represents the part of various effects which are presented below:

- I_1 accounts for the mean loads effects induced by the difference between the vertical velocity profile of gust-front winds and the one of synoptic winds.

- I_2 represents the effect of the quick variations of wind velocity in a finite period of time which are not present in boundary layer winds. This coefficients depend on several parameters such as the duration of the pulse, the natural period of the structure considered and the damping coefficient.
- I_3 states for the effects of turbulence in itself, meaning the buffeting effects on structure mainly due to non-stationarity of the longitudinal wind.
- I_4 is responsible for the change in aerodynamics that are caused by the fluctuations of wind directions in gust-front winds. Indeed, the drag coefficient is affected by those changes of wind direction and then diverges from the drag coefficient of synoptic winds.

The FIGURE 2.12 below illustrates the fact that in practice the design wind load based on gust factor method corresponds to the wind load related to gust-front winds only for a limited range of heights. Indeed, the shape of the boundary layer winds (i.e. synoptic winds) loading profile is such that it is more critical than the gust-front winds loading profile for heights near the ground as well as in high altitude.

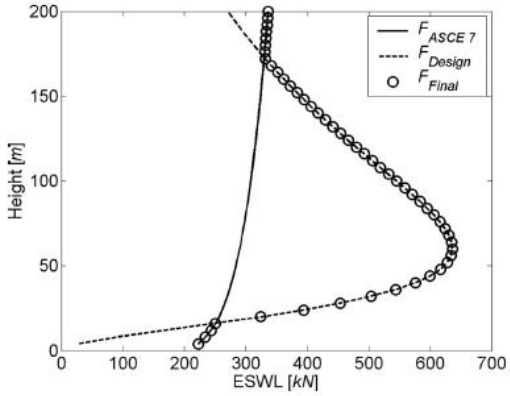

FIGURE 2.12: Practical consideration of the design wind loading in a gust front (F_{design}), adapted from Kwon and Kareem (2009).

2.2.2 Semi-analytical approach

(Canor et al., 2016)

Canor et al. (2016) brings an alternative to the generation of numerous samples of wind field in order to get some statistics to evaluate the structural response to transient solicitation: the use of perturbation method in the evolutionary spectral analysis valid for structures submitted to transient random loads and allows to look at the structural response in the frequencies domain. In order to proceed to the evolutionary spectral analysis in the modal basis, which is preferred, the modal impulse matrix must be computed. To achieve it, the matrix is computed by the intermediate of an asymptotic approximation that will allow to see the modal coupling as a perturbation of the decoupled standard modal basis. This asymptotic extension combined with recurrence relation leads to an approximation of the modal evolutionary transfer matrix. Knowing that in wind engineering non-linearity is everywhere, the Gaussian equivalent linearization is used to make the system LTI and convenient for analysing the structural response.

CHAPTER

3 New model of downburst wind generation

In this chapter, a new wind velocity generation model is first described in a general way and then applied to the case of the Andrews Air Force Base downburst event in 1983, because it is a well known case during which wind measurements have been proceeded by anemometer (Fujita, 1985) and it has been often used as a reference case for downburst modelling in the past and recent years, for example by Holmes and Oliver (2000), Chen and Letchford (2004a) and Le and Caracoglia (2017). Therefore, there is a strong database and simulations done concerning this event. The actual records of the Andrews A.F.B. event wind velocities are shown in FIGURE 3.1 page 15.

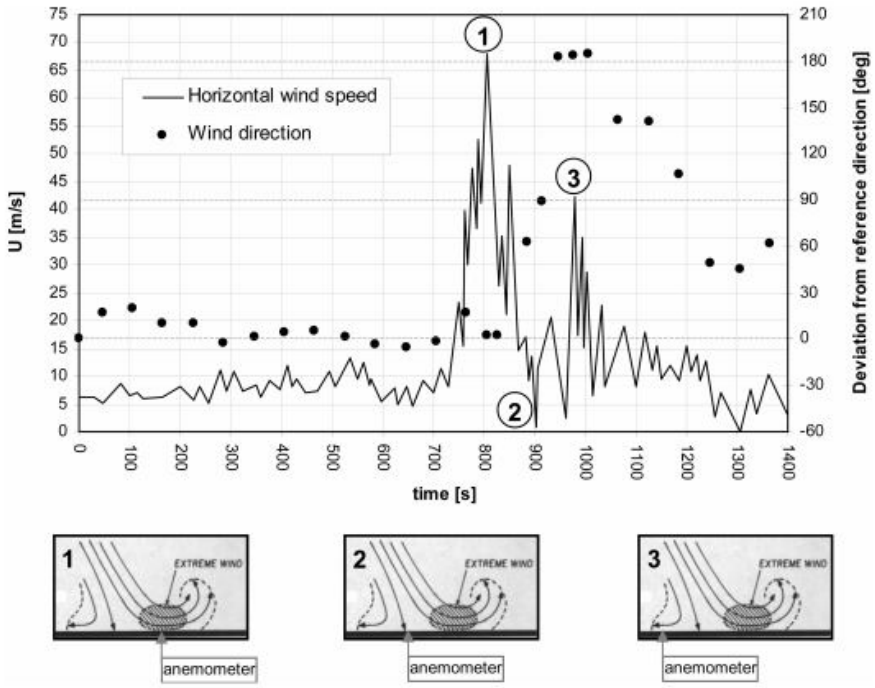

FIGURE 3.1: Velocity history at 4.9 m AGL for a severe outflow (1 Aug 1983, Andrews AFB downburst data from Fujita 1985 and diagrams adapted from Wakimoto 2001), adapted from Lin et al. (2007).

Finally, a parametric study is performed on the basis of the parameters that reproduces at best the Andrews A.F.B. downburst in order to understand what are the factors of influence in a downburst event while keeping in mind that the wind generation is a loading to be applied on structures.

3.1 Definition of reference systems

Before getting into the details of the wind velocity generated during a downburst event, reference systems needs to be set in order to define the relative distance between the downburst and one reference point called as the observer point. Those reference systems are defined in a way that gives the most global vision possible of the evolution over time of the wind velocity created during a thunderstorm downburst event with respect to an observer point that is fixed over time.

The various reference systems in which the wind velocity components can be written are described in the FIGURE 3.2 page 16.

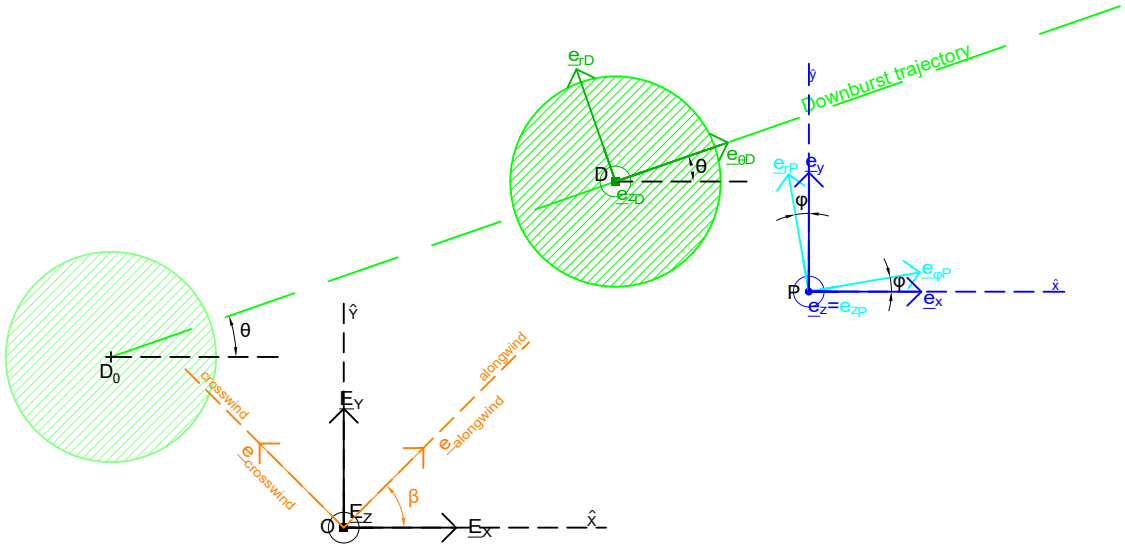

FIGURE 3.2: Reference systems in the $X-Y$ plane (horizontal).

The global reference system is represented by the origin point O and the axes X, Y and Z associated to the basis of orthogonal unit vectors $\{\underline{E}_X, \underline{E}_Y, \underline{E}_Z\}$ whereas the local reference system of the observer is defined by the the position of the observer point P as origin, the basis of orthogonal unit vectors $\{\underline{e}_{\phi P}, \underline{e}_{rP}, \underline{e}_{zP} = \underline{e}_z\}$ and the angle ϕ between unit vectors $\underline{E}_x$ and $\underline{e}_{\phi P}$. That angle ϕ However, note that in this work the angle ϕ is taken equal to 0° so that the local reference system of the observer matches the one defined by point P as origin and the axes x, y and z oriented along the orthoginal basis of unit vectors $\{e_x, e_y, e_z\}$. The downburst position at each time is characterised by the position of its eye and is written $D(t)$ at instant time t while D_0 represent the initial position of the downburst. A local reference system of the downburst is also defined,

using point D as origin, and a set of axis corresponding to the basis of orthogonal unit vectors $\{\underline{e}_{\theta D}, \underline{e}_{rD}, \underline{e}_{zD} = \underline{E}_Z\}$ and θ the angle between unit vectors $\underline{E}_x$ and $\underline{e}_{\theta D}$, defining the direction of the downburst trajectory. Finally, a background wind reference system is created by rotating the global reference system around the Z axis with an angle β. The background wind is part of the environment within which a downburst event occurs and has the properties of a synoptic wind. This notion is more detailed in SECTION 3.2 and particularly in SUBSECTION 3.2.1 page 18. This new reference system uses the set of orthogonal unit vectors $\{\underline{e}_{alongwind}, \underline{e}_{crosswind}, \underline{E}_Z\}$ as a basis and the vectors $\underline{e}_{alongwind}$ and $\underline{e}_{crosswind}$ define respectively the alongwind and crosswind directions also detailed in SUBSECTION 3.2.1 page 18.

3.2 Decomposition of horizontal wind velocity generated during a downburst event

Holmes and Oliver (2000) proposed that the wind velocity in one point of observation results in the vector summation of one translation velocity component that constitutes the velocity in the initial environment where the downburst appears at some time, and a radial velocity component directly downburst-related coming from an impinging jet and modulated in time. Then, Chen and Letchford (2004a) updated the decomposition of Holmes and Oliver by adding the turbulence velocity component downburst-related. This is the appearance of the deterministic-stochastic decomposition, with the resultant wind velocity consisting in a vector sum of a slowly-varying mean velocity (due to unsteadiness of a thunderstorm downburst) and a zero-mean rapidly-varying velocity linked to turbulence. This last term is evaluated as a "uniformly modulated evolutionary vector stochastic process" assuming that this fluctuating velocity is Gaussian and associating it to a PSD and coherence function. The vector writing of the total wind velocity in a downburst event according to this standard decomposition is the following:

$$\underline{V}(r,z,t) = \overline{\underline{V}}(r,z,t) + \underline{V'}(r,z,t) \tag{3.1}$$

With

$$\overline{\underline{V}}(r,z,t) = \underline{V_r}(r,z,t) + \underline{V_t}$$

Then, knowing that the mean velocity component is not constant over time unlike in the case of a synoptic wind, the influence of the thunderstorm downburst can be seen clearly. The literature from 21^{st} century (Chen and Letchford (2004a),Solari et al. (2015),Solari et al. (2017),Le and Caracoglia (2017),...) are going to that sense by defining a downburst-related mean component varying over time ($\overline{\underline{V}}(z,t)$) combined with the time-constant translation velocity linked to the displacement of the Downburst over time ($\underline{V_t}$) and a fluctuating turbulent term downburst-related ($\underline{v}'(z,t)$), as it is shown in vector equation 3.1 above. Nevertheless, it can be thought that the translation velocity is related to a synoptic wind happening in the background of the downburst event. Indeed, looking at the mean wind velocity vertical profile (along axis Z), that thinking makes sense because it brings a vertical profile with a logarithmic profile over the height when the thunderstorm downburst is far away from the observer point instead of a vertical profile that is constant over the height. Such a vertical profile is indeed not close to a real wind distribution over height simply because the wind velocity is decreasing over height when it get closer to the soil surface due to its roughness, cfr. the boundary layer theory. In addition of the mean velocity

component, a turbulence component is brought by the synoptic wind in background. Therefore, the turbulence component is no longer only defined by the radial turbulence due to the downburst but also by a turbulence wind velocity component associated with the synoptic wind happening in background of the downburst. Following the proposition of wind decomposition exposed above, the wind velocity components involved in a downburst occurrence are detailed hereafter in SUBSECTIONS 3.2.1, 3.2.2 and 3.2.3. The chart of FIGURE 3.3 page 18 sums up the different vector velocity component that are part of the new decomposition of wind velocity during a downburst event, also written in the vector equations 3.2a, 3.2b and 3.2c below.

$$\underline{V}_r(r,z,t) = \underline{V}_{backg}(z,t) + \underline{V}_r(r,z,t) \tag{3.2a}$$

With

$$\underline{V}_{backg}(z,t) = \overline{\underline{V}}_{backg}(z) + \underline{V'}_{backg}(z,t) \tag{3.2b}$$

$$\underline{V}_r(r,z,t) = \overline{\underline{V}}_r(r,z,t) + \underline{V'}_r(r,z,t) \tag{3.2c}$$

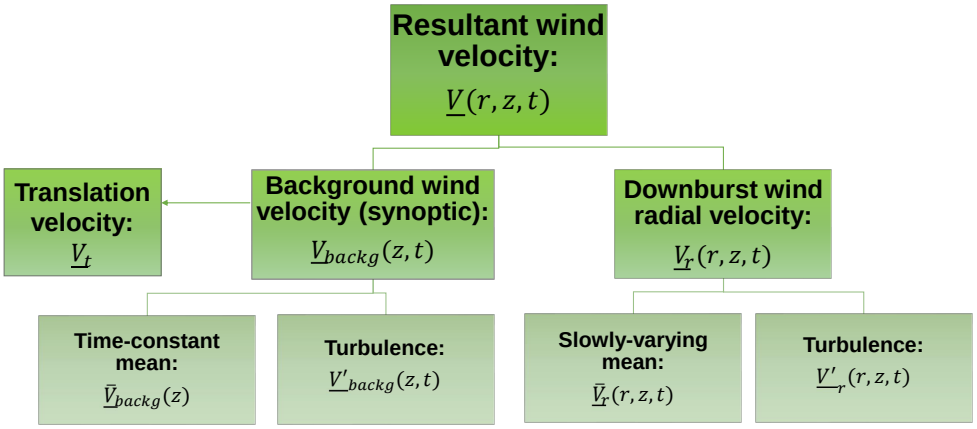

FIGURE 3.3: Organisational chart of the new wind velocity decomposition for downburst thunderstorm modelling.

3.2.1 Background wind related component

The background wind consists in a synoptic wind composed by both mean and turbulence wind velocity components. For such a type of wind generated wind velocities, it makes sense to define the alongwind and crosswind directions, which represent respectively the direction of the gust wind and the corresponding perpendicular one. It should be precised that the alongwind direction is time-varying and does not necessarily match with the direction of the downburst trajectory, which brings to the definition of a new set of axes by the intermediate of the angle β, see FIGURE 3.2 page 16 where the background wind reference system is represented. Nevertheless, in the following developments made in this work, the angle β will correspond to the angle θ

indicating the direction of the downburst displacement for sake of clarity in the analyses of the results.

3.2.1.a) Mean velocity $\overline{V}_{backg}$

The mean velocity of the background wind that is assumed to be a synoptic wind in this new wind model, is defined by norms in the part of the Eurocode dedicated to wind actions (EN 1991-1-4) based on a logarithmic profile function of the height z and depending on roughness parameters of the environment. According to EN 1991-1-4 §4.3, the equation 3.3a below represents the background wind mean velocity $\overline{V}_{backg}$, defined in the alongwind direction (no crosswind component).

$$\overline{V}_{backg}(z) = c_r(z)c_o(z)V_b \tag{3.3a}$$

$$\text{With} \begin{cases} c_r(z) = k_r \ln \dfrac{z_{min}}{z_0} & \text{for } z \leq z_{min} \\ c_r(z) = k_r \ln \dfrac{z}{z_0} & \text{for } z > z_{min} \end{cases} \tag{3.3b}$$

Where $c_r(z)$ is the roughness factor, $c_o(z)$ is the orography factor defined in EN 1991-1-4, §4.3.3 , z_0 and z_{min} are respectively the roughness length and the minimum height of the logarithmic profile both function of the exposure class of the terrain given in EN 1991-1-4, Table 4.1. The terrain factor k_r is defined in EN 1991-1-4, §4.3.3 depending on exposure class and roughness length. Finally, according to EN 1991-1-4, §4.2, V_b represents the basic wind velocity, i.e. the 10 minutes mean wind velocity at 10 m above ground surface for an terrain exposure class II (low vegetation and isolated obstacles). Still following EN 1991-1-4, §4.2, this value of V_b has to be modified by a probability factor c_{prob} depending on the return period to be considered, the basic values being estimated for a mean return period of 50 years. Note that the definition of this mean synoptic wind in EN 1991-1-4 is referenced for extreme winds and the fact that there is very low probability for such values of wind and downburst event to happen simultaneously has to be kept in mind, especially when modelling the downburst of Andrews A.F.B. in SECTION 3.3. The values of parameters defining the mean synoptic wind velocity for the Andrews A.F.B. example of downburst are listed in TABLE 3.1 page 27.

The synoptic wind velocity vertical profile is illustrated in the FIGURE 3.4 below for different exposure classes according to Table 4.1 in EN 1991-1-4 or CNR DT 207-2008, i.e. for different roughness level of the site. The roughness level is greater as the number of exposure class is high.

3.2.1.b) Turbulence velocity $\underline{V'}_{backg}$

The first important fact concerning the turbulence of a synoptic wind is that, by opposition with the synoptic mean wind velocity that is defined in 3.2.1.a) page 19 in the single alongwind direction, the turbulence of the synoptic wind is generated in every space direction (three-dimensional) and then is the only influence in the crosswind direction of the general background velocity component.

The turbulence is defined as a zero mean fluctuating term of the general synoptic wind speed around a mean synoptic wind such as in equation 3.2b page 18. In case of synoptic wind, it is

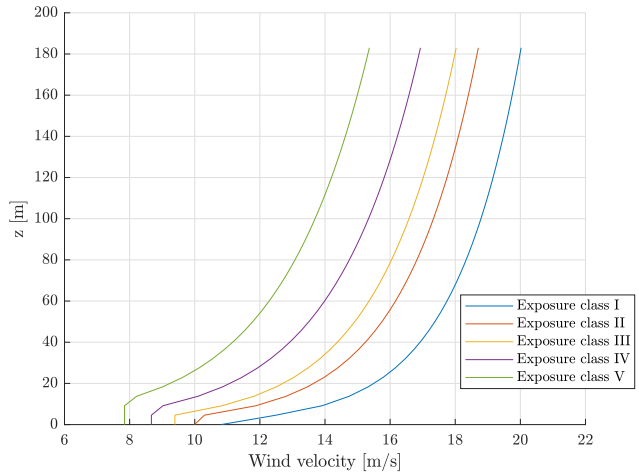

FIGURE 3.4: Background wind mean velocity vertical profile for different exposure classes.

represented by a 3-D stationary Gaussian random process of which the properties over time and space are described by means of the cross-power spectral density functions (CPSDF). Solari and Piccardo (2001) developed a three-dimensional unified model for synoptic wind turbulence in the case of a flat homogeneous terrain and neutral atmospheric conditions on the basis of the work of Solari (1987). In this manner, the model proposed is adapted to the response of all types of structure that are gust-excited in the three-dimensional space such as high-rise buildings and bridges or cable structures. This model is followed in this work in order to generate the CPSDF of synoptic wind turbulence. The approach made bySolari and Piccardo (2001) is described in the following.

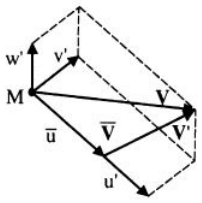

FIGURE 3.5: Wind velocity field, modified from Solari and Piccardo (2001).

The mean wind velocity $\underline{\overline{V}}$ and the turbulence wind velocity $\underline{V'}$ at point M are respectively defined as the following vectors:

$$\underline{\overline{V}}_{backg}(M) = \overline{u}(z)\underline{e}_{alongwind} \tag{3.4a}$$

$$\underline{V'}_{backg}(M) = u'(M,t)\underline{e}_{alongwind} + v'(M,t)\underline{e}_{crosswind} + w'(M,t)\underline{e}_{z} \tag{3.4b}$$

Where $\overline{u}(z)$ is the mean wind velocity in alongwind direction and u', v' and w' represent respectively the alongwind, crosswind and vertical component of the turbulence wind velocity.

The CPSDF that contain the properties of the components of turbulence velocity $\varepsilon'(M,t)$ and $\eta'(M',t)$ is described as in the equation 3.5 below:

$$S_{\varepsilon,\eta}(M,M';n) = \sqrt{S_\varepsilon(z;n)S_\eta(z';n)}\,coh_{\varepsilon\eta}(M,M';n) \quad \text{with } \varepsilon,\eta = u,v,w \tag{3.5}$$

Where M' is a point in space with coordinates x',y' and z';$S_\varepsilon(z;n) = S_{\varepsilon\varepsilon}(M,M;n)$ is the power spectral density function (PSDF) of turbulence velocity component $\varepsilon'(M,t)$; $coh_{\varepsilon,\eta}(M,M';n)$ is the coherence function (COHF) of turbulence velocity components $\varepsilon'(M,t)$ and $\eta'(M',t)$;n is the frequency. The COHF $coh_{\varepsilon,\eta}(M,M';n)$ is defined as following:

$$coh_{\varepsilon\eta}(M,M';n) = sign(\Gamma_{\varepsilon\eta})\sqrt{\Gamma_{\varepsilon\eta}(z;n)\Gamma_{\varepsilon\eta}(z';n)}\sqrt{\Lambda_\varepsilon(M,M';n)\Lambda_\eta(M,M';n)} \tag{3.6a}$$

$$\Gamma_{\varepsilon\eta}(z;n) = coh_{\varepsilon\eta}(M,M;n) \tag{3.6b}$$

$$\Lambda_\varepsilon(M,M';n) = coh_{\varepsilon\varepsilon}(M,M';n) \tag{3.6c}$$

In which $\Gamma_{\varepsilon\eta}$ represents the point COHF of different turbulence components situated at the same position; Λ_ε is the space COHF of the same turbulence component established at different positions in space. The expression of the CPSDF taken in its entirety (equations 3.5, 3.6b and 3.6c) highlights the fact that the 3-D turbulence of synoptic wind is governed by the following three functions: the PSDF $S_\varepsilon(z;n)$, the point COHF $\Gamma_{\varepsilon\eta}$ and the space COHF Λ_ε. The PSDF as well as the space COHF is defined for $\varepsilon = u,v,w$ and the point COHF is described for turbulent components combinations such as $\varepsilon \neq \eta$, i.e. for the combinations uv, uw and vw.

- **Power spectral density functions**:

  Starting from the equations of power spectral density functions developed on the basis of the experiments made by Von Karman (1948) and from the variance σ_ε^2 definition (Eq. 3.8), a PSDF estimation equation in the inertial subrange is derived as below taking advantage of the theory of the energy cascade:

$$\frac{nS_\varepsilon(z;n)}{\sigma_\varepsilon^2} = \frac{d_\varepsilon nL_\varepsilon(z)/\overline{u}(z)}{\left(1+1.5d_\varepsilon nL_\varepsilon(z)/\overline{u}(z)\right)^{5/3}} \tag{3.7}$$

  Where $d_u = 6.868, d_v = d_w = 9.434$.

$$\sigma_\varepsilon^2 = \beta_\varepsilon u_*^2 \tag{3.8}$$

  Where u_* is the shear velocity and β_ε the non-dimensional turbulence intensity factor. Its mean value in the alongwind direction has been computed on the basis of experimental measurements at ground level and neutral atmospheric conditions for different values of roughness length:

$$\beta_u = 6 - 1.1\arctan(\ln z_0 + 1.75) \tag{3.9}$$

- **Point coherence functions**:

$$\Gamma_{uw}(z;n) = -\frac{1}{\kappa_{uw}}\frac{1}{\sqrt{1+0.4\left(nL_u(z)/\overline{u}(z)\right)^2}} \tag{3.10}$$

$$\kappa_{uw}(z) = A_{uw}\sqrt{\beta_u(z)\beta_w(z)} \tag{3.11}$$

$$A_{uw}(z) = 1.11\,[L_w(z)/L_u(z)]^{0.21} \tag{3.12}$$

- **Space coherence functions**:

$$\Lambda_\varepsilon(M, M'; n) = \exp\left\{-\frac{2n\sqrt{\sum_r C_{r\varepsilon}^2 |r - r'|^2}}{\overline{u}(z) + \overline{u}(z')}\right\} \tag{3.13}$$

  Where $C_{r\varepsilon}$ is an exponential decay coefficient of the turbulence component $\varepsilon' = u', v', w'$ in direction r=x,y,z. The values of this coefficient are evaluated following the Tabella E.I of CNRDT207 and are exposed hereafter in a matrix:

$$C_r = \left\{\begin{array}{ccc} 3 & 10 & 10 \\ 3 & 6.5 & 6.5 \\ 0.5 & 6.5 & 3 \end{array}\right\} \tag{3.14}$$

Having defined the PSD of the background turbulence, it still remains to determine a method to generate the random samples of turbulence. For this purpose, the Di Paola and Gullo (2001) article proposes the following random generation process.

The PSD matrix is decomposed into the orthonormal basis of its eigenvectors, such that we have:

$$\underline{\underline{S_V}}(w) = \underline{\underline{\psi}}(w)\underline{\underline{\Lambda}}(w)\underline{\underline{\psi}}(w)^T \tag{3.15}$$

In the basis of the eigenvectors of PSD matrix $\underline{\underline{S_V}}$, the n-variate process $\underline{V}(t)$ can be decomposed into a sum of n n-variate fully correlated independent vectors $\underline{Y}(t)$:

$$\underline{\underline{V}}(t) = \sum \underline{\underline{Y}}(t) \tag{3.16}$$

And finally those vectors can be rewritten by a combination of sinusoïds (cfr. Shinozuka and Deodatis (1991):

$$Y_j(t) = 2\sum \psi_j(w_k)\sqrt{\Lambda_j(w)\Delta w}(cos(w_k t R_k{}^{(j)} - sin(w_k t I_k{}^{(j)} \tag{3.17}$$

3.2.2 Thunderstorm downburst related component

3.2.2.a) Mean velocity $\overline{V}_r$

The estimation of the wind velocity due to the downburst itself is made by means of the "impinging wall jet" empirical model of Holmes and Oliver (2000) derived from the experiment of Hjelmfelt (1987) which has given proof that the mean velocity profiles coming from experiment in a laboratory and and its computation were close to match with the ones that has been found in thunderstorm downburst event (Hjelmfelt (1987)). The impinging jet consists in an vertical jet of fluid that hits the ground which generates a radial outflow. It is considered as a axisymmetric

jet. In the radial plane of the downburst, two different regions must be distinguished in such a model, based on the radial distance from the centre of the jet impact (i.e. the downburst eye) on the ground :

- The stagnation region, governed by the following equation :

$$f_r(r) = r/r_{max} \quad for \;\; r < r_{max} \tag{3.18}$$

- The diverging region, governed by the following equation :

$$f_r(r) = \exp\left\{-\left(\frac{r - r_{max}}{r^*}\right)^2\right\} \quad for \;\; r \geq r_{max} \tag{3.19}$$

Note that by definition $f_r \in \{0;1\}$ and can be seen as an intensification function in space (radial plane more precisely) and the radial mean wind velocity in the downburst is given by :

$$\overline{V_r} = f_r(r) V_{r,max} \tag{3.20}$$

Where $V_{r,max}$ is the maximum radial velocity at a fixed height z_{max}.

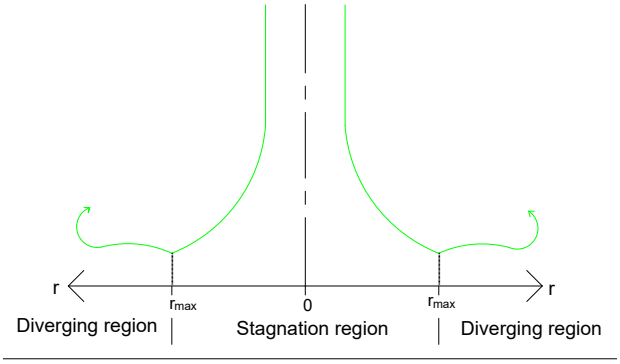

FIGURE 3.6: Radial regions induced by impinging jet model.

The parameters used in the equations 3.18 and 3.19 above are summarised in TABLE 3.1 page 27 which gives their values corresponding to the Andrews A.F.B. downburst estimation.

As mentioned above, the value of the mean radial velocity computed thanks to the equations 3.18 page 23 and 3.19 page 23 is estimated at a given height corresponding to the maximum radial velocity happening. This leads to the definition of the vertical profile (along Z) of mean velocity for a downburst, of which the maximum radial velocity $V_{r,max}$ is part. Three solutions has been established in the past for V_z profile estimation:

- Oseguera and Bowles (1988):

$$\overline{V}_z = \lambda \frac{R^2}{2 * r}(1 - exp(-((r/R)^2)))[exp(-z/z^*) - exp(-z/e)] \tag{3.21}$$

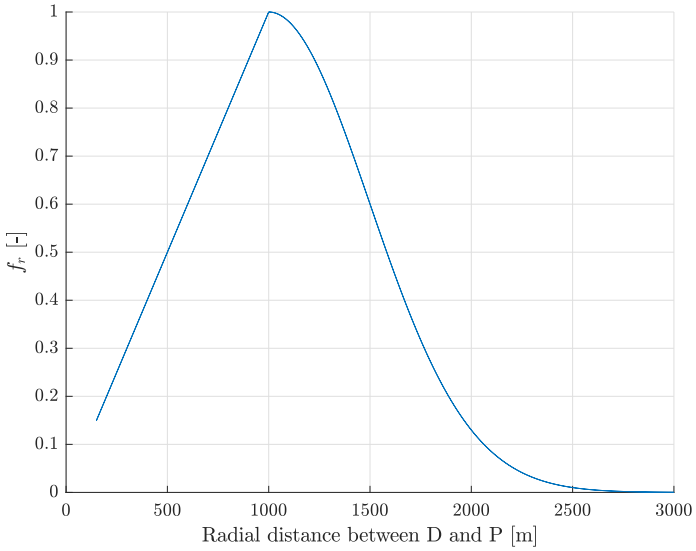

FIGURE 3.7: Spatial intensification function with respect to radial distance from the downburst r.

- Vicroy (1998):

$$\overline{V}_z = 1,22 V_{r,max}(\exp(-0.15 z/z_{max}) - exp(-3.2175 z/z_{max})) \tag{3.22}$$

- Wood and Kwok (1998):

$$\overline{V}z = 1,55((z/\delta)^{(1/6)})(1 - erf(0.7 z/\delta)) V_{r,max} \tag{3.23}$$

The parameters used in the equations 3.21, 3.22 and 3.2.2.a) above are summarised in TABLE 3.1 page 27 which gives their values corresponding to the Andrews A.F.B. downburst estimation.

In this work, the Wood law is chosen to be in accordance with Le and Caracoglia (2017). By the way, some of the results obtained with the model presented in this article are compared with the ones resulting from the new model in SECTION 3.3 page 27.

By combining the impinging jet model for radial profile and the Wood and Kwok's law for vertical profile, a mean radial velocity $\overline{V}_r(z,r)$ is obtained but corresponds to a "frozen" state of the downburst in time when its intensity is maximum ($V_{r,max}$). Therefore the definition of a time intensification function f_t is introduced to be able to model the decay in time of the downburst. This function has been evaluated by Le and Caracoglia (2017) and is given by the following equation:

$$\begin{aligned} f_t(t) &= t/t_0 \quad when t < t_0 \\ f_t(t) &= \exp(-\frac{t - t_0}{T}) \quad when t_0 \leq t \leq T \end{aligned} \tag{3.24}$$

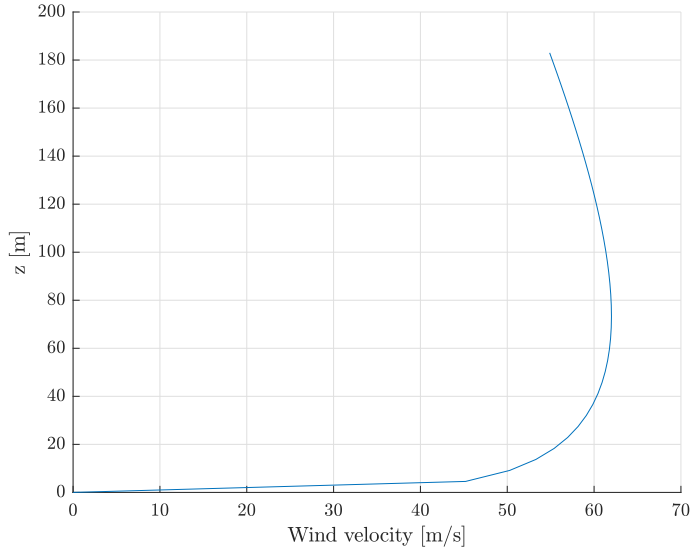

FIGURE 3.8: Vertical radial velocity profile.

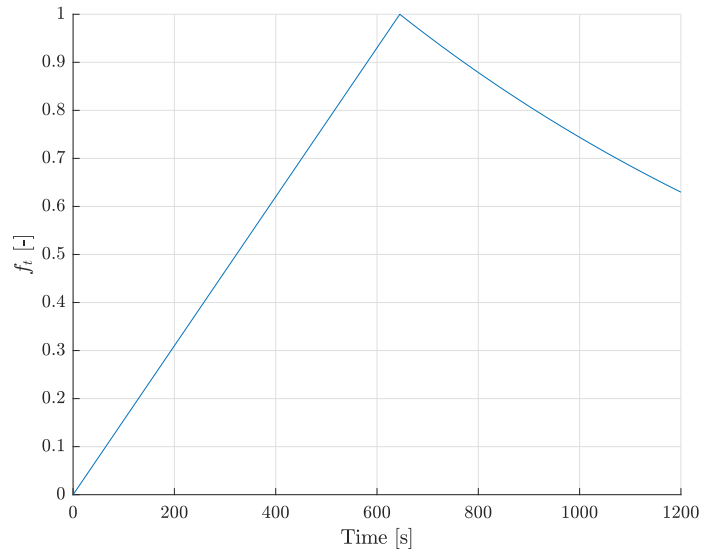

FIGURE 3.9: Time intensification function with respect to time t.

Where t represent a time instant in seconds (> 0) and the other parameter T representing the simulation duration is given in TABLE 3.1 page 27. It is worth noting that by definition: $f_t \in \{0;1\}$.

Finally, the slowly time-varying mean radial wind velocity can be computed by bringing all together the spatial intensification function derived from the impinging jet model, the law giving the vertical profile of the mean radial velocity V_z and the time intensification function:

$$\overline{V}_r(t,r,z) = f_t(t)\, f_r(r)\, V_z(z) \tag{3.25}$$

3.2.2.b) Turbulence velocity $\underline{V'}_r$

On the contrary of the synoptic turbulence, the downburst-related turbulence is a non-stationary random process.

By contrast with the turbulence related to a synoptic wind, the downburst related turbulence velocity component has not been yet well modelled in the existing literature. Therefore, it is still a subject of study in the field of downburst wind loading as there is some recent papers such as Haines and Taylor (2019) that are looking for discussing the modelling of the fluctuating part of the downburst wind velocity. In fact, this could change the conclusions on the structure response because of the potential meeting of much higher frequencies than the ones of the flexible structures studied in this work (low natural frequencies). However, in order to still model this turbulence and get the best simulation of the Andrews A.F.B. downburst, some approach already used in different papers can be employed: take the unsteady turbulence velocity as a Gaussian evaluated by evolutionary spectral process, choosing the PSD following the one measured in experiment of impinging jet in Haines and Taylor (2019) and generating random samples thanks to the Di Paola and Gullo (2001) method presented above. A comparison of the PSD of turbulence during Haines and Taylor (2019) experiment and various attempts to approach it is illustrated on FIGURE 3.10.

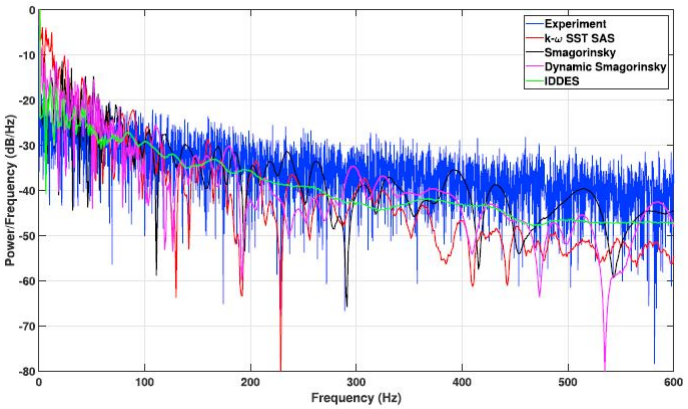

FIGURE 3.10: A comparison of the power spectral density of the experimentally measured and simulated velocity 0,5 m below the inlet region (individual run turbulence levels), adapted from Haines and Taylor (2019).

It is important to note that this essential turbulence velocity component is not included in the wind model developed in this work. Nevertheless, it is a perspective of further development of the new approach of downburst modelling presented here and could well lead to an improvement in reproducing the wind velocities generated in a thunderstorm downburst.

3.2.3 Downburst trajectory related velocity

The downburst trajectory related velocity vector $\underline{V}_t$ is only used in order to establish the trajectory of the downburst or more precisely its eye, happening in the $X-Y$ 2D plane only. Its direction is defined by the constant angle θ (cfr. FIGURE 3.2 page 16). This angle is considered as

a time-constant throughout the movement for convenience and can be evaluated thanks to the available experimental data of the downburst event chosen to be reproduced. However, in this work, it is set as a parameter of the problem in order to see the effect of a change of downburst trajectory on the wind velocities applied to the structure as well as its response to those corresponding wind loads, as it is discussed further. In parallel, the downburst trajectory velocity is also considered as a time-constant for the same reason and can be determined for one particular downburst event by means of the time spent between wind velocity peaks in the velocity history of this event (cfr. FIGURE 3.1 page 15), knowing the distance between those peaks. Nevertheless, it is again set as a parameter for the need of a parametric study. (SECTION 3.4).

3.3 Validation: Case of Andrews A.F.B. downburst event

The wind generation model developed in SECTION 3.2 need to be validated. For this purpose, the model will be applied to a real example of downburst event: The Andrews A.F.B. downburst event. The choice of this example has been driven by the fact that a lot of studies have been applied to it and thus the wind recording data is available as well as models of this event. It allows to compare the results of the new model with the ones produced with the wind model developed in Le and Caracoglia (2017) for the Andrews A.F.B. downburst.

3.3.1 Parameters

The TABLE 3.1 page 27 offers a summary of the values of the parameters used in the downburst wind model. That constitutes the first set of parameters which represents the set of reference for the parametric study of SECTION 3.4. This set of parameters is dedicated to the rproduction in simulation of the Andrews A.F.B. downburst event.

Parameters [units]	Values	Parameters [units]	Values
Duration of simulation T $[s]$	1200	Translation velocity V_t $[m/s]$	12
Time step Δt $[s]$	0.2	Radius related to maximum wind speed r_{max} $[m]$	1000
Reference velocity V_b $[m/s]$	10	Radial length scale r^* $[m]$	700
Topography factor c_t $[-]$	1	Characteristic time t_0 $[s]$	645
Terrain factor k_r $[-]$	0.19	Maximum mean radial velocity $V_{r,max}$ $[m/s]$	62
Roughness length z_0 $[m]$	0.05	Height where the velocity is half its maximumδ $[m]$	400
Minimum height z_{min} $[m]$	4		

TABLE 3.1: Summary of parameters and their values used to estimate wind velocity of Andrews A.F.B. downburst event.

3.3.2 Results

FIGURES 3.11 (a) and (b) below shows that the slowly time-varying mean wind velocity is well reproduced by the model implemented for the example of Andrews A.F.B. downburst and presents a similar shape of the one performed by the model of Le and Caracoglia (2017). However, looking at the turbulence wind velocity, it can be said that it is not well captured by the model which is not surprising giving the fact that the radial turbulence is not implemented in this work (FIGURE 3.11 (c)). Indeed, the amplitude of velocity fluctuation of the synoptic wind turbulence does not change much through time as opposed to the turbulence of the Andrews A.F.B. real downburst that shows two peaks of amplitude variation at the same period of time corresponding to the apparition of the wind velocity peaks (i.e. downburst passage).

Concerning the turbulence, it appears at first that the turbulence generated in the alongwind direction has a high content of very low frequencies that is taking over the content of the other frequencies as is it shown by the red curve in FIGURE 3.12 (a) page 30. This observation is confirmed by looking at the PSD of the alongwind turbulence still by the red curve in FIGURE 3.12 (b) page 30. In order to remove the content in very low frequencies, the PSD is modified. This modification consists in removing the area of the PSD situated before a certain cut-off frequency f_{cut} and to add it with the area starting from f_{cut} and which has the same size of frequency range than the area removed, in such a way that the variance is not changed by the operation. The chosen cut-off frequency equals to 0.0377 Hz in such a way that the PSD values in the range of the 10 first frequencies evaluated are removed and has been determined by a trial and error method. This procedure is summarised in the FIGURE 3.15 hereafter.

Even though their very low frequency content is not taking precedence over the other frequencies content as it can be seen on FIGURE 3.12 (c), (d), (e) and (f) page 30, the PSD modification is applied the same way to the crosswind and vertical turbulent velocities to be consistent with the PSD of the alongwind turbulent velocities.

Being placed in the observer point local axes, the FIGURE 3.13 page 31 highlights that the resultant wind velocity is reduced in norm after the downburst passage, for an identical radial distance between the eye of the downburst and the observer point P.

During the passage of downburst, not only the wind velocity norm is changing over time but also the wind direction with respect to the point of observation, as can attest the FIGURE 3.14. This figure illustrates that the new model represents relatively well the evolution of the wind direction in time and is close to the estimation given by the model of Le and Caracoglia (2017). A change of maximum 180 °is observed at the time of the downburst passage that can easily be understood by looking at FIGURE 3.13 representing the velocity vectors at two time instants of the downburst passage from an observer point of view.

Concerning the vertical profile of wind velocity, the implementation of the new model offers a vertical profile of which the shapes is time-changing, depending on the position of the downburst relative to the observation point. In fact, that makes more sense because the type of wind that affects the observation time is different when the downburst is there or not and an evolution in time should reasonably be seen. The results of the new model approach are compared

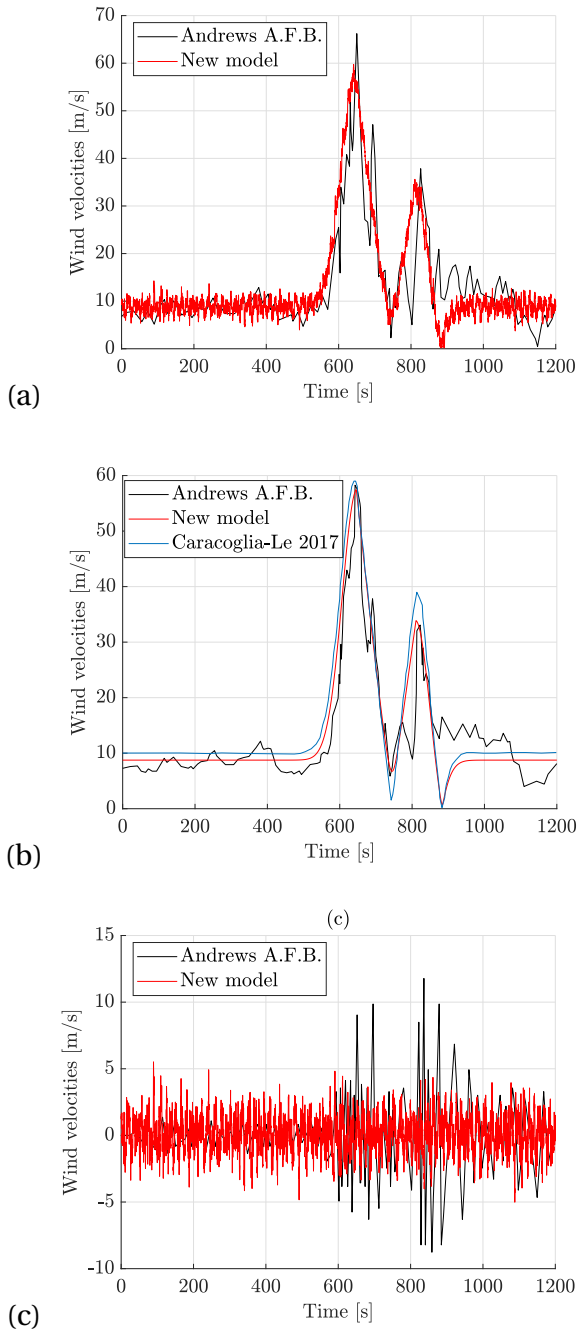

FIGURE 3.11: Andrews A.F.B. downburst velocities time histories: (a) Resultant wind velocity time history, (b) Mean wind velocity time history, (c) Turbulent velocity time history.

in the FIGURE 3.16 with the one produced by a standard wind velocity decomposition as well as for a combination of time-constant translation velocity with the vertical velocity profile law. For a standard decomposition, the vertical profile shape is the same whatever the time instant considered but is modulated by the time function in order to emphasise the increase of wind velocity due to the downburst passage. In the approach composed by the vertical profile law and

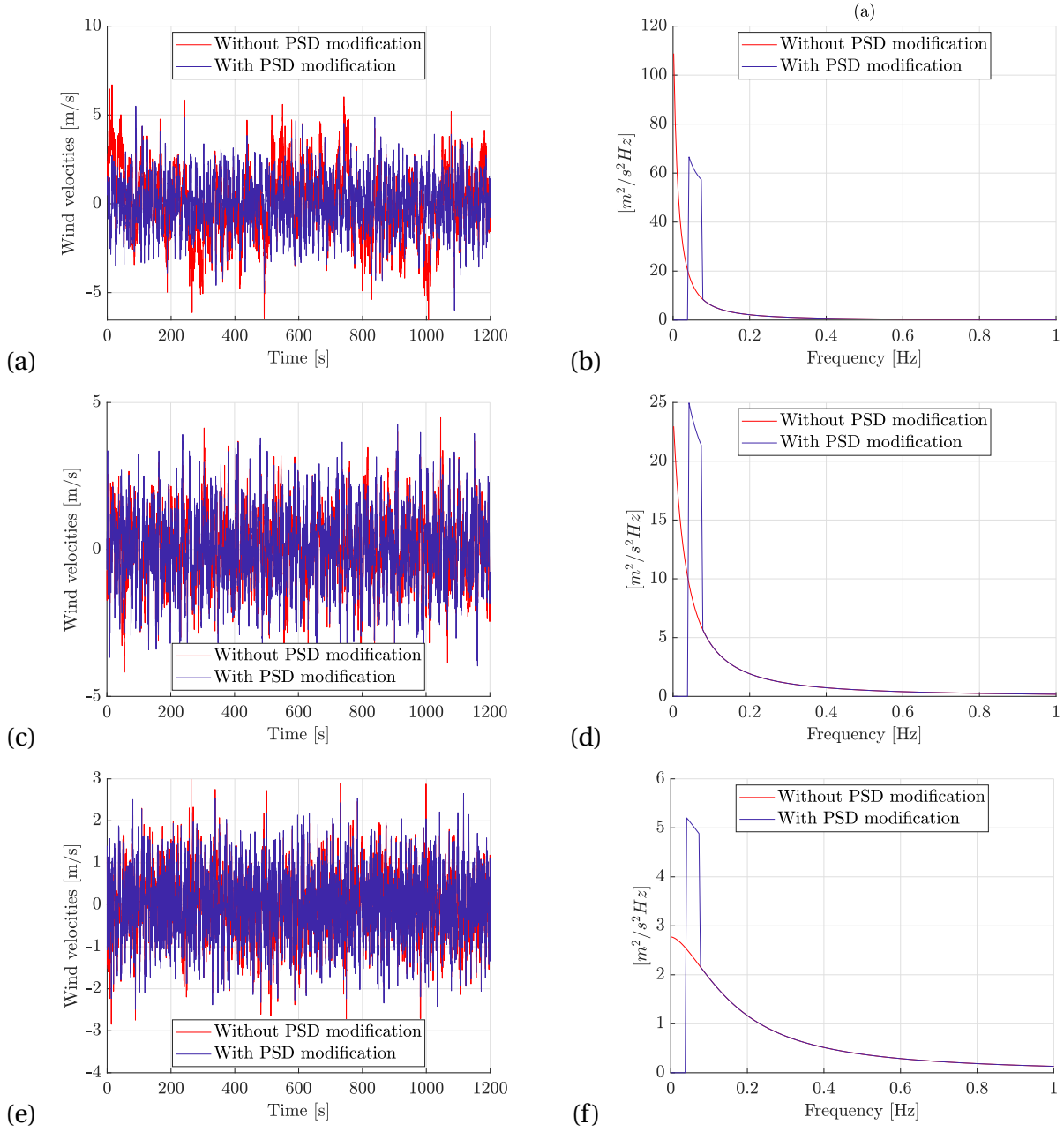

FIGURE 3.12: Turbulent velocities of the Andrews downburst generated using the new model of downburst wind generation and their respective PSD with or without modification of the PSD: (a) Alongwind turbulent velocities, (b) Alongwind turbulence PSD, (c) Crosswind turbulent velocities, (d) Crosswind turbulence PSD, (e) Vertical (Z axis) turbulent velocities, (f) Vertical (Z axis) turbulence PSD.

the translation velocity, the change of shape is visible because when the downburst is not influencing the wind velocity in the observation point, the vertical profile of radial velocity related to downburst is set close to zero which makes more physical sense that with the standard approach. This modification of the shape is even more materialised by the new decomposition that is proposed in this work because of the synoptic wind profile that can be seen appearing when the doownburst is too far from the observer, considering only a synoptic wind profileif there is no downburst thunderstorm and a combination of the vertical profile law for downburst wind with

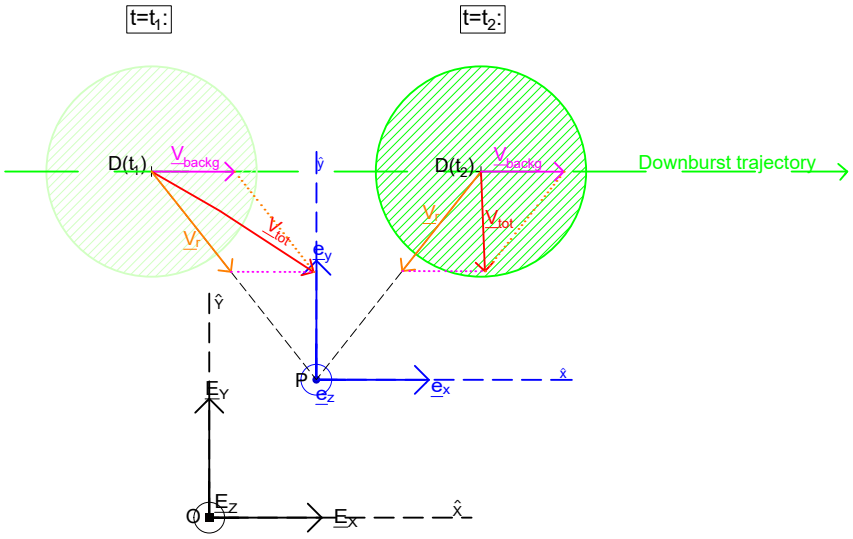

FIGURE 3.13: Scheme of the evolution in time of the resultant horizontal velocity vector.

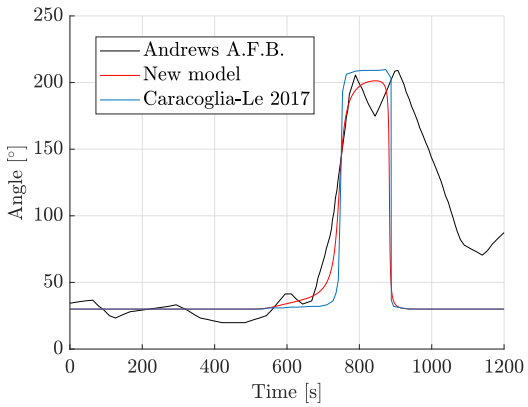

FIGURE 3.14: Andrews A.F.B. downburst mean wind direction time history.

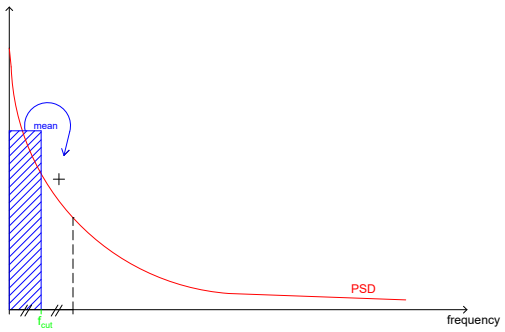

FIGURE 3.15: Modification of the PSD to remove the very low frequency content.

the background synoptic wind when downburst is close enough to the observer. Note that the difference of time-evolution of the vertical profile between the two approaches is more pronounced as the height considered is higher and the vertical downburst related wind profile is more nosed, i.e. as z_{max} is smaller (cfr. FIGURE 3.16 page 32).

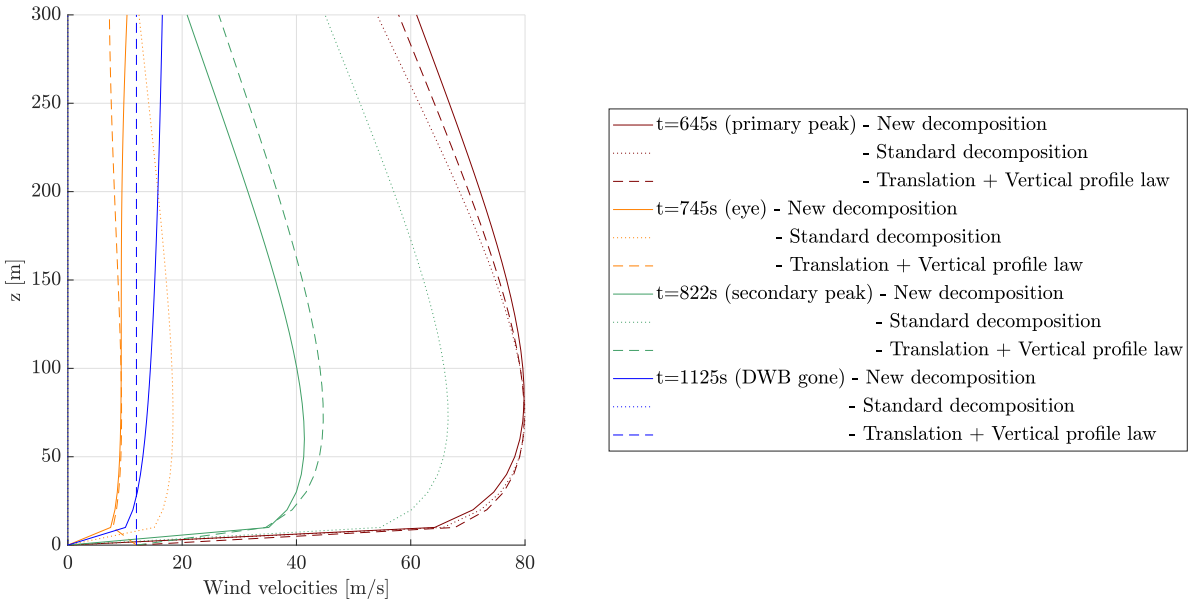

FIGURE 3.16: Evolution in time of the vertical profile for different choices of velocity decomposition.

3.4 Parametric study

Having validated the new proposition of wind model for the downburst event of Andrews A.F.B. by means of the set n°1 of parameters, it is interesting to understand how those parameters influence the wind velocities generated by the model. A parametric study is then performed with respect to the following parameters of which the influence is studied separately from each other :

- The reference mean wind velocity V_{ref} for establishment of the background wind velocity profile.
- The translation velocity of the downburst, the downburst radius and the time intensification function.

Then, keeping in mind that the purpose of the wind generation proposed in this chapter is to be applied on structures as a loading, the effect of the wind modelling is studied on a vertical set of observer points as well as on a horizontal one. In this context, the effect of the model of mean velocity vertical profile "frozen" in time is investigated for vertical structure application mostly. In the mean time, horizontal structures are also under investigation in this section by looking into the influence of the downburst size (i.e. diameter) as well as into different downburst angle of attacks with respect to an horizontal set of observers.

3.4.1 Basic mean wind velocity for synoptic wind generation

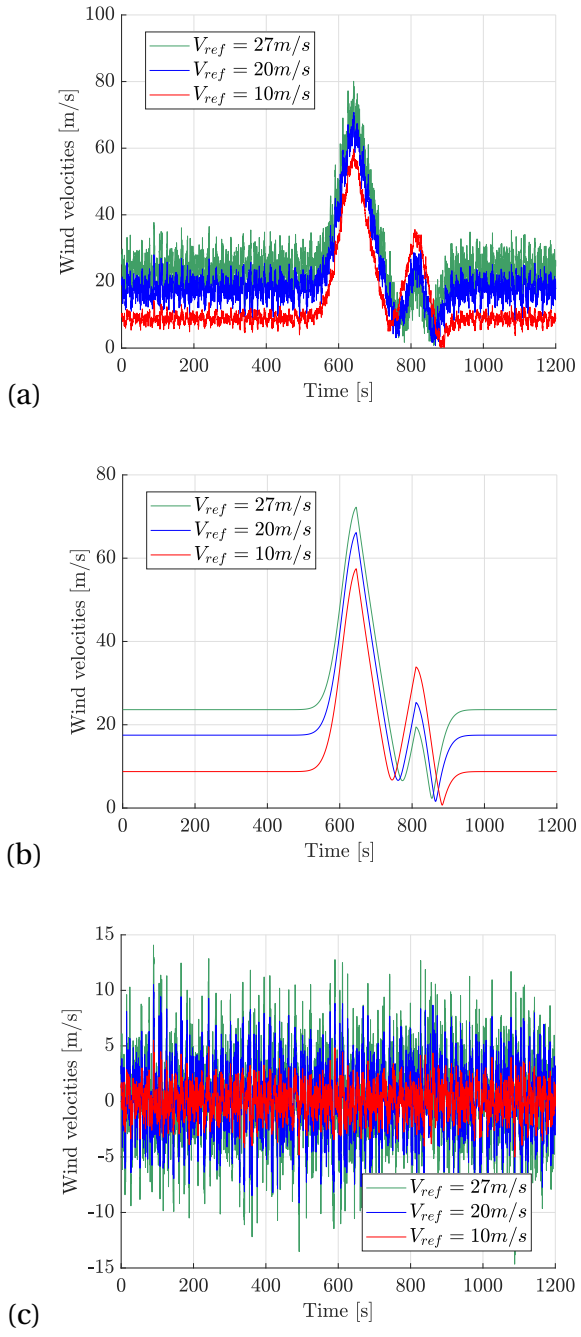

FIGURE 3.17: Downburst velocities time histories generated with the new model for different values of reference velocity in background turbulence generation: (a) Resultant wind velocity time history, (b) Mean wind velocity time history, (c) Turbulent velocity time history.

According to Eurocode, it is possible to compute the velocity profile of the background synoptic wind by implementing roughness conditions (exposure class II for Andrews A.F.B. because it is close to sea and rural environment) and reference wind velocity at 10 m height for a duration time of 10 min and a 10 year period of return (temporary structures). Indeed, this means that an unlikely event (wind velocities happening every 10 years) is combined with a downburst thunderstorm which already has a small probability of occurrence. Then, it does not make sense to use the reference wind velocities given by the Eurocode. This is supported by the results presented in FIGURE 3.17 (a), (b) and (c) page 33. In those FIGURES, it is shown that the use of 27 m/s as a reference velocity for computation of synoptic wind leads to an overestimation of the mean velocity component when the downburst is far from the observer point as well as an overestimation of the primary peak of mean velocity and an underestimation of the secondary peak of the Andrews A.F.B. downburst (FIGURE 3.17(a)). This difference between the effect on primary peak and secondary peak is explained by the fact that in the LRS of the observer, the background wind velocity goes in the same direction as the radial downburst-related velocity before the downburst joins the position of the observer whereas it goes in the opposite direction of the radial velocity after the passage of the downburst at the observer position. The amplitude of turbulence velocity component is also impacted as it can be seen on FIGURE 3.17(b) and (c). Indeed, the turbulence intensity is increased by using a higher reference velocity for background wind.

3.4.2 Scale parameters

The first scale parameter set to variation in the simulation of Andrews A.F.B. downburst is the translation velocity. The results of this change of parameter value are given by FIGURE 3.18 and show that the peaks of the mean wind velocity profile are advanced in time for greater value of translation velocity and the distance separating the peaks is reduced as it could have been expected. Another ascertainment from this graph is the diminution of the peaks intensity for higher translation speeds. This is only due to the fact that the time function is the same for all translation velocity and this intensification function is set to maximise the wind velocity at the first peak in the initial configuration aiming the representation of Andrews A.F.B. downburst.

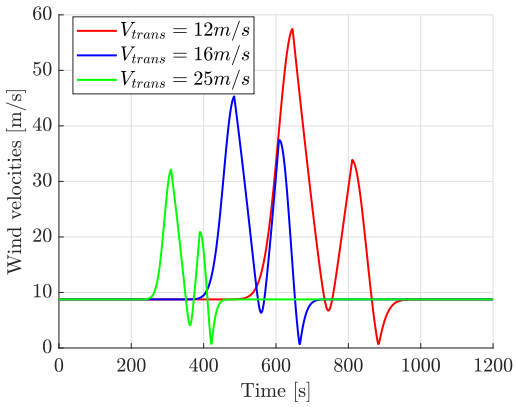

FIGURE 3.18: Mean wind velocity time history for different values of downburst translation velocity.

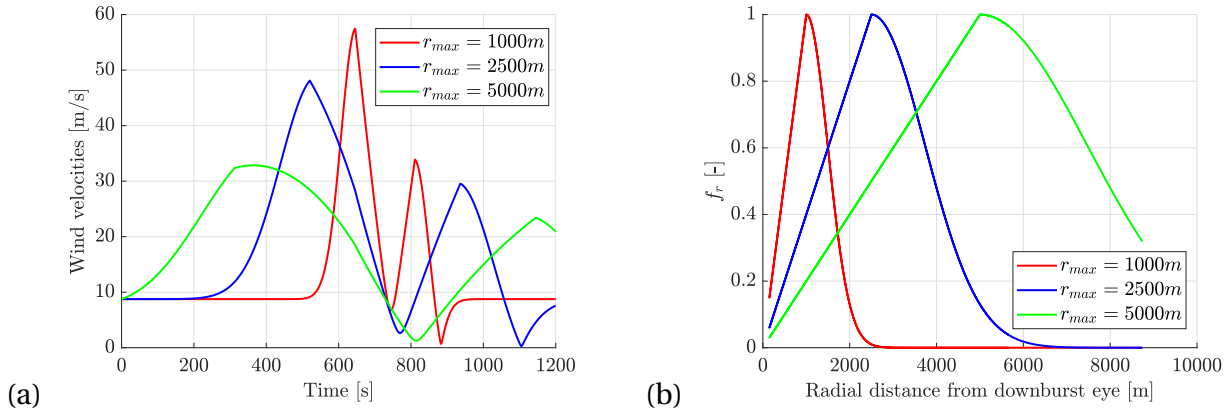

FIGURE 3.19: Influence of the downburst radius parameter on the mean wind velocity time history: (a) Mean wind velocity time history for different downburst size, (b) Radial intensification function for different downburst radius.

Next, the effect of the variation of the downburst radius parameter r_{max} is studied in FIGURES 3.19 (a) and (b) above. It can be observed on these figures that the mean wind velocity peaks are further from each other for higher values of r_{max} and are also more progressives. The first observation is explained that, giving the increased size of the downburst, the first/second

peak appears at a further distance than with the initial value of r_max and then earlier/later in the time history. Second, the progressiveness of the mean wind velocity peaks are due to a more spread radial intensification function, visible on FIGURE 3.19 (b). As for the translation velocity, a diminution of the peaks is illustrated. This is again a result of the initial set of the time intensification function.

The colours of the velocity vectors appearing on FIGURE 3.21 page 35 matches the same legend than the FIGURE 3.20 page 35. These FIGURES 3.21 and 3.20 study the effects of a change of time intensification function. Thus, the FIGURES 3.21 and 3.20 jointly shows that the difference between the velocity peaks is only due to the change of sign of the background velocity vector with respect to the radial velocity when the a unitary time intensification function is employed whilst the peaks of velocity both diminish when the maximum of the time intensification function (i.e. $f_t = 1$) is set sooner than the maximum of the spatial intensification function (i.e. $f_r = 1$).

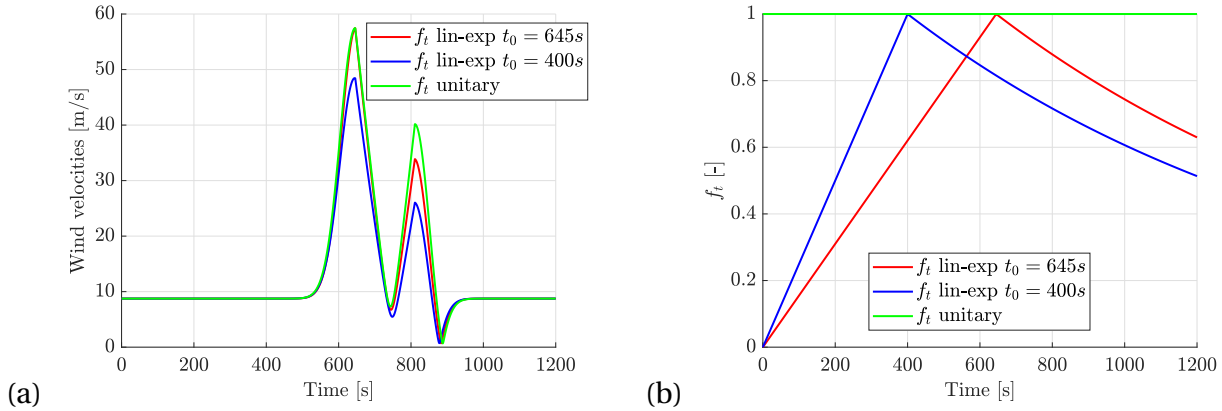

FIGURE 3.20: Influence of the time intensification function parameter on the mean wind velocity time history: (a) Mean wind velocity time history for different time intensification functions, (b) Time intensification functions.

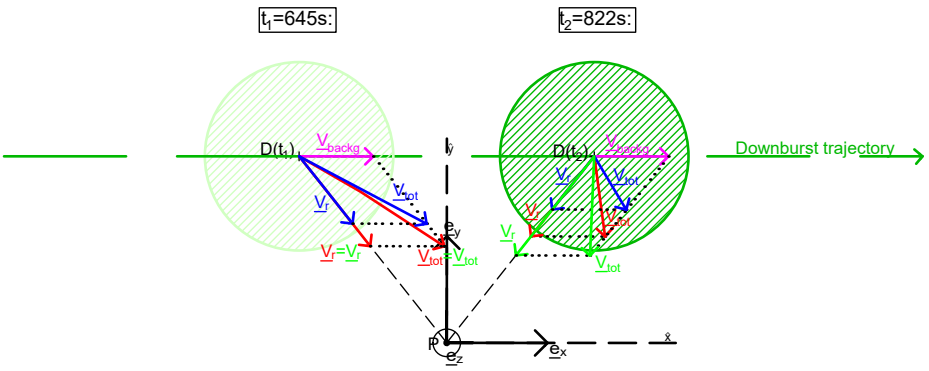

FIGURE 3.21: Vector scheme of the velocity vector components happening at the velocity peaks for unitary f_t, $t_0 = 645s$ and $t_0 = 400s$ respectively.

Finally, various orientations of downburst trajectory are tested on a horizontal set of observer, instead of one point of observation as it was used before to represent the Andrews A.F.B. downburst. This new set of observer corresponds to the case of a cable which is studied further in this work. The mesh formed by this new set of observers as well as the different trajectory tested are shown on FIGURE 3.22 below. These trajectories are chosen in order to keep the same initial distance from the centre of the set of observer.

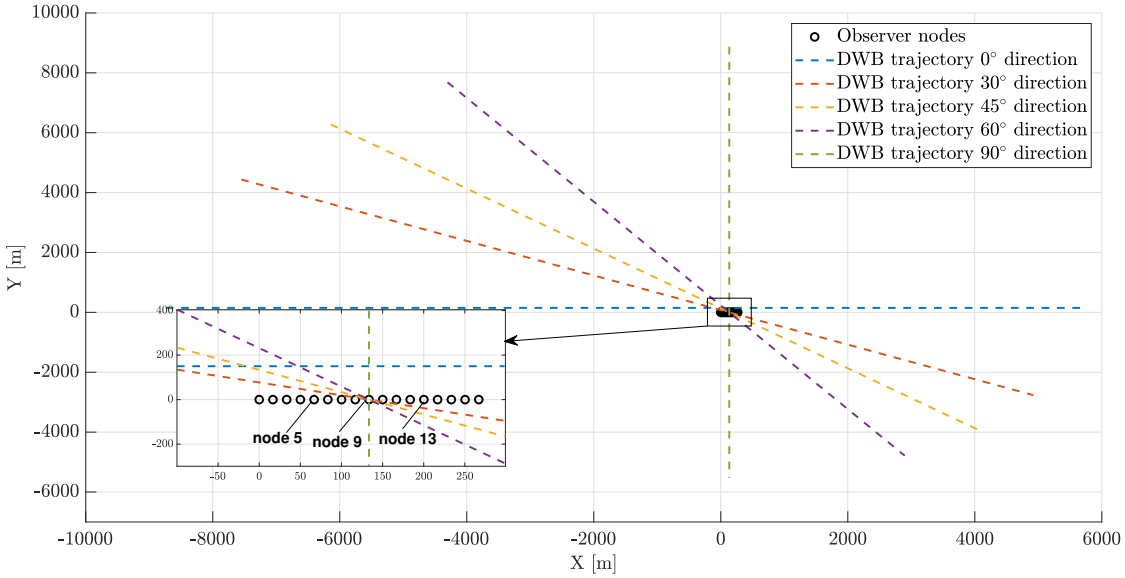

FIGURE 3.22: Downburst trajectory and horizontal set of observer nodes.

The results in terms of total wind velocity time history are presented in FIGURE 3.23 hereafter. The choice of a downburst trajectory parallel to the set of observer (0°angle) engenders no differences of intensity in the wind velocity time histories between the 3 locations of point of observation but only a small time lag caused by the distance between the points of interest. Still for this trajectory, the y-diection wind velocity contribution is zero-mean until the downburst pass near the observation point. This is explained by the fact that only the synoptic wind acts on the observer when the downburst is too far to influence the wind velocity at this point and in the case of a 0°angle trajectory of downburst the synoptic wind brings no mean wind component in y direction (only turbulence). Conversely, in the same optic, a downburst trajectory perpendicular (y-directed) to the set of observer (x-directed) (i.e. with a 90°angle) . The particularity of this trajectory is that it creates a zero mean total wind velocity during the whole time simulation at the node 9 (half-span) because this point coincides with the downburst trajectory which is oriented in direction y and then no mean wind x component is ever generated at this particular point of observation, as indicates FIGURE 3.23 (c). It can also be noted that for this same trajectory, the sign of the wind velocity in direction x at node 5 (1/4 span) is opposed to the sign of the wind velocity in direction x at node 13 (3/4 span) during the passage of the downburst (cfr. FIGURE 3.23 (a) and (e)), simply because these points are situated from either side of the 90°trajectory (see FIGURE 3.22). Now, regarding the envelope of the total wind velocity time histories, it can be said

that the critical case in terms of velocity intensity oriented in direction x and direction y are the 0°angle trajectory and the 90°angle trajectory respectively.

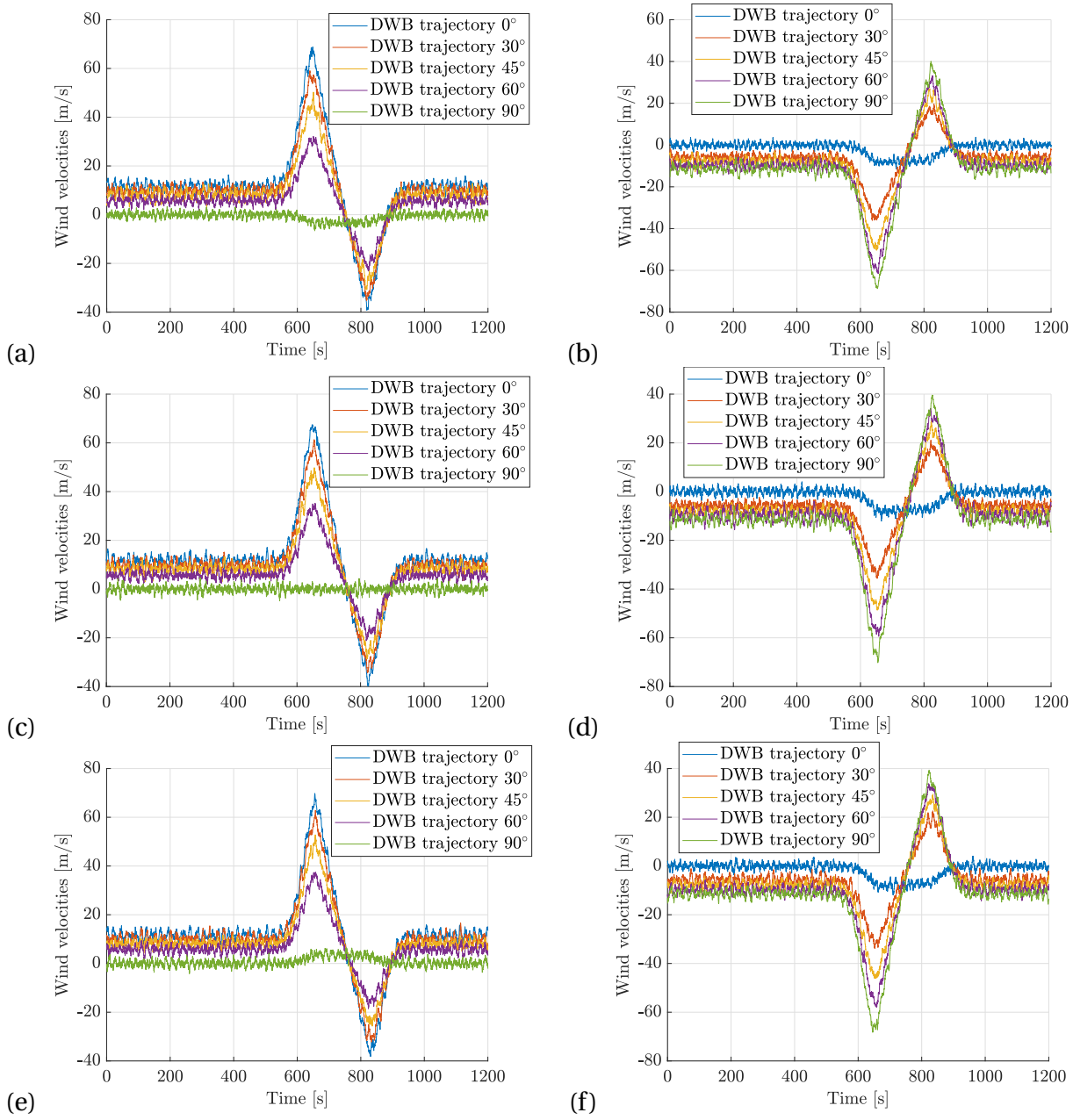

FIGURE 3.23: Resultant wind velocity histories in the local reference system at node 5, 9 and 13 of the horizontal set of observers for different angles of downburst trajectory: (a) Node 5 (1/4 span) x-direction, (b) Node 5 (1/4 span) y-direction, (c) Node 9 (half-span) x-direction, (d) Node 9 (half-span) y-direction, (e) Node 13 (3/4 span) x-direction, (f) Node 13 (3/4 span) y-direction.

CHAPTER

4 Effects of thunderstorm downburst on structures

Once the wind field of downburst created, it is needed to apply it to structure in order to evaluate the structural response to downburst thunderstorm. The generation of the wind field is made such that wind velocity time history is spread into the nodes of the mesh considered. In this manner, the excitation is available at whole times of the simulation and for each node of the structural mesh to be considered. The excitation of the wind is materialised as aerodynamic forces, proportional to the squared wind velocity and depending on the angle of attack of the wind with respect to the structure as a well as geometric properties of the structure. Those aerodynamic forces are then applied directly to the mesh and the Newton-Raphson numerical algorithm is used to solve motion equilibrium equations. This procedure is made through the intermediate of the finite element software Nonda. This non-linear finite element software is preferred because the structure of interest in this work are flexible which implies non-linearity.

The structures to be studied in this section are the following:

- CAARC tall building
- Iced cable

4.1 Validation of the code: Static unit load case

A small example of a cantilever composed of 2 nodes (one is fixed) loaded at the top by a static unit load is used in order to validate the finite element code necessary to simulate the response to the wind load. Indeed, the analytical results can be computed easily and allow to validate the code.

4.2 Vertical cantilever application: case of CAARC building

For the first application of the downburst wind loading generated through the new model explained in CHAPTER 3, a vertical building is chosen: the CAARC (Commonwealth Advisory Aeronautical Council) building. This choice has been driven by the fact that plenty of studies has

been using this building as an example in aerodynamics studies (Alminhana et al., 2018) (Braun and Awruch, 2009) but also to study the response of a structure to a downburst event (Le and Caracoglia, 2017) (Chen and Letchford, 2004b).

4.2.1 Parameter nC

In the background turbulence generation process exposed in SUBSECTION 3.2.1, two steps were distinguished:

- The establishment of the turbulence PSD through Solari and Piccardo (2001)'s method.
- The generation of random processes developed by Di Paola and Gullo (2001).

In the second step (generation of random processes), needed to generate the random samples of the background turbulence, as the turbulence PSD is decomposed into the basis of its own eigenvectors, the number of eigenvalues to consider must be evaluated. This number represents the number of fully correlated components with 1 eigenvalue corresponding to 1 degree of freedom of the structure. Knowing that the CAARC building mesh is composed by 41 nodes (i.e. 123 degrees of freedom), the FIGURE 4.1 hereafter shows that not all the degrees of freedom need to be fully correlated to obtain one sample of background turbulence, because only a few are dominant in the range of the low frequencies, which are of interest in the case of slender structure. It is worth noting that on this figure the eigenvalues are numbered such that the first is the biggest eigenvalue, the second is the second biggest, and so on.

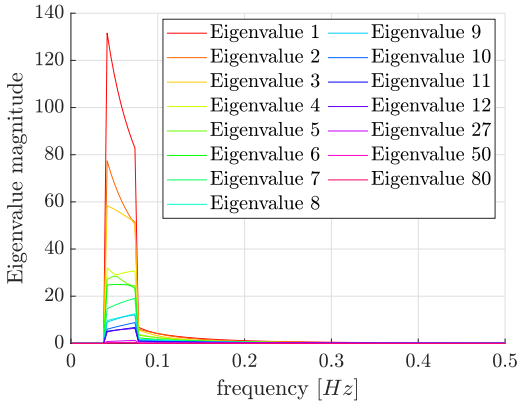

FIGURE 4.1: Frequency dependent eigenvalues of the background turbulent velocities PSD for CAARC building example.

The chosen criterion to obtain a coherent value of nC and avoid a too long time of computation is to take into account in the random samples generation only the eigenvalues that have a maximum bigger than 1% of the maximum of the first eigenvalue (Eigenvalue 1). The application of this criterion gives: $nC = 27$. It is important to keep in mind that this criterion implies to forgot some modes of which the corresponding frequency of excitation can be met even though the excitation intensity is weak. However, the criterion is kept as such in order to avoid a too big simulation run time.

4.2.2 Mesh and geometry

The finite element mesh of CAARC building is the same as in Le and Caracoglia (2017) as it allows to potentially compare the results obtained after simulation. This mesh is composed of 41 nodes distant from each other of 4.575 m which represents approx one storey of the building for a total height of 183 m. The section of the building is simplified as a rectangle of 45.7 m over 30.5 m. The longer side of the section is subjected to the alongwind component of the wind field. The mesh of CAARC building is visible in FIGURE 4.2 below (Le and Caracoglia, 2017). Geometrical and aerodynamic parameters are summarised in TABLE 4.1 hereafter (Le and Caracoglia, 2017).

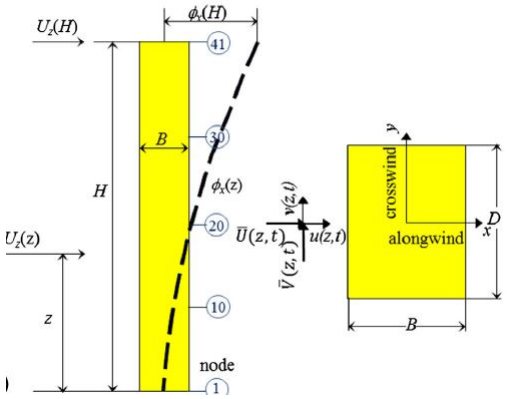

FIGURE 4.2: Schematic vertical-plane view of the CAARC building, adapted from Le and Caracoglia (2017).

Parameter or physical quantity [with units]	Values
Width of cross section, B [m]	30.5
Depth of cross section, D [m]	47.5
Height of cross section, H [m]	183
Mass per unit height, m [kg/m]	220800
Modal damping ratios, ζ_x, ζ_y	0.01
Fundamental natural frequency in x-direction, n_x [Hz]	0.20
Fundamental natural frequency in y-direction, n_y [Hz]	0.22
Normalized mode shape in x-direction, ϕ_x	$(z/H)^1$
Normalized mode shape in y-direction, ϕ_y	$(z/H)^1$
Drag coefficient, C_D	1.2
First derivative of drag coefficient, $C'_D = \partial C_D/\partial\alpha$	−1.1
Lift coefficient, C_L	−0.1
First derivative of lift coefficient, $C'_L = \partial C_L/\partial\alpha$	−2.2

TABLE 4.1: Structural and aerodynamic properties of CAARC building, adapted from Le and Caracoglia (2017).

4.2.3 Aerodynamic forces implementation

Due to the transient nature of the downburst wind field, the wind angle of attack is varying in function of time. In order to reproduce the most precisely possible the aerodynamic forces, this variation must be taken into account in the calculation of the aerodynamic forces. That means

that the forces must be calculated at each time iteration in function the time instant wind angle of attack. In fact, this angle influences the value of the drag and lift coefficients. The relation angle of attack - aerodynamic coefficient is particular of the case of study considered. Therefore, this relation is given by Alminhana et al. (2018) for the CAARC building following the batteries of test they made and the results are represented in FIGURE 4.3 hereafter. These relations visible on the graph are depending on their environment, i.e. the class of exposure. However, the Alminhana et al. (2018) refers to the Brazilian Wind Code (NBR6123/88) which differs from the standards of Eurocode. Then, the choice of the "p=0.23" ensemble of points is made, corresponding to urban areas conditions of roughness which matches the best the environment of the case studied in this work. Practically, in the code, an interpolation of the points is made in order to obtain a continuous curve of angle of attack - aerodynamic coefficient relation.

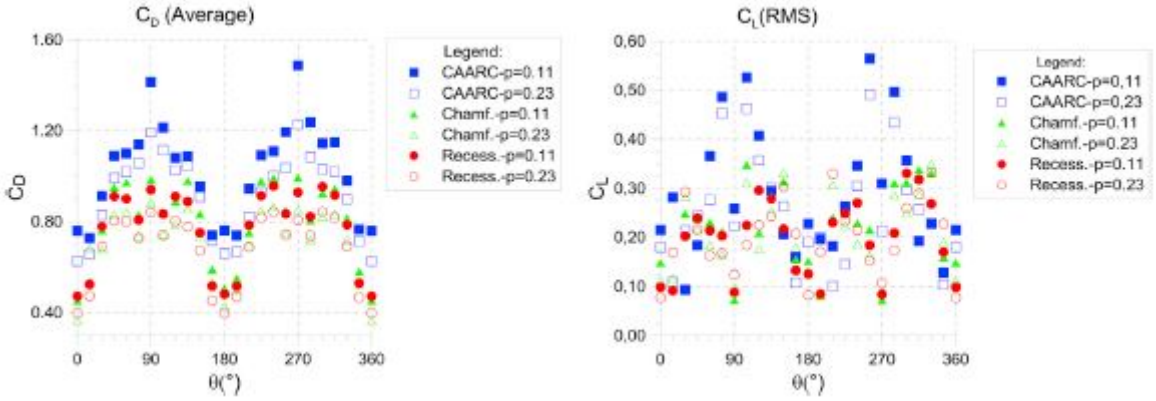

FIGURE 4.3: Drag and lift coefficients of CAARC building in function of the wind angle of attack, adapted from Alminhana et al. (2018).

Aerodynamic forces by units of length (along the height of the CAARC building) can be written the following way:

$$\begin{cases} f_D = \frac{1}{2}\rho_{air} C_D D V^2_{alongwind} \ [kN/m] \\ f_L = \frac{1}{2}\rho_{air} C_L D V^2_{crosswind} \ [kN/m] \end{cases} \tag{4.1}$$

Where f_D and f_L are respectively the drag force and lift force per unit length, ρ_{air} is the air specific mass, D is the characteristic dimension of the CAARC building section that is orthogonal to the main direction of the air flow (alongwind direction) and $V_{alongwind}$ and $V_{crosswind}$ are respectively the wind velocity in alongwind and crosswind direction.

4.2.4 Results

The FIGURE 4.4 (a) and (c) hereafter illustrates the fact that the response of the CAARC building to the Andrews A.F.B. downburst wind loading is quasi-static. Indeed, these FIGURES show that rapid variations around the mean displacement response have a small magnitude compared to

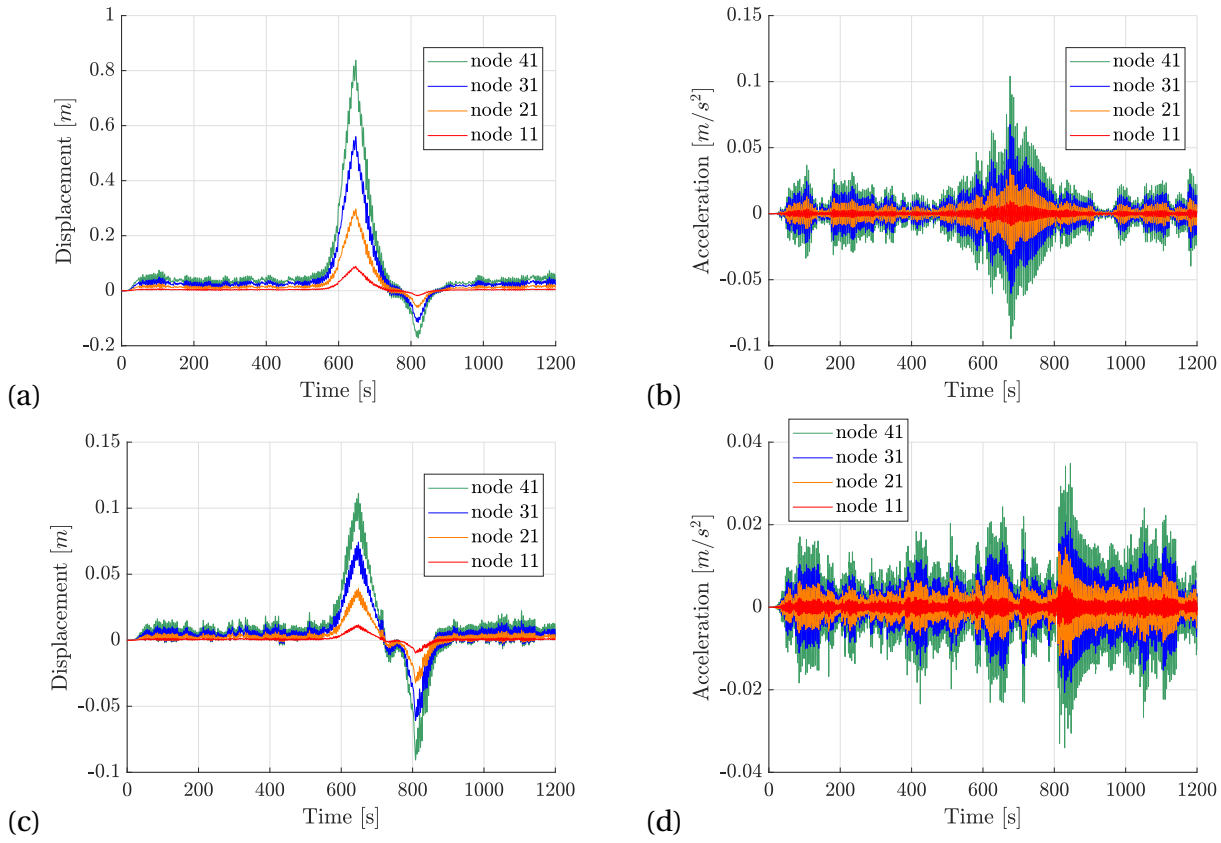

FIGURE 4.4: Response of the CAARC structure to the wind load coming from the Andrews A.F.B. downburst, in terms of displacement and acceleration in x and y directions: (a) Displacement in direction x, (b) acceleration in direction x, (c) Displacement in direction y, (d) acceleration in direction y.

In terms of displacement at the top of the CAARC tower, the value obtained is far from the displacement resulting from the Le and Caracoglia (2017) simulation. In fact, the order of magnitude of the top displacement in direction x of Le and Caracoglia (2017) is 10m while in this work the order of magnitude is closed to 1m (FIGURE 4.4 (a)). This difference is huge and that was the reason of the code validation (cfr. SECTION 4.1 page 38).

The dynamic displacement response of CAARC time histories show quasi-static properties in direction x while the fluctuations in the displacement response along y axis are bigger compared to the mean allure of the response which presents a weaker peak in comparison with the x direction response. The CAARC building is in fact responding to the slowly time-varying mean wind component of the downburst which is why the response in direction x can be considered as quasi-static. This conclusions on the dnamic repsonse of the CAARC tower to downburst solicitation is going the same way as in Le and Caracoglia (2017). However, it is important to keep in mind that the radial turbulence of the downburst was not considered in the wind field model.

4.3 Horizontal structure application: case of iced cable

After having applied the downburst wind field of Andrews A.F.B. to a vertical structure (CAARC building), it is now a horizontal structure which is submitted to the downburst wind field: an iced

cable case defined in Foti and Martinelli (2018b). The choice of this example has been driven by the fact that:

- This is a cable, so that it is useful to the extension of this work which is the application of the wind field to a transmission line structure composed of cables and towers.
- This is an interesting case of cable because it is in fact an iced-cable which means that is section is completed with an u-shaped ice accretion. Also, the geometry of this cable is such that it is subjected to modal coupling between 3 of the first natural frequencies modes (Foti and Martinelli, 2018b).
- The cable is an already existing case of study in literature (cfr. Foti and Martinelli (2018b) and Foti and Martinelli (2018a)).

In this section, a deeper analysis of the structural response is performed with development of rank 1 and 2 statistics on the basis of 500 random samples of downburst wind field. In addition, the procedure is iterated for 5 different downburst trajectories (0°, 30°, 45°, 60°and 90°), corresponding to the ones described in FIGURE 3.22 page 36.

4.3.1 Parameter nC

The same process than in SUBSECTION 4.2.1 is applied to the example of the iced cable for the evaluation of the parameter nC value. This leads to a number of 19 turbulence PSD eigenvalues to be considered in the random samples of background turbulence generation.

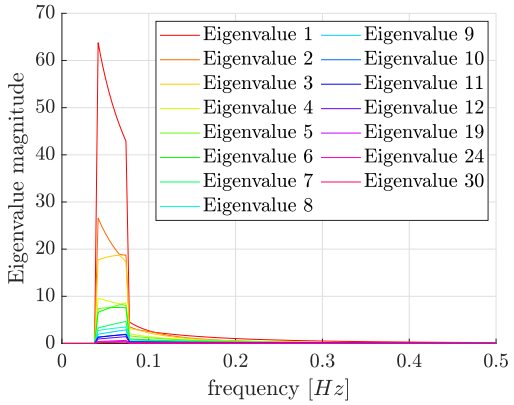

FIGURE 4.5: Frequency dependent eigenvalues of the background turbulent velocities PSD for iced cable example.

4.3.2 Mesh and geometry

(Foti and Martinelli, 2018b)

The mesh of the iced cable case is described at FIGURE 3.22 page 36 as well as the different studied trajectories of downburst. It is composed of 8 cable elements comprising 3 nodes each for a total of 17 nodes. Each nodes is initially distant by 16.68375m from each other giving a total span length of 266.94m compared to the 267.09m of length in the static configuration of the cable. It is worth noting that the cable is horizontal (along direction x) in the initial conditions and situated at z=20m. This height has been chosen in order to be in accordance to small transmission lines infrastructure. However, heights closer to 70 m for example can be implemented for high transmission lines structures and it will result in larger wind velocities applied to the structure. The steel reinforced aluminium conductor DRAKE ACSR 7/26 is chosen for the cable material and is giving the mechanical and geometrical properties described in TABLE 4.6 hereafter.

d (cm)	m (kg/m)	EA (kN)	EI (Nm^2)	GJ (Nm^2)	C_T (Nm)
2.81	1.8	29700	2100	159	0

FIGURE 4.6: Mechanical and geometrical properties of the DRAKE ACSR cable, adapted from Foti and Martinelli (2018b).

Here is the cross-section of the iced cable:

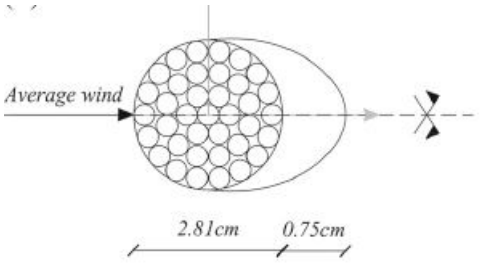

FIGURE 4.7: Iced cable section with u-shaped ice accretion, adapted from Foti and Martinelli (2018b).

4.3.3 Aerodynamic forces implementation

The process of aerodynamic forces is similar to the one used for CAARC building in SUBSECTION 4.2.3 page 40 but with drag and lift coefficients - angle of attack relation adapted to the present case of iced cable, which are shown at FIGURE 4.8 hereafter.

4.3.4 Self-weight application

As the iced cable is entered in the Nonda software as an horizontal lines, the self weight is applied when the simulation starts and it is done by introducing the self-weight as an initial distributed force on the mesh. It is worth noting that the horizontal set up of the cable initially is allowed only by adding very small fictive tension in the cable elements at the initial state in order to avoid instability.

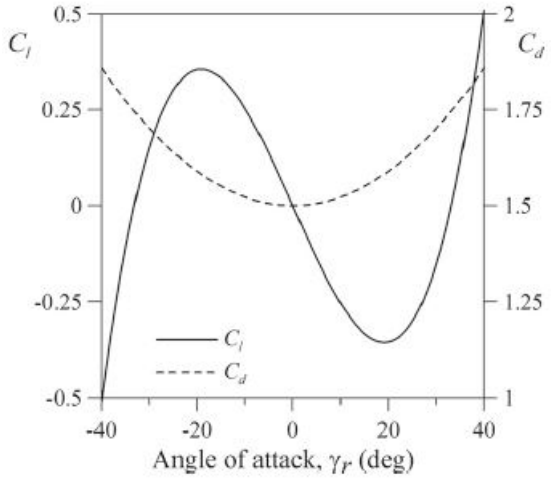

FIGURE 4.8: Drag and lift coefficients of iced cable in function of the wind angle of attack, adapted from Foti and Martinelli (2018b).

4.3.5 Results

Nonda output gives the following values of iced cable natural frequencies:

COMPUTED EIGENVALUES

EIGENVALUES	CIRCULAR FREQ.	PERIOD	Hz
0.1972061E+01	0.1404301E+01	0.4474240E+01	0.2235016E+00
0.7841526E+01	0.2800272E+01	0.2243775E+01	0.4456775E+00
0.7862670E+01	0.2804045E+01	0.2240756E+01	0.4462780E+00
0.7886060E+01	0.2808213E+01	0.2237430E+01	0.4469413E+00
0.1777880E+02	0.4216492E+01	0.1490144E+01	0.6710760E+00
0.1884263E+02	0.4340810E+01	0.1447467E+01	0.6908619E+00
0.3176570E+02	0.5636106E+01	0.1114809E+01	0.8970149E+00
0.3186180E+02	0.5644626E+01	0.1113126E+01	0.8983709E+00
0.5011343E+02	0.7079084E+01	0.8875697E+00	0.1126672E+01
0.5065686E+02	0.7117363E+01	0.8827960E+00	0.1132764E+01
0.7329813E+02	0.8561433E+01	0.7338935E+00	0.1362596E+01
0.7390936E+02	0.8597055E+01	0.7308526E+00	0.1368265E+01
0.1018144E+03	0.1009031E+02	0.6226944E+00	0.1605924E+01
0.1031655E+03	0.1015704E+02	0.6186035E+00	0.1616544E+01
0.1277682E+03	0.1130346E+02	0.5558636E+00	0.1799003E+01
0.1306683E+03	0.1143103E+02	0.5496603E+00	0.1819306E+01
0.1886741E+03	0.1373587E+02	0.4574287E+00	0.2186133E+01
0.1905940E+03	0.1380558E+02	0.4551189E+00	0.2197228E+01
0.2461455E+03	0.1568903E+02	0.4004825E+00	0.2496988E+01
0.2495426E+03	0.1579692E+02	0.3977472E+00	0.2514159E+01
0.3195752E+03	0.1787667E+02	0.3514738E+00	0.2845162E+01
0.3248092E+03	0.1802246E+02	0.3486305E+00	0.2868367E+01
0.4111482E+03	0.2027679E+02	0.3098706E+00	0.3227154E+01
0.4187554E+03	0.2046351E+02	0.3070431E+00	0.3256872E+01
0.5197620E+03	0.2279829E+02	0.2755987E+00	0.3628464E+01
0.5303217E+03	0.2302871E+02	0.2728411E+00	0.3665137E+01
0.6345553E+03	0.2519038E+02	0.2494278E+00	0.4009177E+01

FIGURE 4.9: Computed eigenvalues and corresponding natural frequencies resulting from Nonda simulation.

The first four natural frequencies of the cable structure corresponds respectively to the one loop symmetric out-of-plane (y) mode, the anti-symmetric two loop out of plane mode, the anti-symmetric two loop in-plane (z) mode and the symmetric one loop in-plane mode. The second to the fourth value of natural frequency are very close from each other which show the resonant nature of this iced cable.

In this section, the results of the simulations for an Andrews A.F.B. downburst with trajectories coming from 0°to 90°with respect to the axis x (longitudinal axis) are presented first in terms of displacement, acceleration and tension in the cable. From there, statistics of rank 1 are made as well as PSD is performed for each of these responses. In a second time, statistics of rank 2 are performed (correlation coefficient).

4.3.5.a) Rank 1 statistics and PSD

First of all, it is worth noting that the FIGURES 4.10 to 4.24 (b) are of no interest because the mean value of the acceleration response sample is close to zero as it was expected because the random background turbulence is generated as a zero-mean random process.

Next, concerning the displacement response, it is shown on FIGURES 4.10 to 4.24 (g) pp.48-60 that in the direction x, the displacement response is quasi-static because the PSD graphs present a peak only for very low frequencies (<0.05Hz) which is much lower than the first natural frequency of the structure (approx 0.2Hz) except in the case of an 90°trajectory of downburst (i.e. perpendicular to the longitudinal axis of the cable). Indeed, in that case, the FIGURE 4.22 (g) page 60 shows a dynamic response for frequencies of excitation in the range of 0.44Hz which corresponds to the second, third and fourth natural frequencies coupled of the iced cable even though the PSD intensity at these frequencies is low. Now looking at the displacement response in direction y, FIGURES 4.11, 4.14, 4.17, 4.20 and 4.23 (g) PSD distributions show peaks both a quasi-static background response in the very low frequencies and dynamic response in the first mode corresponding to the first natural frequency (0.22Hz). For 30, 45 and 60°trajectory of downburst, the dynamic response at 0.22Hz represents a much lower contribution of the total response than the background quasi-static response while they share the same contribution for 0 and 90°trajectory of downburst. Considering displacement in direction z, the PSD of displacement response of FIGURES 4.12, 4.15, 4.18, 4.21 and 4.24 (g) show no dynamic response except in the case of the 90°trajectory that presents PSD content at 0.44Hz and a lower contribution at 0.67Hz. For evaluation of the most critical trajectories of downburst in terms of displacements engendered, the 90°trajectory creates as expected the larger displacements (approx 3m) in direction y which is in the same axis. In other directions, the relative displacements are smaller than 0.5m.

In terms of acceleration response of the iced cable to the different trajectories of downburst sollicitation, in the direction x, FIGURES 4.10, 4.13, 4.16, 4.19 and 4.22 (g) show the presence of peaks in the PSD for 0.44,0.67 and at a lower level 0.69Hz which corresponds to the second to the sixth modes of the structure natural frequencies. The PSD peaks intensity is maximised for the 0°trajectory of downburst as expected. However, it is worth noting that the PSD presents a progressive peak centred at around 2Hz frequency. This could be the result of a not enough refined mesh of the cable structure which then does not allow to represent well the modes with small wavelength (i.e. high frequencies). In fact, the minimal wavelength is set to approximately the

distance between two nodes of the mesh (16 m in this case of mesh). An other observation that can be made on the basis of FIGURE 4.12 (h) page 50: The first peak of the acceleration response PSD in direction z is not regular and is distribution is enlarged around the 0.44HF frequency. This could be explained by the fact that displacement of the structure increases its stiffness and enlarges consequently the response peak. This observation is shared with FIGURES 4.12, 4.15 and 4.13 (h).

Tension is an other parameter of iced cable response that is studied (cfr. FIGURES 4.25 to 4.29 pp. 63-67 represent respectively the statistics and PSD for 0°to 90°downburst trajectory. It can be observed from these figures that the allure of the tension response is very similar for each trajectory excepted the 90°trajectory of downburst. The frequencies excited in the PSD are much lower than natural frequencies of the cable. Concerning the values of tension, the values of tension recorded are all smaller than .0013 kN and the downburst trajectory in direction parallel to the cable axis is the most critical as expected.

4.3.5.b) Rank 2 statistics

Further statistics can be obtained from the 500 samples of iced cable response generated, FIGURES 4.30, 4.31 and 4.32 pp.68-70 represent the coefficient of correlation R of acceleration response of the iced cable structure. The choice of the use of this rank 2 statistics tool is due to the availability of the random samples of wind field generated. An example of analysis of a graph of correlation and its interest is presented in the following.

On FIGURE 4.32 (e) page 70,focusing on the diagonal, it can be observed that correlation starts to spread at the characteristic time of the Andrews A.F.B. downburst (i.e. at time = 645 s) and it corresponds with the first peak of the wind velocity time history. Then, the correlation diminish before re-spreading when the second velocity peak is reached (at time = 822 s). This data is important because it can simplify the structural response by identifying the quasi-static responses that can be removed from the transient model. Concerning the parallels to the diagonal of correlation, their presence is recurrent approximately every 250 s because this time corresponds to the buffeting period. Indeed, damping happens after one buffeting period.

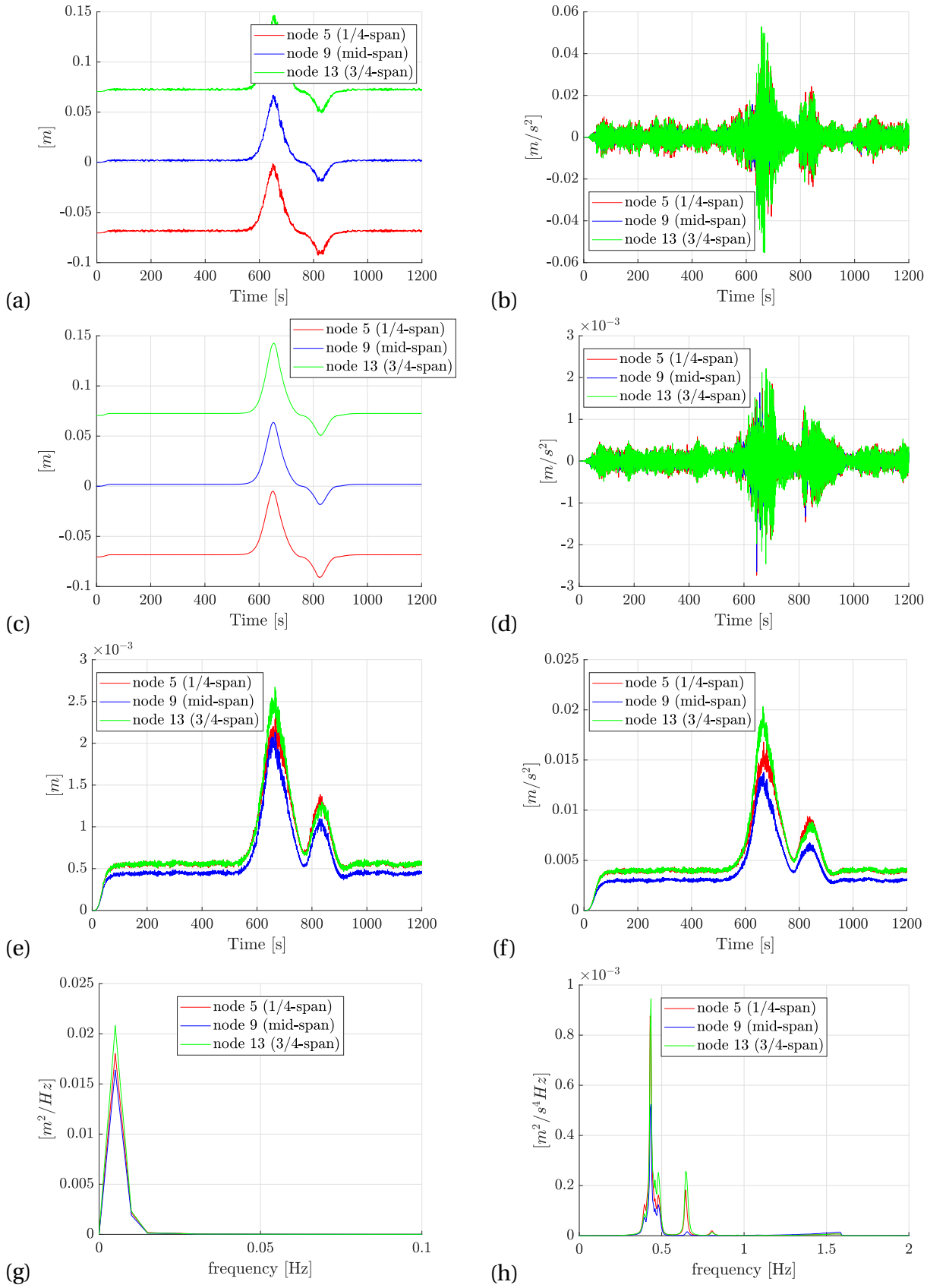

FIGURE 4.10: Statistics about the iced cable response at node 5, 9 and 13 in direction x for a downburst directed parallel to axis x: (a) Random sample of displacement response, (b) Random sample of acceleration response, (c) Mean of the samples of displacement response, (d) Mean of the samples of acceleration response, (e) Standard deviation of the samples of displacement response, (f) Standard deviation of the samples of acceleration response, (g) PSD of displacement response, (h) PSD of acceleration response.

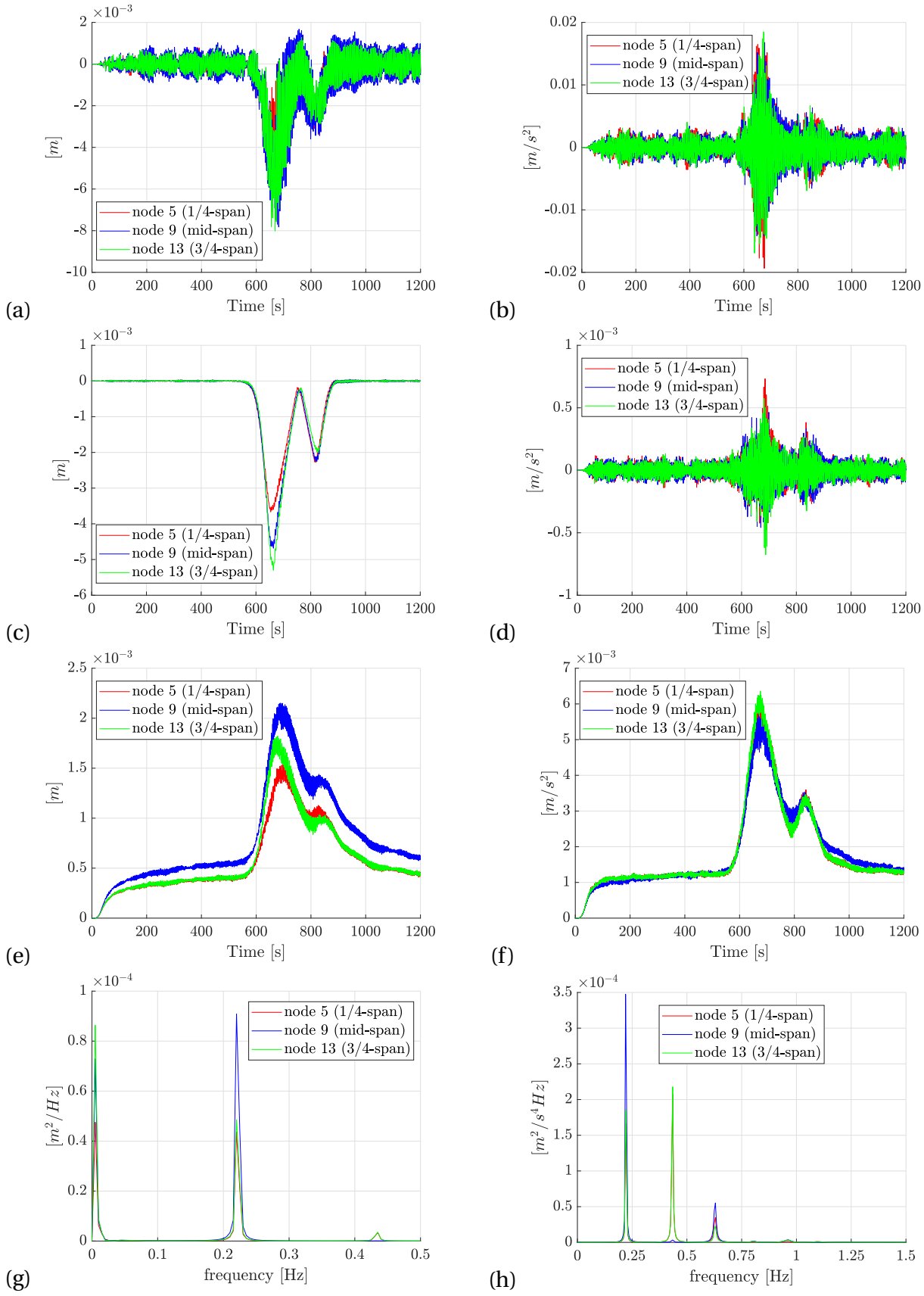

FIGURE 4.11: Statistics about the iced cable response at node 5, 9 and 13 in direction y for a downburst directed parallel to axis x: (a) Random sample of displacement response, (b) Random sample of acceleration response, (c) Mean of the samples of displacement response, (d) Mean of the samples of acceleration response, (e) Standard deviation of the samples of displacement response, (f) Standard deviation of the samples of acceleration response, (g) PSD of displacement response, (h) PSD of acceleration response.

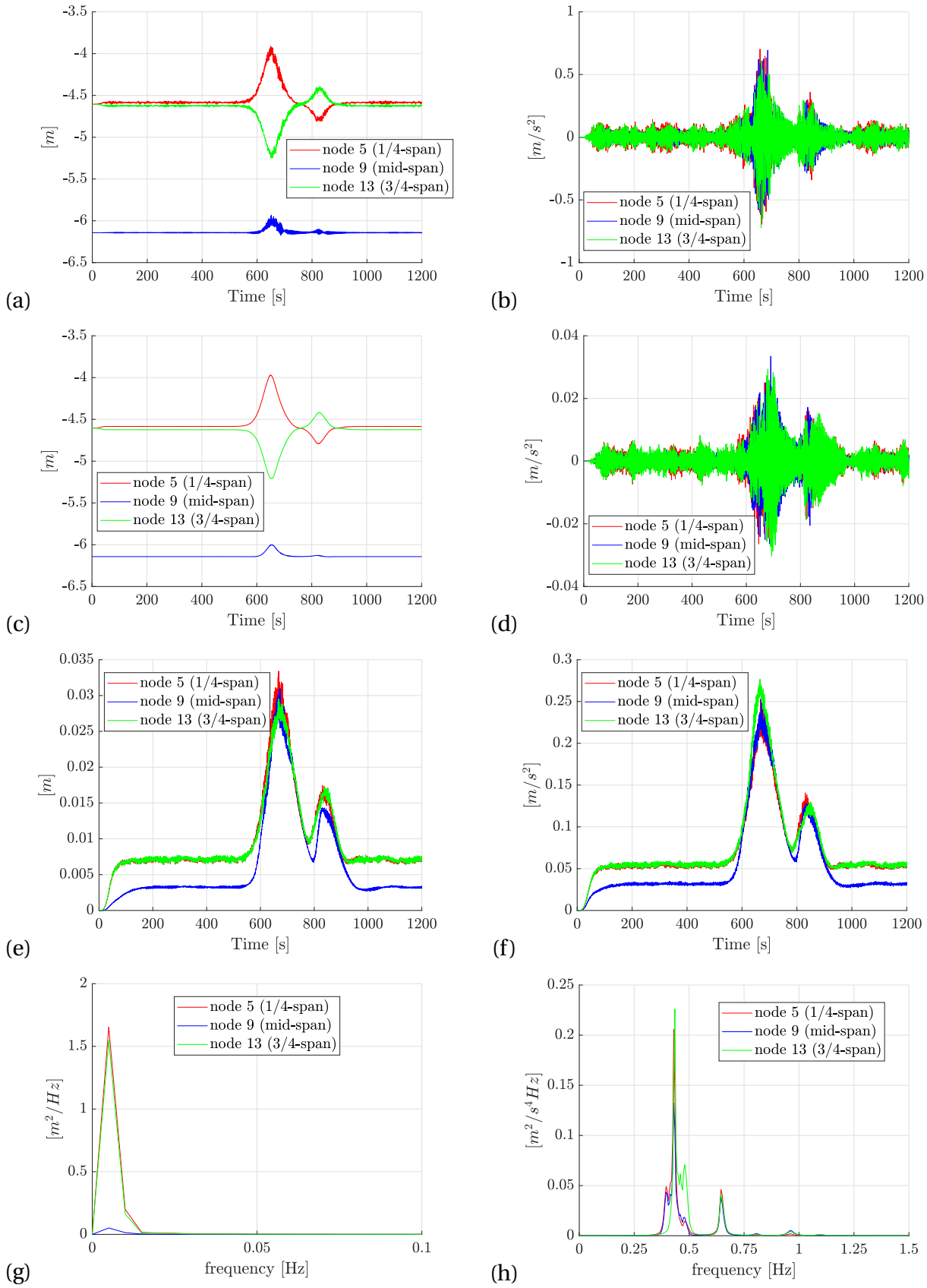

FIGURE 4.12: Statistics about the iced cable response at node 5, 9 and 13 in direction z for a downburst directed parallel to axis x: (a) Random sample of displacement response, (b) Random sample of acceleration response, (c) Mean of the samples of displacement response, (d) Mean of the samples of acceleration response, (e) Standard deviation of the samples of displacement response, (f) Standard deviation of the samples of acceleration response, (g) PSD of displacement response, (h) PSD of acceleration response.

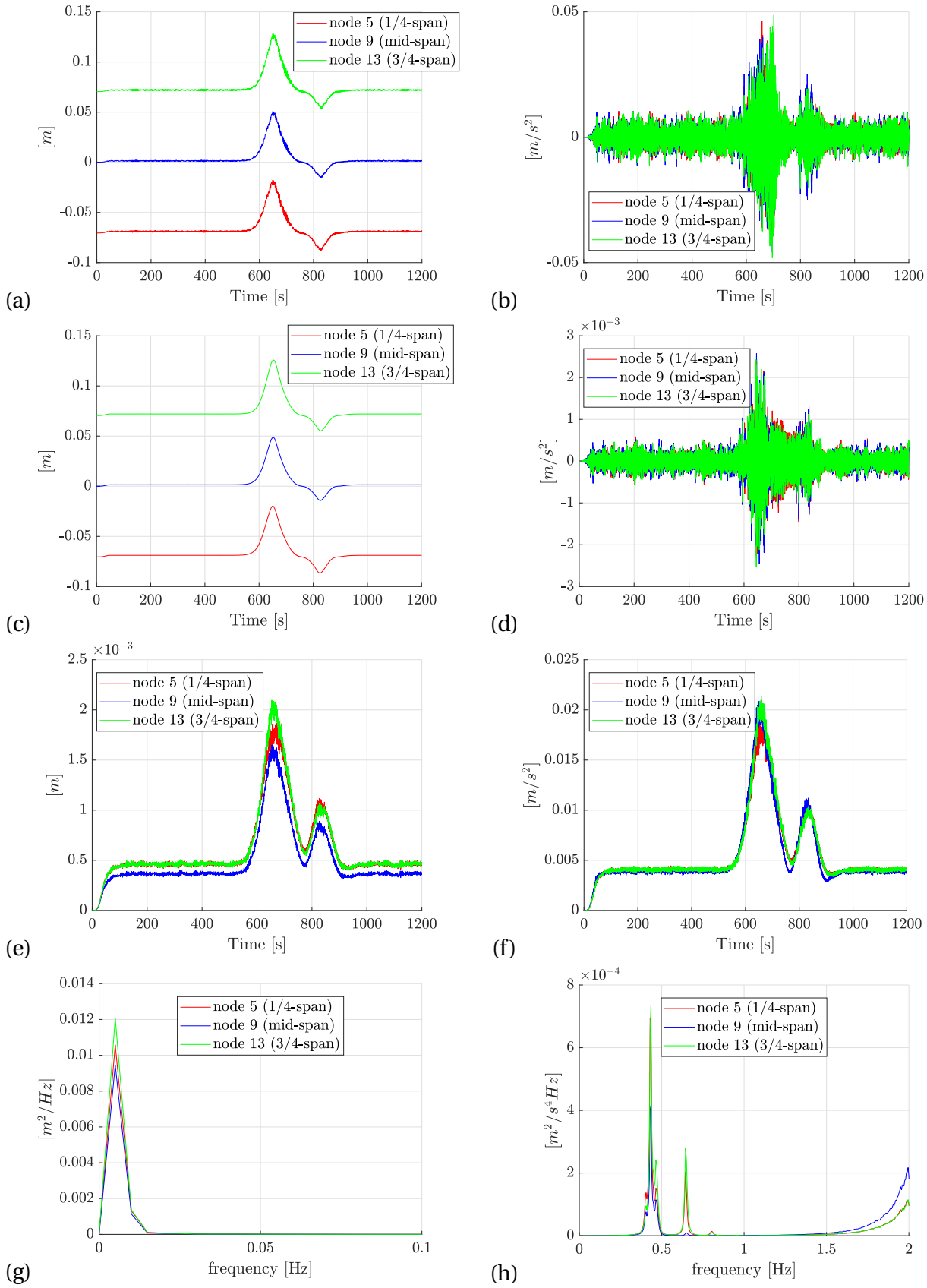

FIGURE 4.13: Statistics about the iced cable response at node 5, 9 and 13 in direction x for a downburst directed from a 30° angle with respect to axis x: (a) Random sample of displacement response, (b) Random sample of acceleration response, (c) Mean of the samples of displacement response, (d) Mean of the samples of acceleration response, (e) Standard deviation of the samples of displacement response, (f) Standard deviation of the samples of acceleration response, (g) PSD of displacement response, (h) PSD of acceleration response.

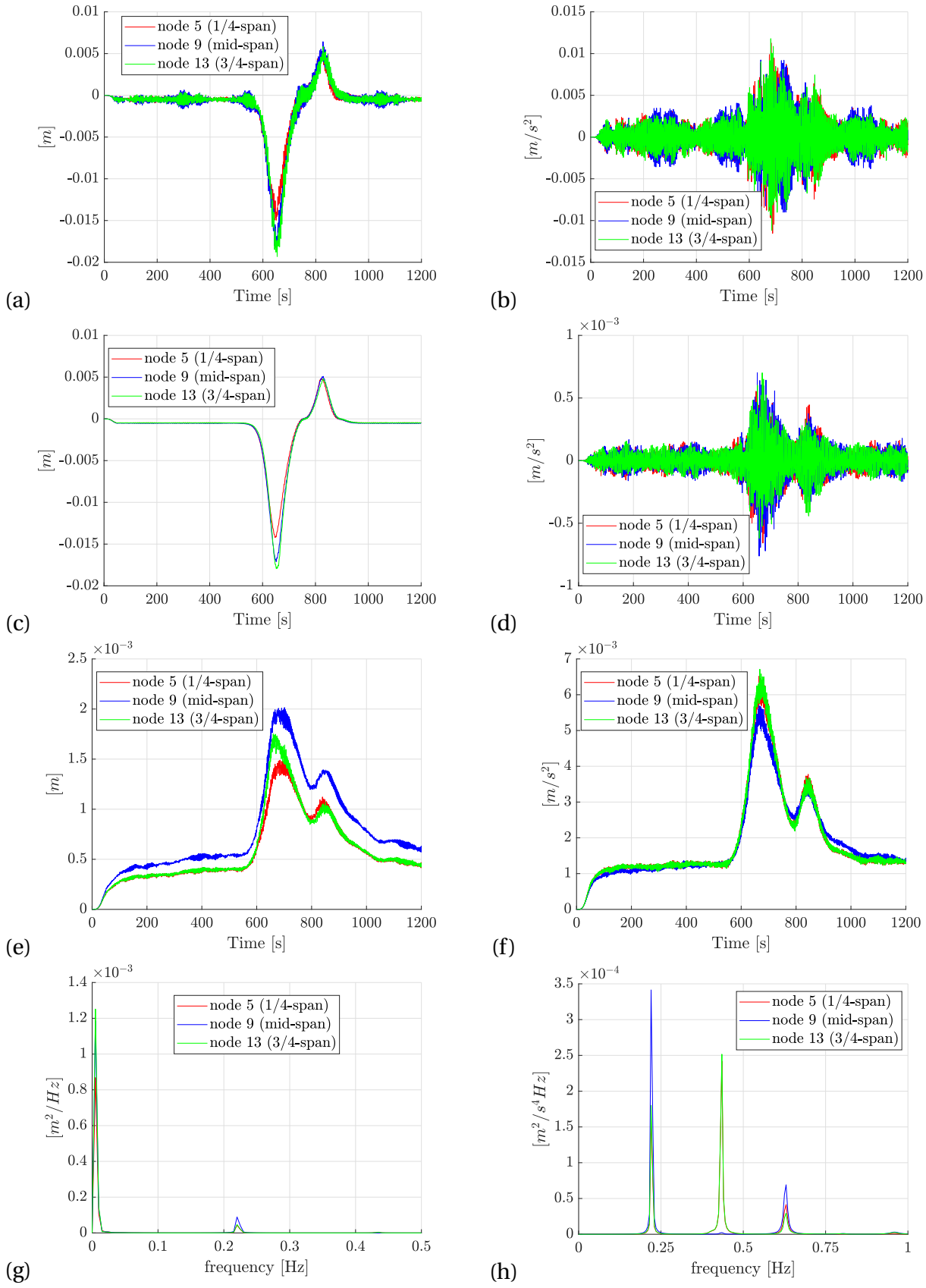

FIGURE 4.14: Statistics about the iced cable response at node 5, 9 and 13 in direction y for a downburst directed from a 30° angle with respect to axis x: (a) Random sample of displacement response, (b) Random sample of acceleration response, (c) Mean of the samples of displacement response, (d) Mean of the samples of acceleration response, (e) Standard deviation of the samples of displacement response, (f) Standard deviation of the samples of acceleration response, (g) PSD of displacement response, (h) PSD of acceleration response.

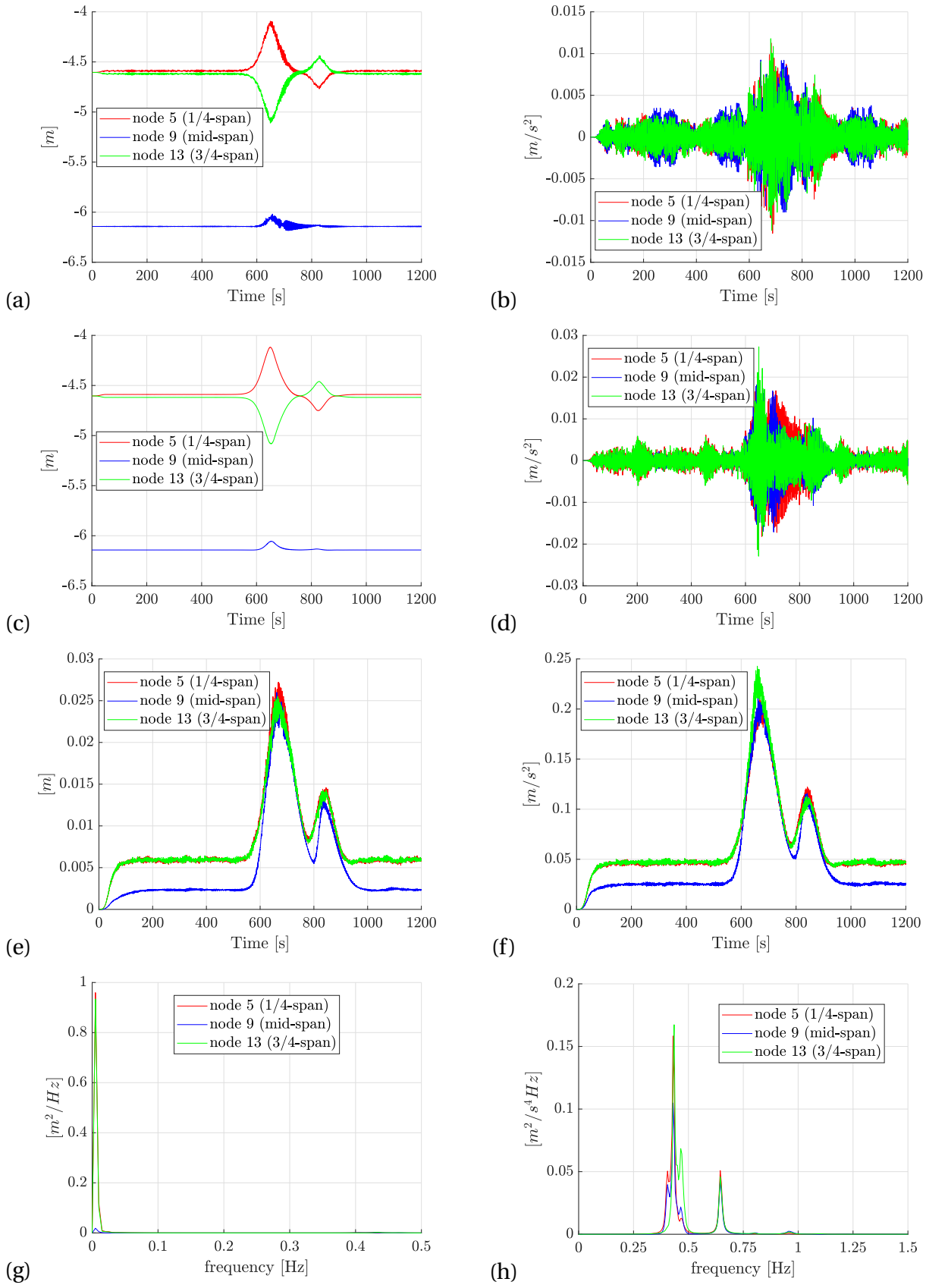

FIGURE 4.15: Statistics about the iced cable response at node 5, 9 and 13 in direction z for a downburst directed from a 30° angle with respect to axis x: (a) Random sample of displacement response, (b) Random sample of acceleration response, (c) Mean of the samples of displacement response, (d) Mean of the samples of acceleration response, (e) Standard deviation of the samples of displacement response, (f) Standard deviation of the samples of acceleration response, (g) PSD of displacement response, (h) PSD of acceleration response.

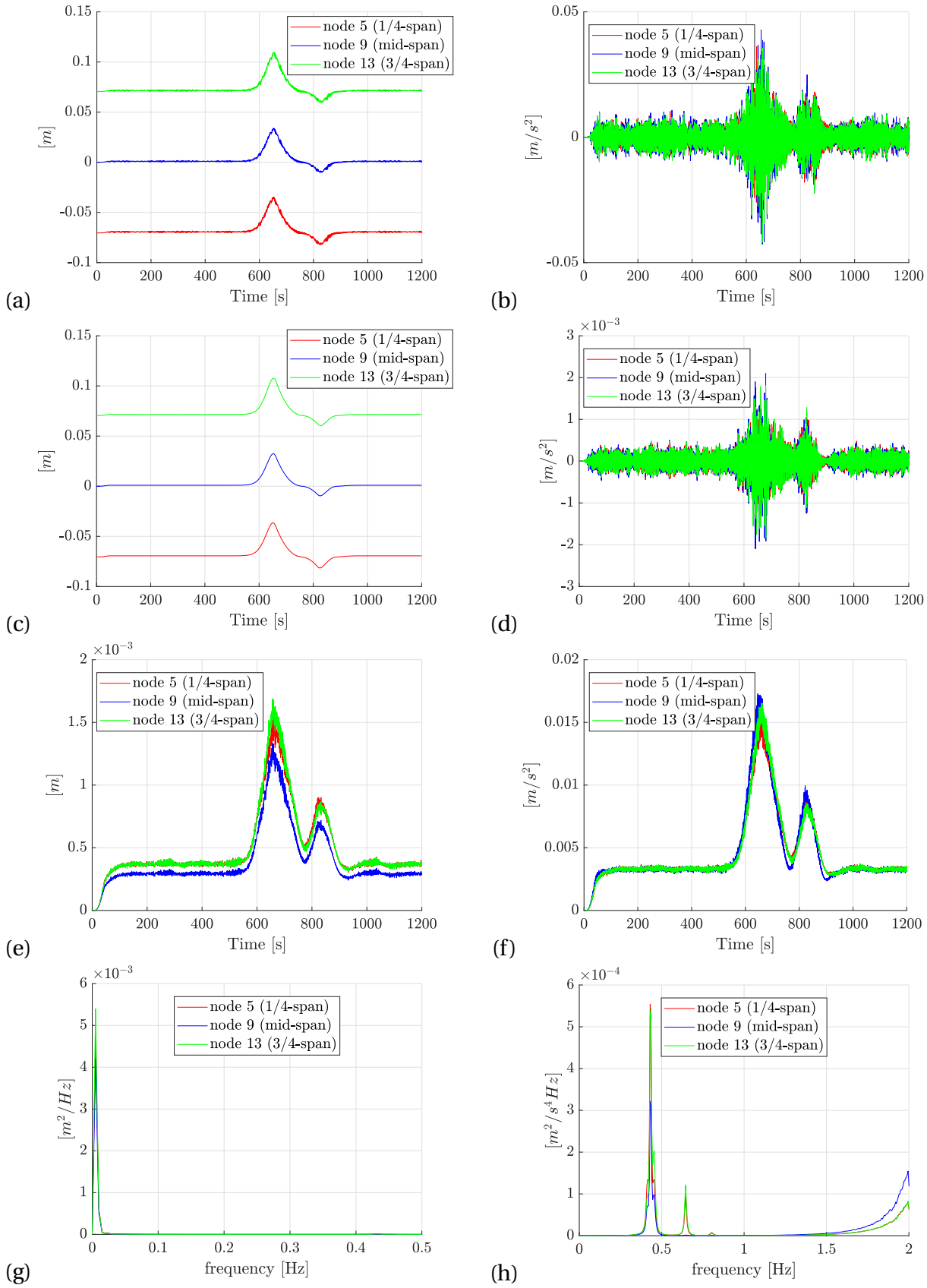

FIGURE 4.16: Statistics about the iced cable response at node 5, 9 and 13 in direction x for a downburst directed from a 45° angle with respect to axis x: (a) Random sample of displacement response, (b) Random sample of acceleration response, (c) Mean of the samples of displacement response, (d) Mean of the samples of acceleration response, (e) Standard deviation of the samples of displacement response, (f) Standard deviation of the samples of acceleration response, (g) PSD of displacement response, (h) PSD of acceleration response.

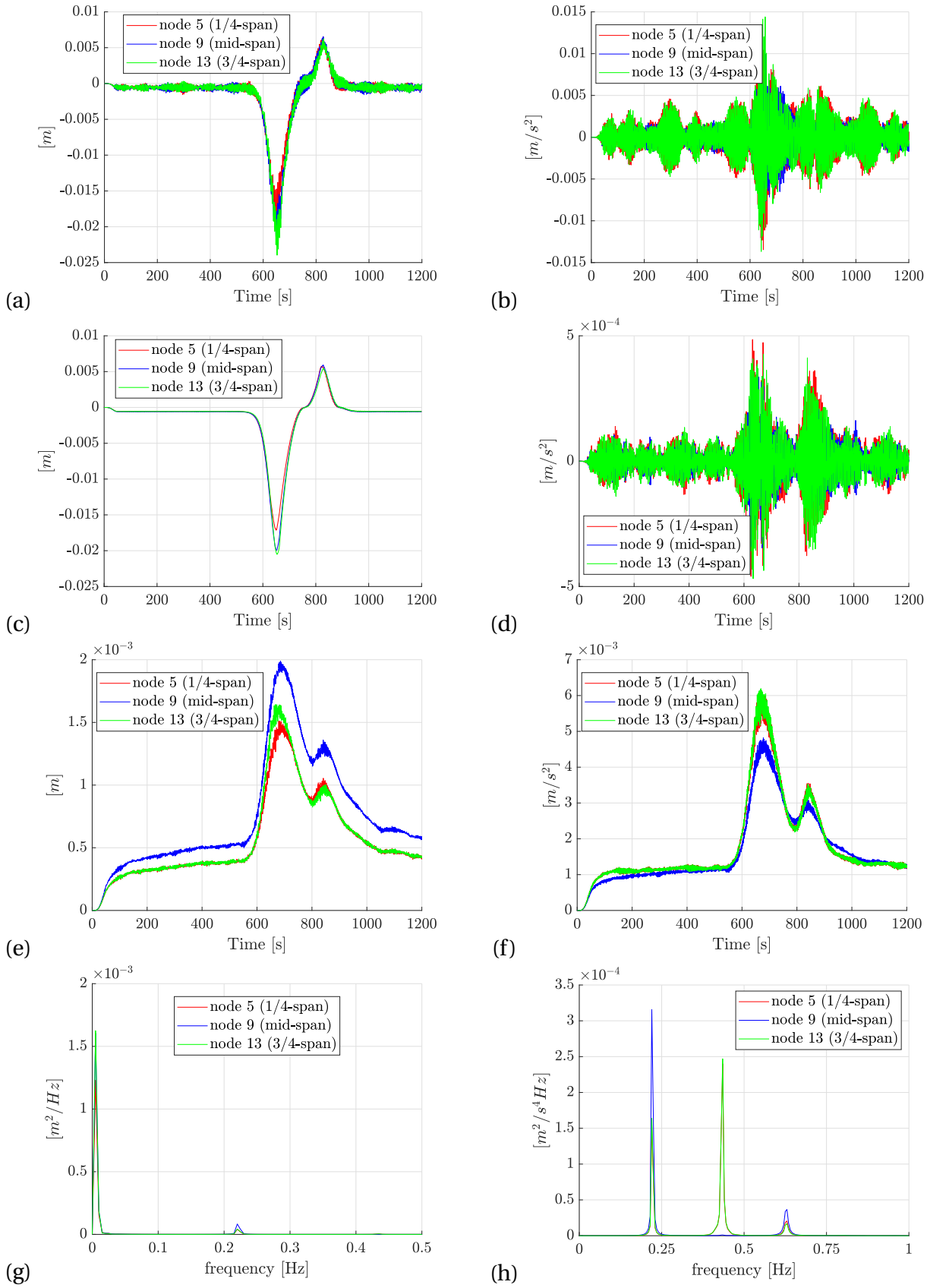

FIGURE 4.17: Statistics about the iced cable response at node 5, 9 and 13 in direction y for a downburst directed from a 45° angle with respect to axis x: (a) Random sample of displacement response, (b) Random sample of acceleration response, (c) Mean of the samples of displacement response, (d) Mean of the samples of acceleration response, (e) Standard deviation of the samples of displacement response, (f) Standard deviation of the samples of acceleration response, (g) PSD of displacement response, (h) PSD of acceleration response.

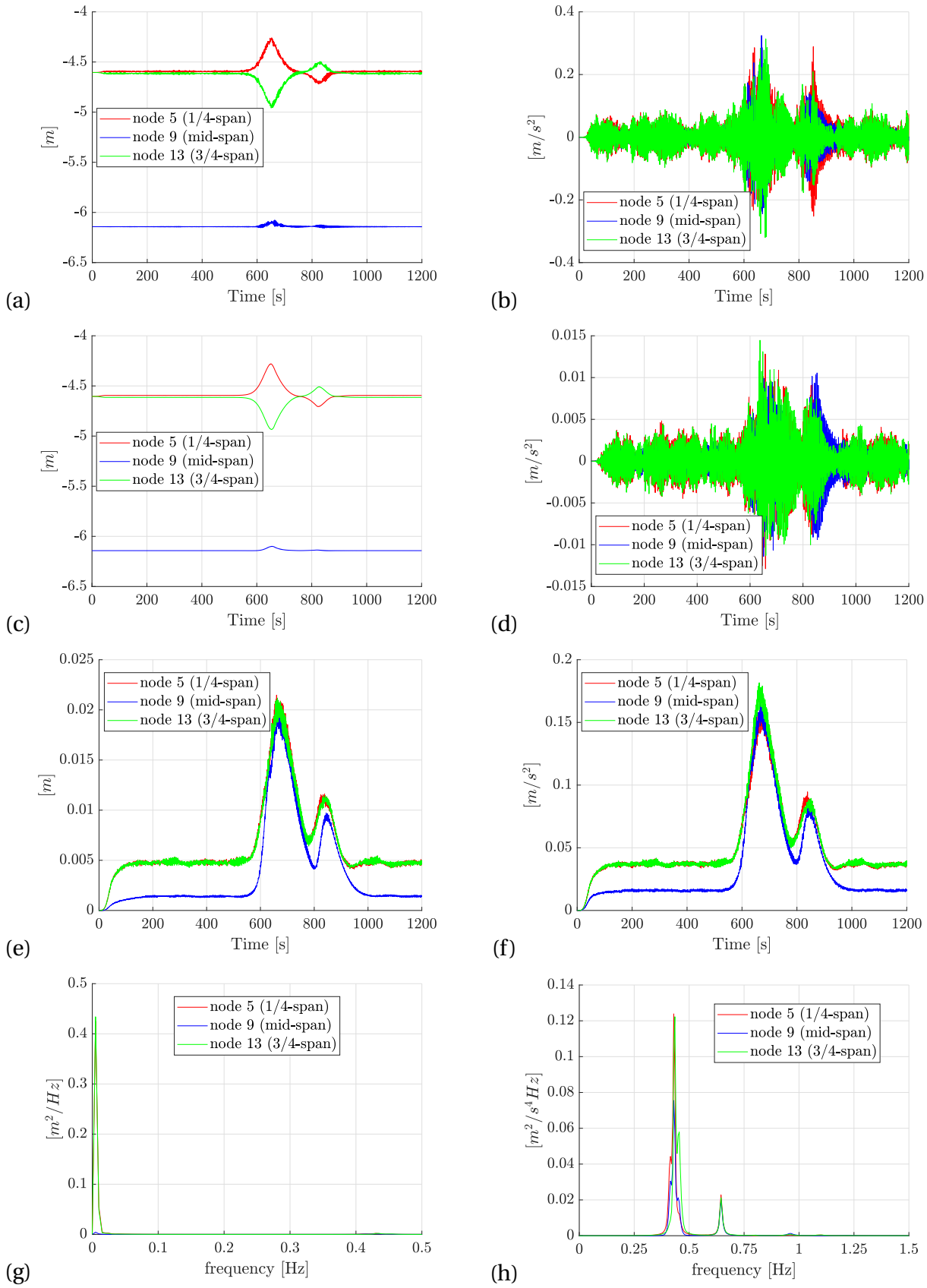

FIGURE 4.18: Statistics about the iced cable response at node 5, 9 and 13 in direction z for a downburst directed from a 45° angle with respect to axis x: (a) Random sample of displacement response, (b) Random sample of acceleration response, (c) Mean of the samples of displacement response, (d) Mean of the samples of acceleration response, (e) Standard deviation of the samples of displacement response, (f) Standard deviation of the samples of acceleration response, (g) PSD of displacement response, (h) PSD of acceleration response.

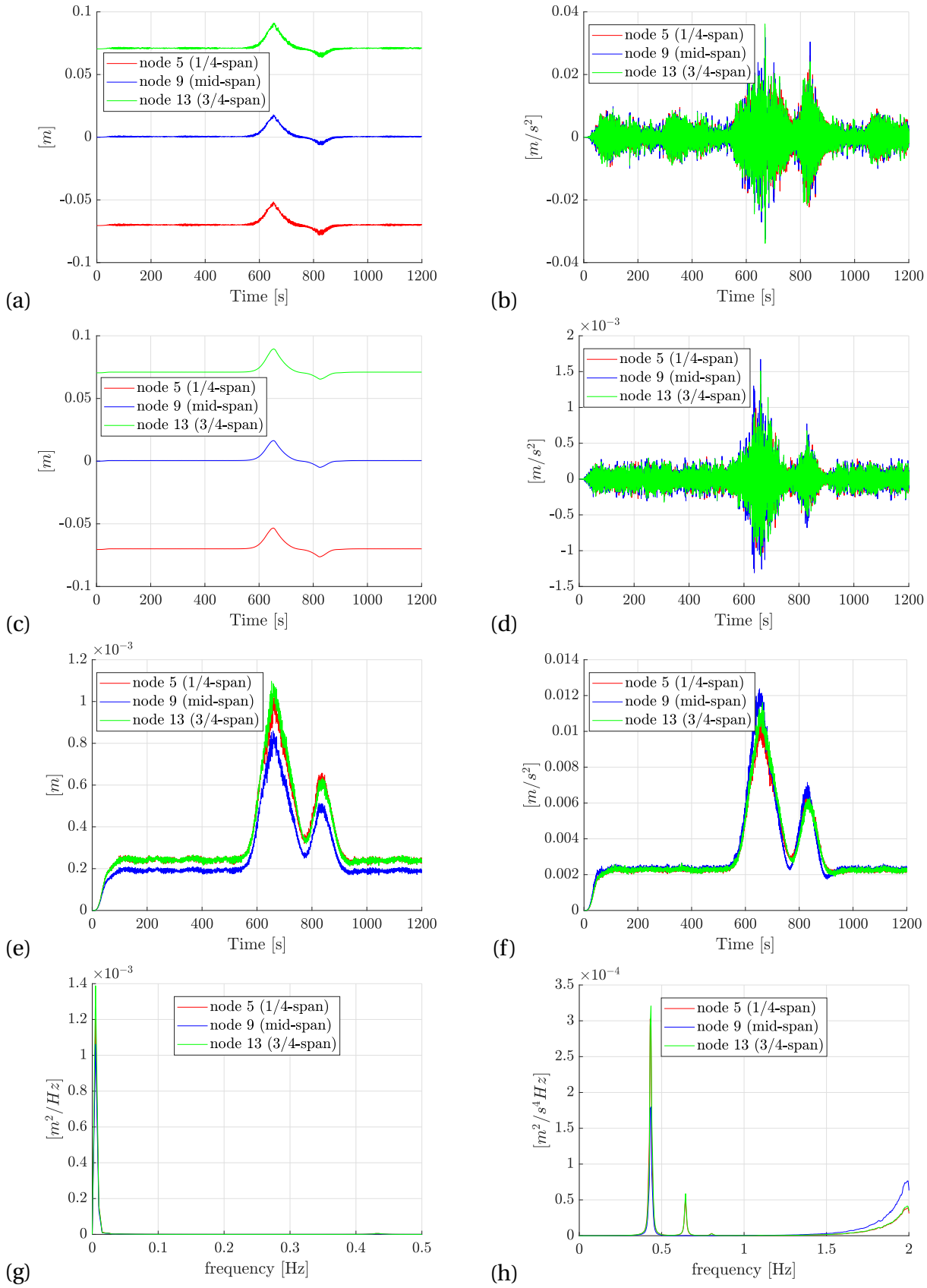

FIGURE 4.19: Statistics about the iced cable response at node 5, 9 and 13 in direction x for a downburst directed from a 60° angle with respect to axis x: (a) Random sample of displacement response, (b) Random sample of acceleration response, (c) Mean of the samples of displacement response, (d) Mean of the samples of acceleration response, (e) Standard deviation of the samples of displacement response, (f) Standard deviation of the samples of acceleration response, (g) PSD of displacement response, (h) PSD of acceleration response.

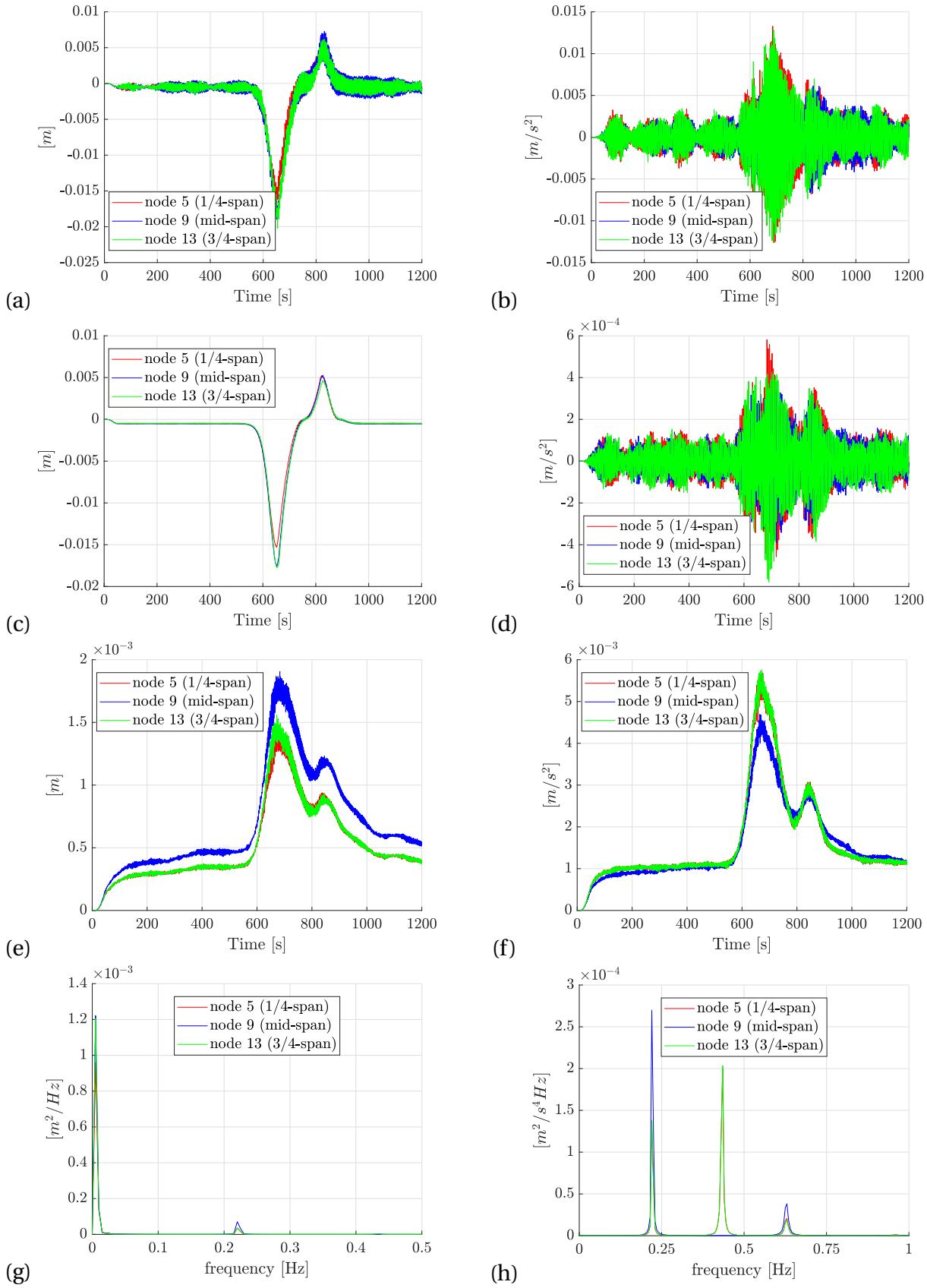

FIGURE 4.20: Statistics about the iced cable response at node 5, 9 and 13 in direction y for a downburst directed from a 60° angle with respect to axis x: (a) Random sample of displacement response, (b) Random sample of acceleration response, (c) Mean of the samples of displacement response, (d) Mean of the samples of acceleration response, (e) Standard deviation of the samples of displacement response, (f) Standard deviation of the samples of acceleration response, (g) PSD of displacement response, (h) PSD of acceleration response.

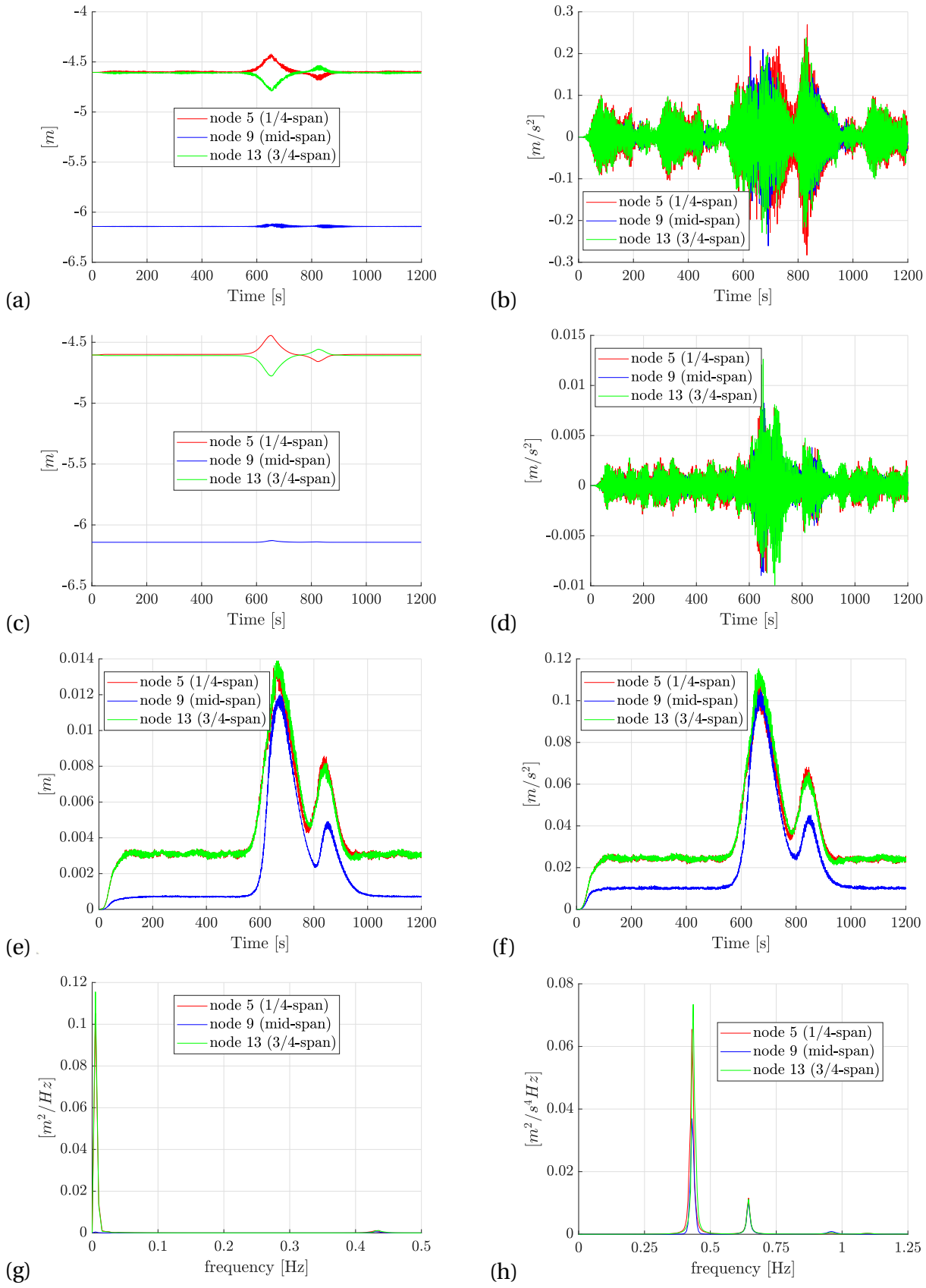

FIGURE 4.21: Statistics about the iced cable response at node 5, 9 and 13 in direction z for a downburst directed from a 60° angle with respect to axis x: (a) Random sample of displacement response, (b) Random sample of acceleration response, (c) Mean of the samples of displacement response, (d) Mean of the samples of acceleration response, (e) Standard deviation of the samples of displacement response, (f) Standard deviation of the samples of acceleration response, (g) PSD of displacement response, (h) PSD of acceleration response.

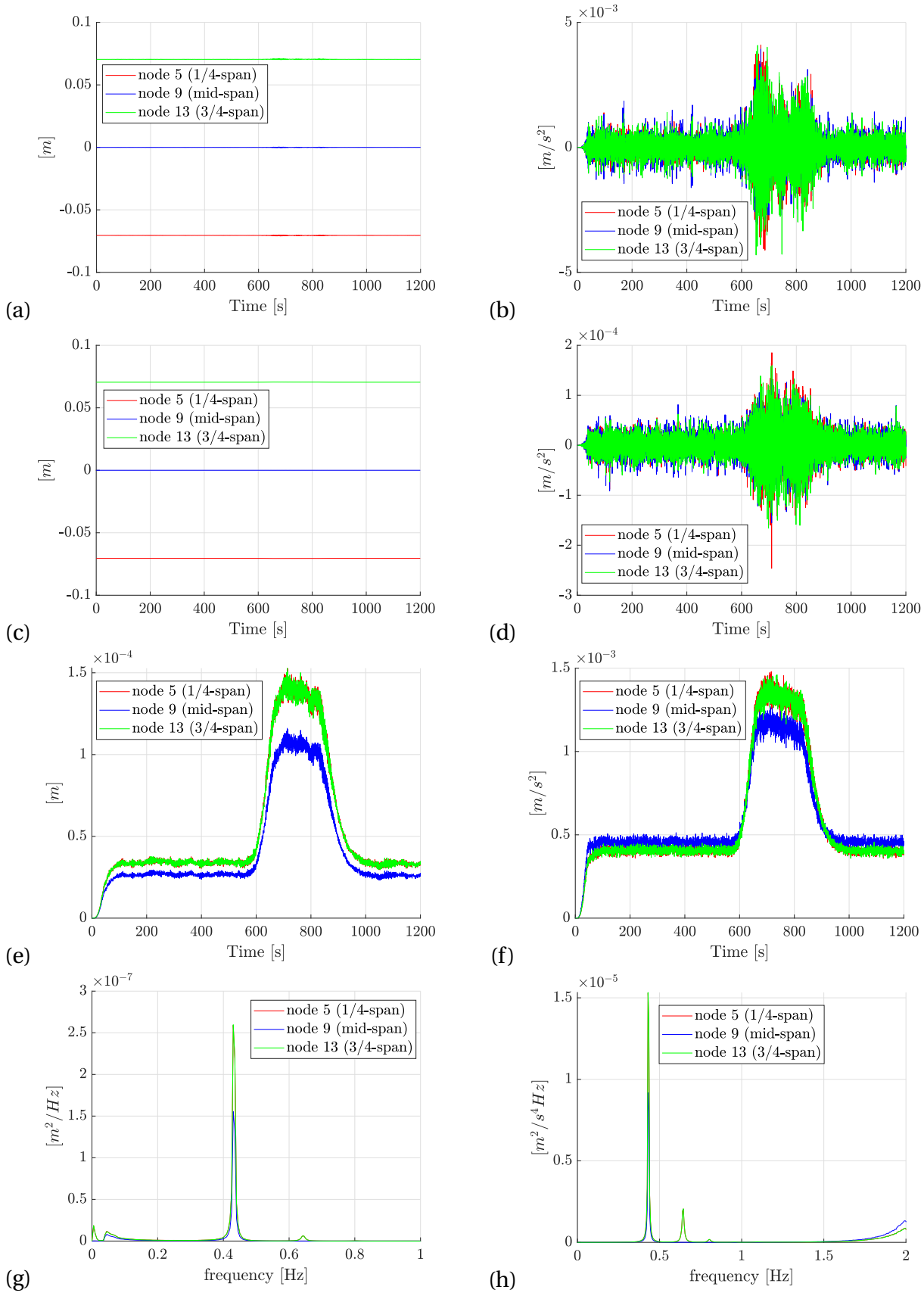

FIGURE 4.22: Statistics about the iced cable response at node 5, 9 and 13 in direction x for a downburst directed from a 90° angle with respect to axis x: (a) Random sample of displacement response, (b) Random sample of acceleration response, (c) Mean of the samples of displacement response, (d) Mean of the samples of acceleration response, (e) Standard deviation of the samples of displacement response, (f) Standard deviation of the samples of acceleration response, (g) PSD of displacement response, (h) PSD of acceleration response.

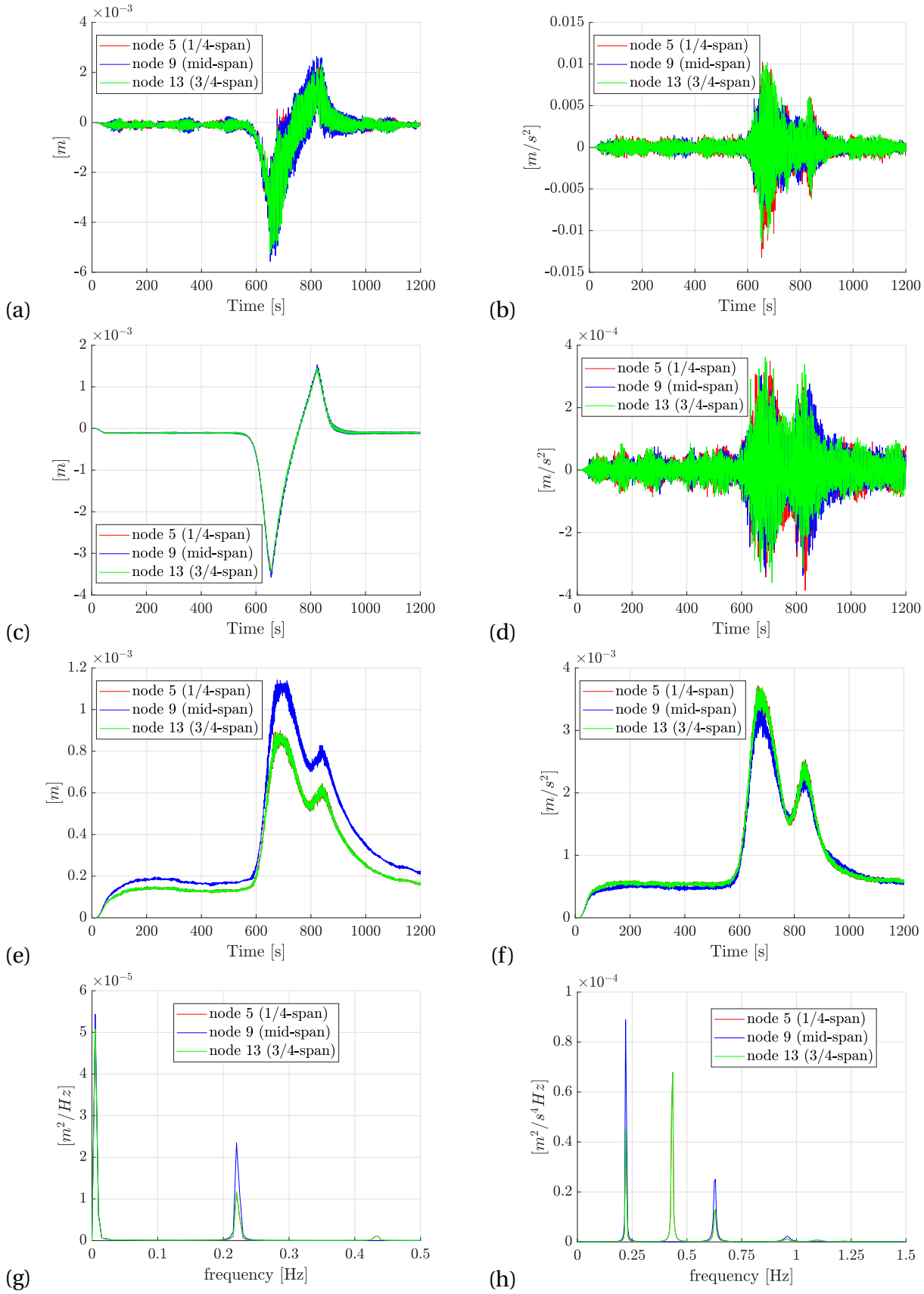

FIGURE 4.23: Statistics about the iced cable response at node 5, 9 and 13 in direction y for a downburst directed from a 90° angle with respect to axis x: (a) Random sample of displacement response, (b) Random sample of acceleration response, (c) Mean of the samples of displacement response, (d) Mean of the samples of acceleration response, (e) Standard deviation of the samples of displacement response, (f) Standard deviation of the samples of acceleration response, (g) PSD of displacement response, (h) PSD of acceleration response.

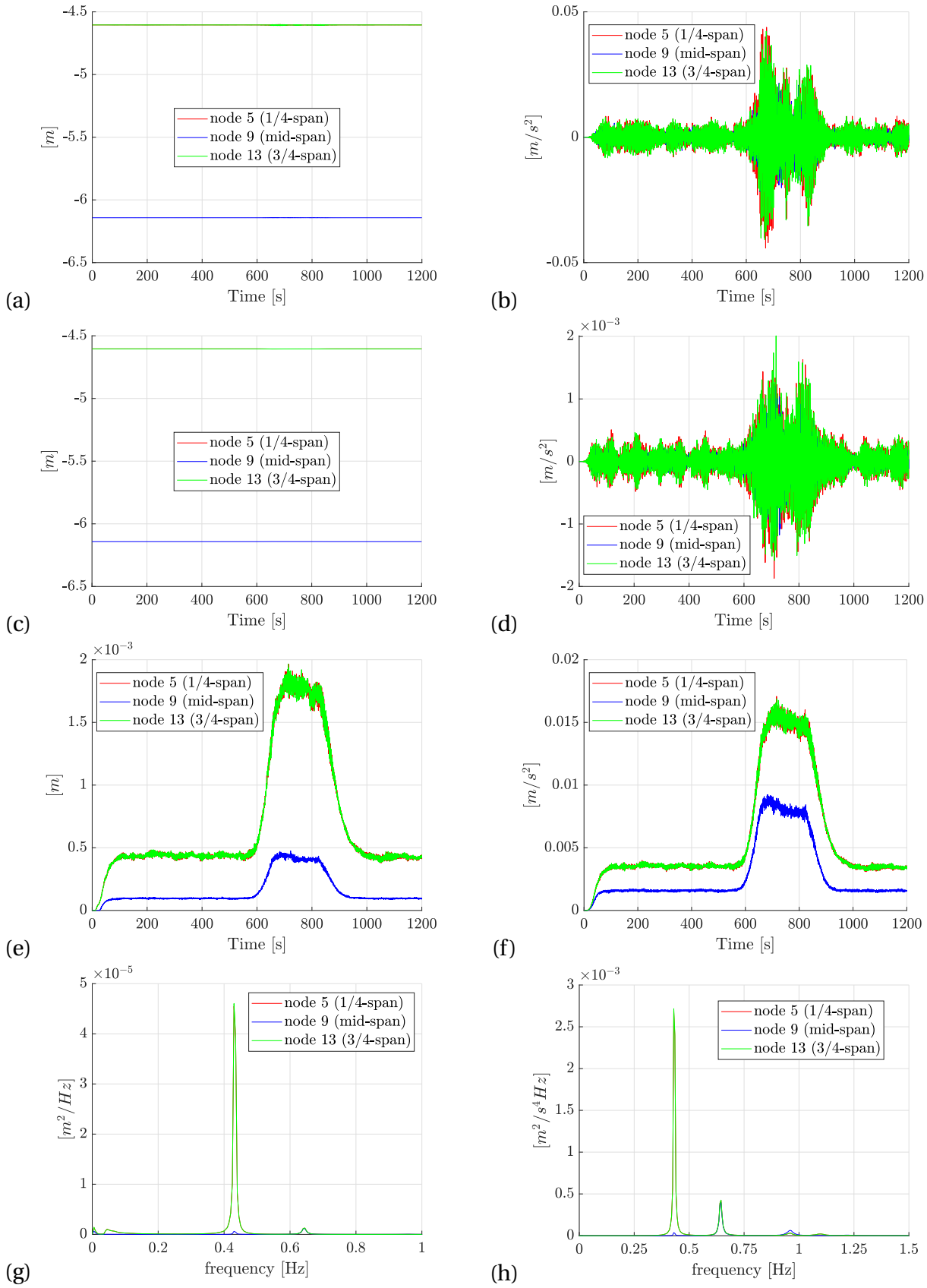

FIGURE 4.24: Statistics about the iced cable response at node 5, 9 and 13 in direction z for a downburst directed from a 90° angle with respect to axis x: (a) Random sample of displacement response, (b) Random sample of acceleration response, (c) Mean of the samples of displacement response, (d) Mean of the samples of acceleration response, (e) Standard deviation of the samples of displacement response, (f) Standard deviation of the samples of acceleration response, (g) PSD of displacement response, (h) PSD of acceleration response.

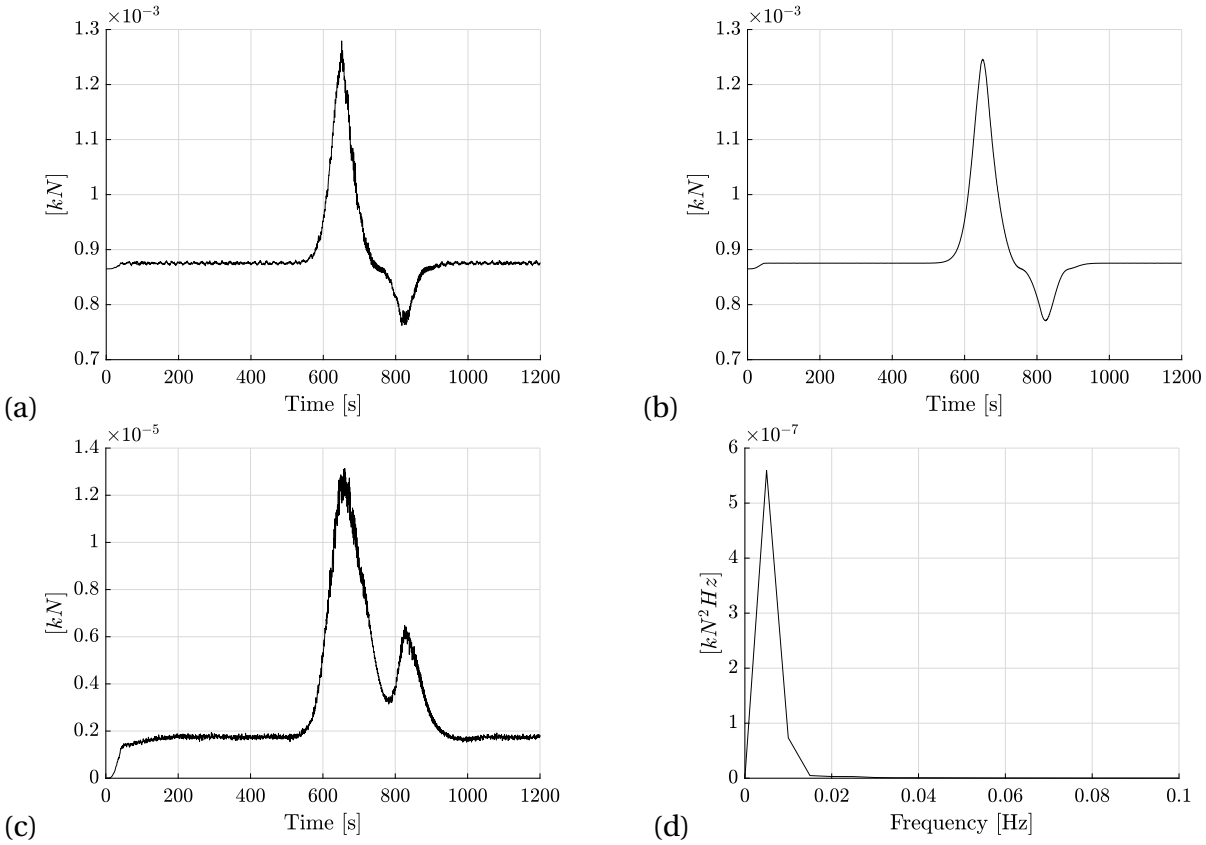

FIGURE 4.25: Statistics about the iced cable response in terms of tension in the cable for a downburst directed from a 0° angle with respect to axis x: (a) Random sample of tension response, (b) Mean of the samples of tension response, (c) Standard deviation of the samples of tension response, (d) PSD of the tension response.

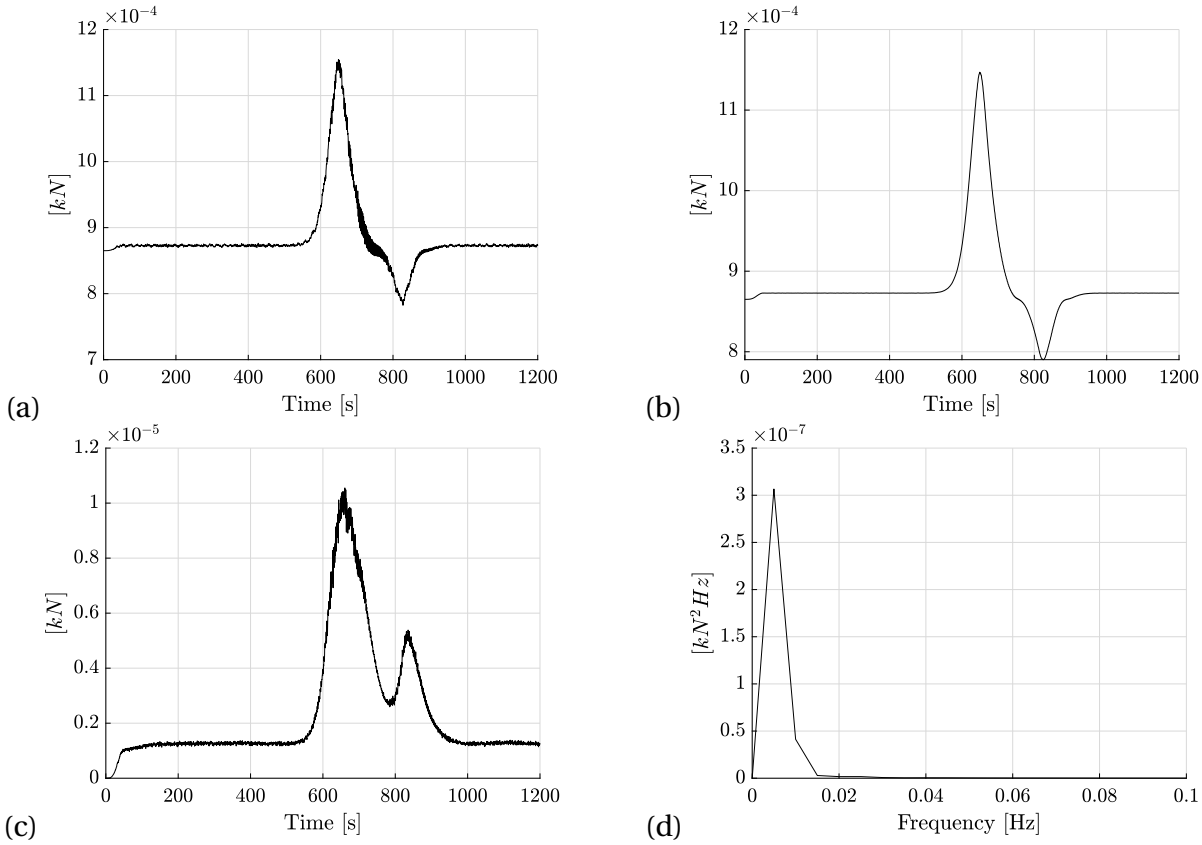

FIGURE 4.26: Statistics about the iced cable response in terms of tension in the cable for a downburst directed from a 30° angle with respect to axis x: (a) Random sample of tension response, (b) Mean of the samples of tension response, (c) Standard deviation of the samples of tension response, (d) PSD of the tension response.

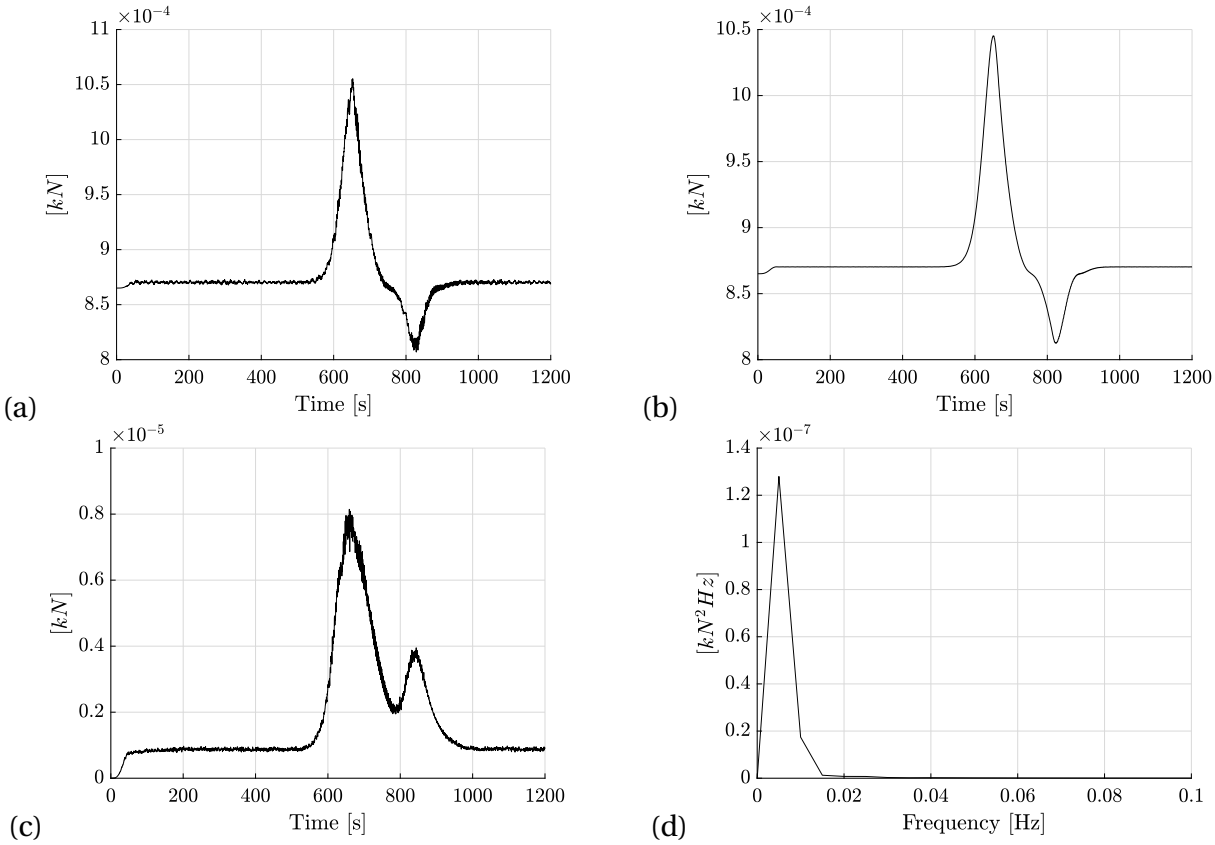

FIGURE 4.27: Statistics about the iced cable response in terms of tension in the cable for a downburst directed from a 45° angle with respect to axis x: (a) Random sample of tension response, (b) Mean of the samples of tension response, (c) Standard deviation of the samples of tension response, (d) PSD of the tension response.

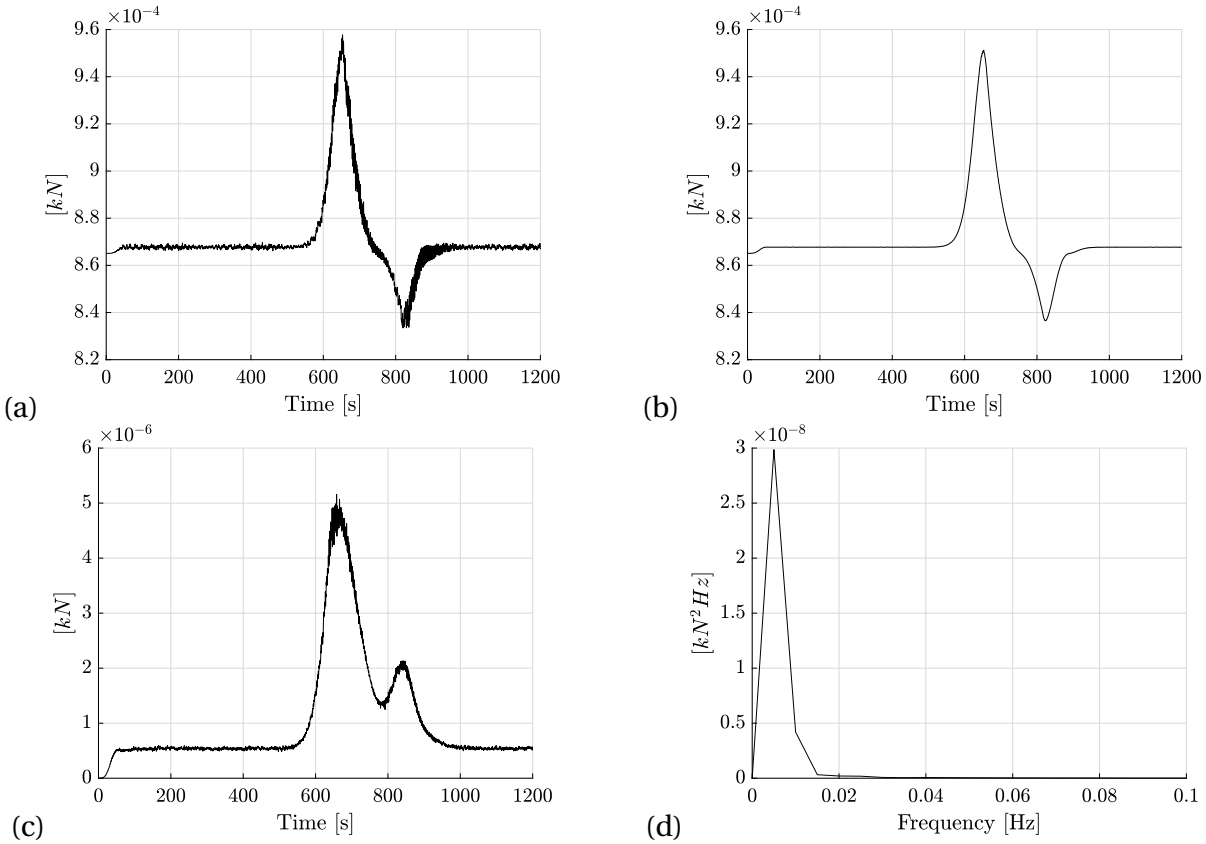

FIGURE 4.28: Statistics about the iced cable response in terms of tension in the cable for a downburst directed from a 60° angle with respect to axis x: (a) Random sample of tension response, (b) Mean of the samples of tension response, (c) Standard deviation of the samples of tension response, (d) PSD of the tension response.

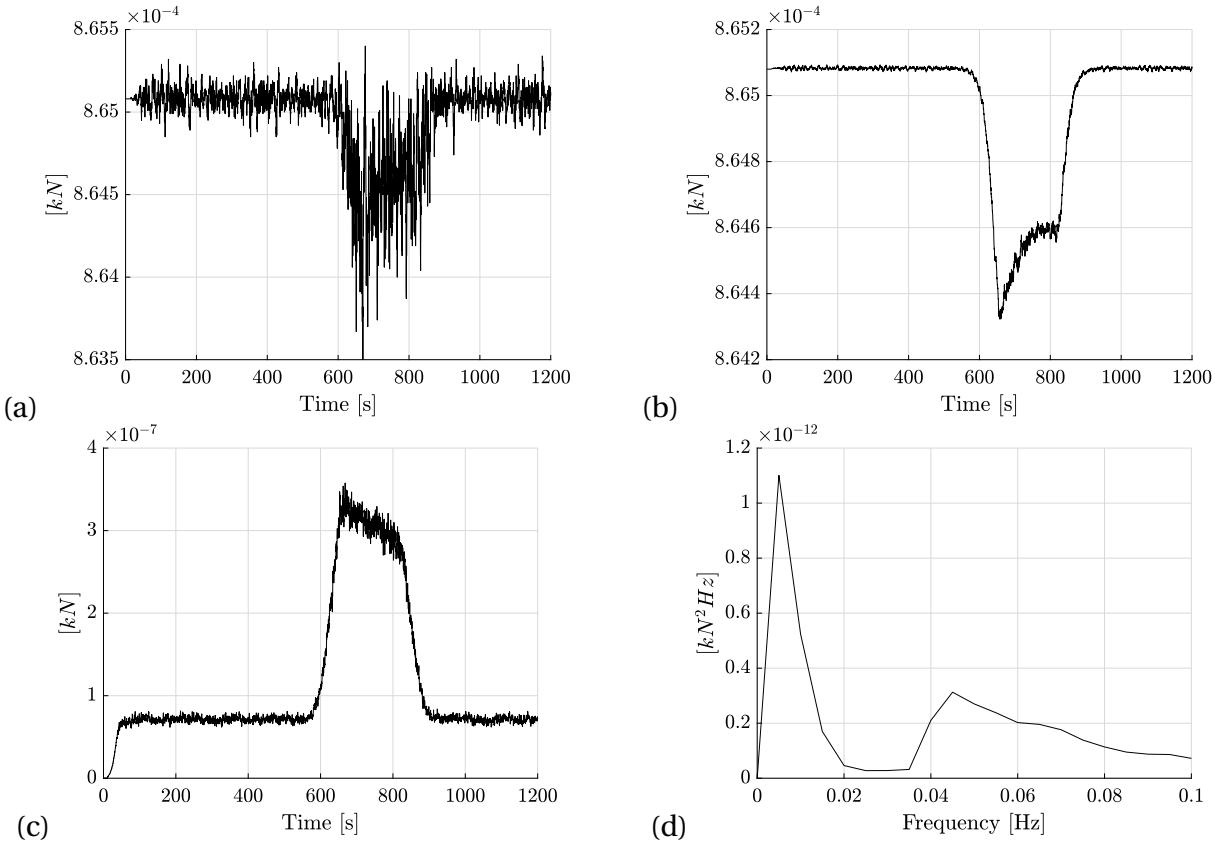

FIGURE 4.29: Statistics about the iced cable response in terms of tension in the cable for a downburst directed from a 90° angle with respect to axis x: (a) Random sample of tension response, (b) Mean of the samples of tension response, (c) Standard deviation of the samples of tension response, (d) PSD of the tension response.

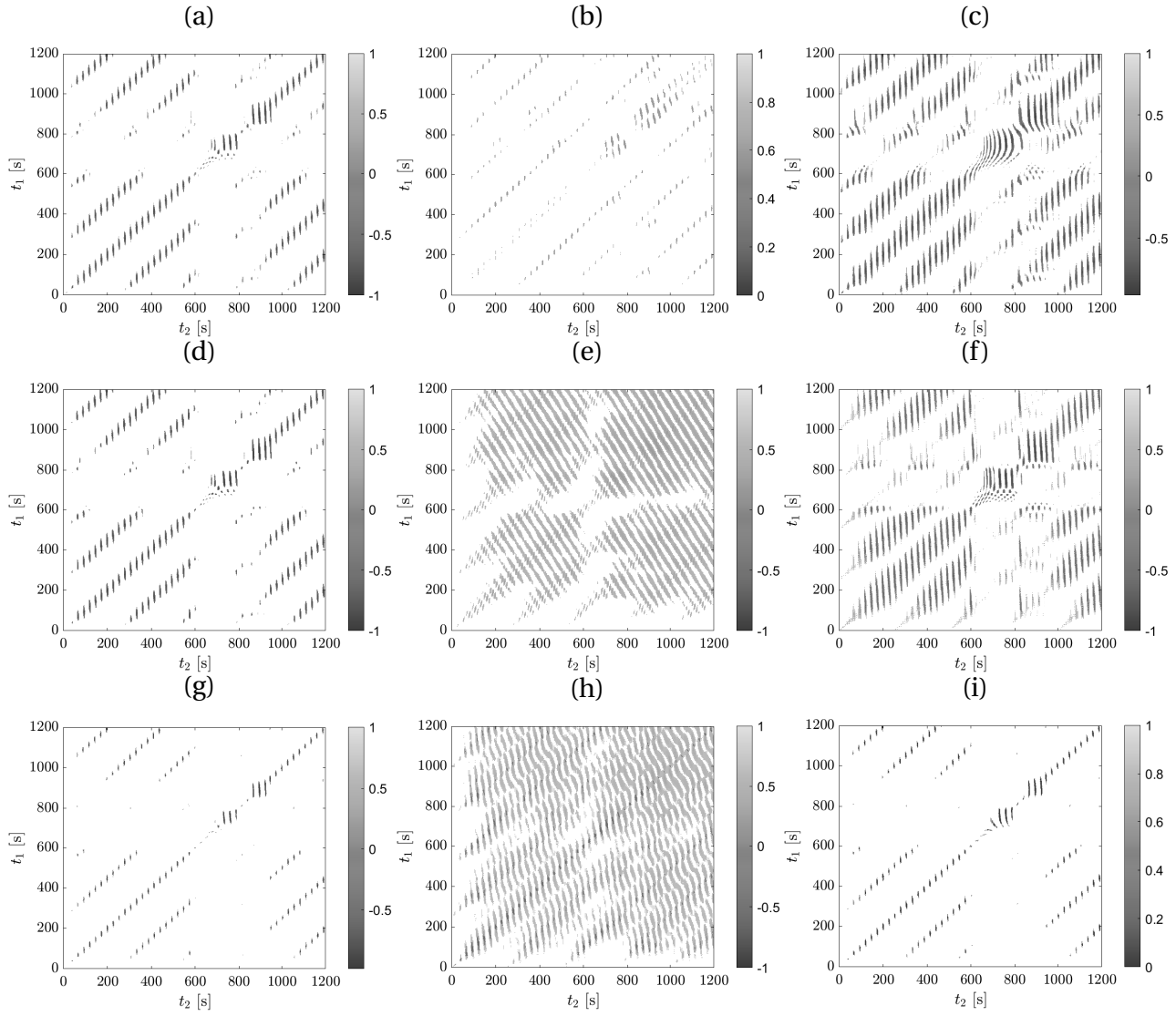

FIGURE 4.30: Correlation coefficient values of the acceleration repsonse of the iced cable in the time domain for 0°downburst trajectory: (a) at node 5 (1/4 span) in direction x, (b) at node 5 (1/4 span) direction y, (c) at node 5 (1/4 span) direction z, (d) at node 9 (half span) in direction x, (e) at node 9 (half span) direction y, (f) at node 9 (half span) direction z, (g) at node 13 (3/4 span) in direction x, (h) at node 13 (3/4 span) direction y, (i) at node 13 (3/4 span) direction z.

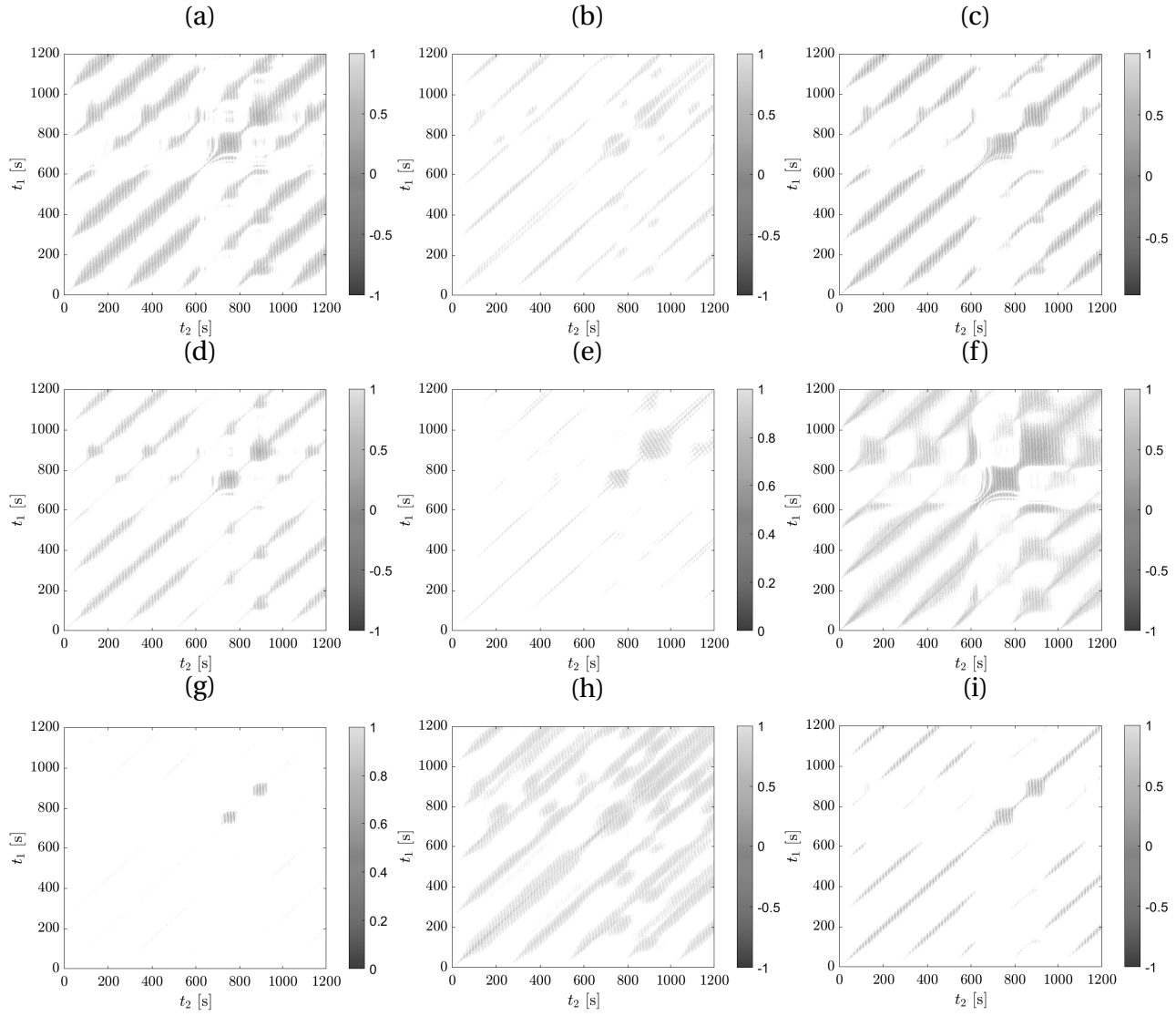

FIGURE 4.31: Correlation coefficient values of the acceleration repsonse of the iced cable in the time domain for 45°downburst trajectory: (a) at node 5 (1/4 span) in direction x, (b) at node 5 (1/4 span) direction y, (c) at node 5 (1/4 span) direction z, (d) at node 9 (half span) in direction x, (e) at node 9 (half span) direction y, (f) at node 9 (half span) direction z, (g) at node 13 (3/4 span) in direction x, (h) at node 13 (3/4 span) direction y, (i) at node 13 (3/4 span) direction z.

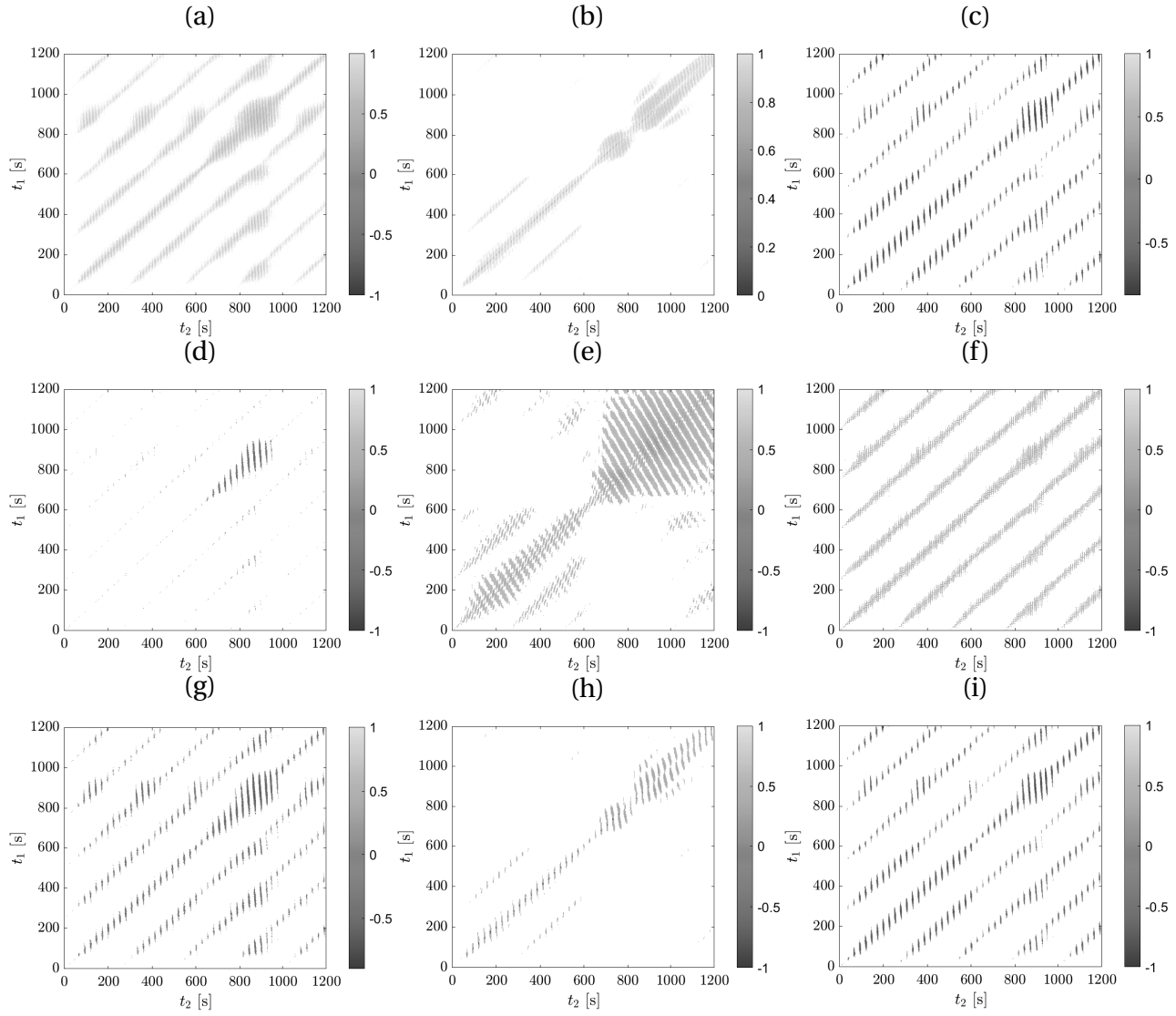

FIGURE 4.32: Correlation coefficient values of the acceleration response of the iced cable in the time domain for 90°downburst trajectory: (a) at node 5 (1/4 span) in direction x, (b) at node 5 (1/4 span) direction y, (c) at node 5 (1/4 span) direction z, (d) at node 9 (half span) in direction x, (e) at node 9 (half span) direction y, (f) at node 9 (half span) direction z, (g) at node 13 (3/4 span) in direction x, (h) at node 13 (3/4 span) direction y, (i) at node 13 (3/4 span) direction z.

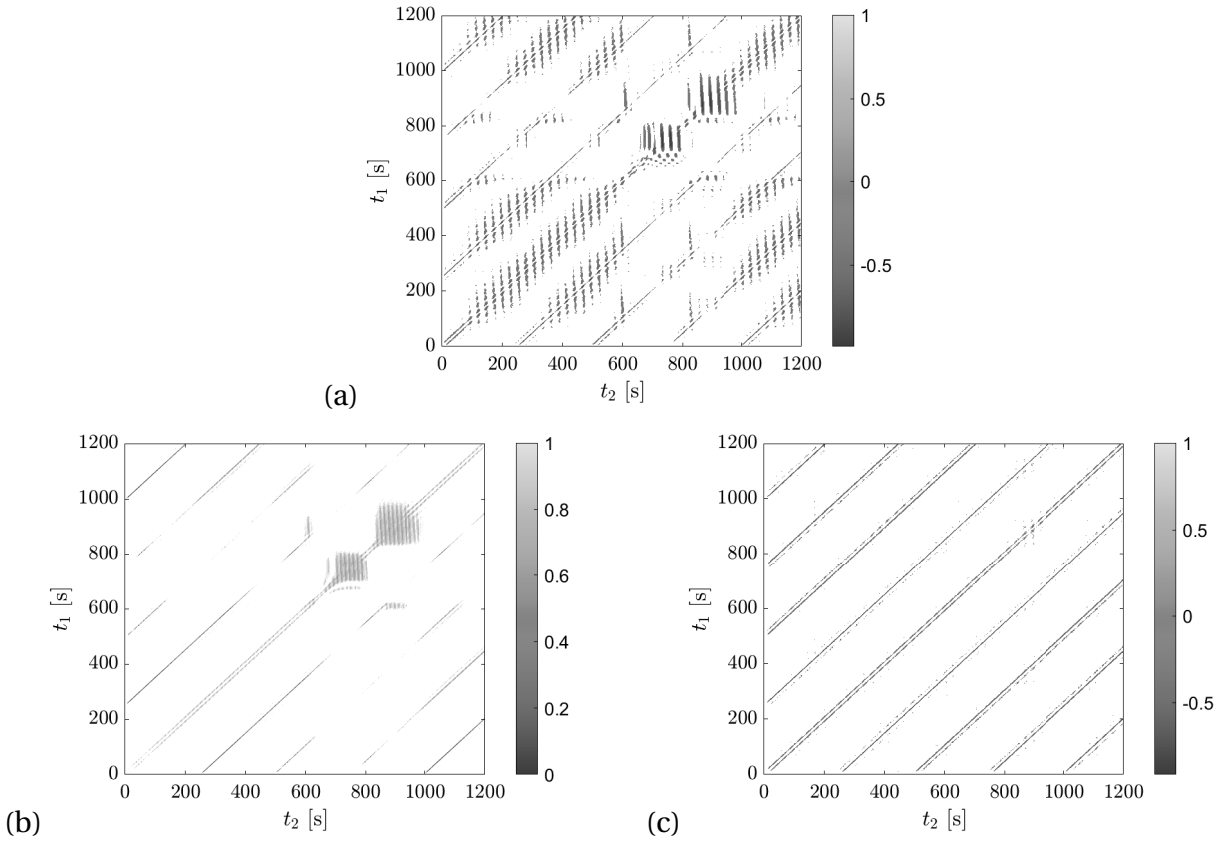

FIGURE 4.33: Correlation coefficient values of the cable tension in the time domain: (a) for 0°downburst trajectory, (b) for 45°downburst trajectory, (c) for 90°downburst trajectory.

CHAPTER

5 Conclusions

The problematic which led to this work is the damaging effects of downburst on flexible structures and in particular on the transmission lines. That identifies a need of understanding of the transient nature of downburst in order to be allowed to model it precisely. Once the wind field of downburst is modelled, it still remains to apply the downburst solicitation to a structure.

In this work, a new approach of downburst modelling was employed. It consists in decomposing the total wind velocity of downburst into a background wind component independent of the downburst phenomenon and that is assumed to be a synoptic wind which is well established on the contrary of downburst wind. This background component allows to explain physically the evolution in time of the vertical wind velocity profile shape with the synoptic profile appearing as the downburst goes far from the observation point and conversely. However, the turbulence linked to the downburst is not yet standardised and therefore it has not been included in the model. Nevertheless, an approach to generate such a turbulence consisting in the use of an existing PSD of radial turbulence from downburst recordings is proposed.

The new model of downburst was then adapted to fit with the Andrews A.F.B. downburst data recordings and the results were quite similar except for the turbulence component due to the neglecting of the downburst turbulence. Next, a parametric study was performed to evaluate the influence of reference velocity of the background wind and the downburst scale parameters on the wind velocity time histories. The first of these parameters influenced the wind velocity mainly at time instants where downburst is far. Concerning the scale parameters, they influenced the wind velocity peaks distribution in time and also their intensity. Finally, different trajectories of downburst were studied relative to an horizontal set of observers (such as a cable structure. This study showed that a trajectory perpendicular and parallel to the horizontal set of observers are critical in terms of wind velocity engendered respectively in the transverse direction to the set of observes and in the direction of the longitudinal axis of the observers.

The downburst wind field modelled using the new approach was then applied to 2 types of structures: the CAARC vertical building and an iced cable. The combination of such structural responses could be helping the following researches aiming to predict the structural response of transmission lines to downburst. The appliance of the wind field to the structures was made by

the intermediate of a non-linear finite element method necessary because of the non-linearity induced by the flexible structures studied.

Response of CAARC building to the Andrews A.F.B. downburst simulated can be considered as quasi-static especially in the mean direction of the wind. Although, it is worth keeping in mind that the downburst turbulence was not modelled in the new approach brought in this work.

Response of iced-cable is analysed in terms of statistics data collected from the structural responses of 500 random samples of synoptic background turbulence generation. From that, in addition of the standard deviation, the mean and the PSD, the correlation coefficients can be retrieved for displacement, acceleration and tension in the cable responses. This allows to separate the quasi-static structural response from the dynamic response which results in simplification of the model. In addition, the statistics have been performed for different trajectories of downburst in order to identify the critical cases depending on the direction of interest.

Finally, this model applied to vertical and cable structures aims to be improved in the future with the addition of the downburst turbulence modelling and also the application to an entire transmission line structure.

Bibliography

Alminhana, G., Braun, A., and Loredo-Souza, A. (2018). *A numerical-experimental investigation on the aerodynamic performance of CAARC building models with geometric modifications.* Journal of Wind Engineering & Industrial Aerodynamics 180: 34–48.

ASCE (2005). *ASCE 7-05: Minimum Design Loads for Buildings and Other Structures.* American Society of Civil Engineers.

Braun, A. L. and Awruch, A. M. (2009). *Aerodynamic and aeroelastic analyses on the CAARC standard tall building model using numerical simulation.* Computers and Structures 87: 564–581.

Canor, T., Caracoglia, L., and Denoël, V. (2016). *Perturbation methods in evolutionary spectral analysis for linear dynamics and equivalent statistical linearization.* Probabilistic Engineering Mechanics 46: 1–17.

Chen, L. and Letchford, C. W. (2004a). *A deterministic–stochastic hybrid model of downbursts and its impact on a cantilevered structure.* Engineering Structures 26: 619-629.

Chen, L. and Letchford, C. W. (2004b). *Parametric study on the along-wind response of the CAARC building to downbursts in the time domain.* Journal of Wind Engineering & Industrial Aerodynamics 92: 703–724.

Di Paola, M. and Gullo, I. (2001). *Digital generation of multivariate wind field processes.* Probabilistic Engineering Mechanics 16: 1–10.

Foti, F. and Martinelli, L. (2018a). *Finite element modeling of cable galloping vibrations. Part II: Application to an iced cable in 1:2 multiple internal resonance.* Journal of Vibration and Control 24(7): 1322-1340.

Foti, F. and Martinelli, L. (2018b). *Finite element modeling of cable galloping vibrations—Part I: Formulation of mechanical and aerodynamic co-rotational elements.* Archive of Applied Mechanics 88:645–670.

Fujita, T. (1985). *Downburst: microburst and macroburst.* University of Chicago Press.

Fujita, T. (1990). *Downburst: Meteorological features and wind field characteristics.* Journal of Wind Engineering & Industrial Aerodynamics 36:75-86.

Haines, M. and Taylor, I. (2019). *The turbulence modelling of a pulsed impinging jet using LES and a divergence free mass flux corrected turbulent inlet.* Journal of Wind Engineering & Industrial Aerodynamics 188: 338–364.

Hangan, H., Refan, M., Jubayer, C., Romanic, D., Parvu, D., LoTufo, J., and Costache, A. (2017). *Novel techniques in wind engineering.* Journal of Wind Engineering & Industrial Aerodynamics 171: 12-33.

Hawes, H. and Dempsey, D. (1993). *Review of recent Australian transmission line failures due to high intensity winds.* Proceedings of the task force of high intensity winds on transmission lines.

Hjelmfelt, M. R. (1987). *Structure and Life Cycle of Microburst Outflows Observed in Colorado.* Journal of Applied Meteorology 27: 900-927.

Holmes, J. D. and Oliver, S. E. (2000). *An empirical model of a downburst.* Engineering Structures 22: 1167–1172.

Kwon, D.-K. and Kareem, A. (2007). *Gust-front factor: A new framework for the analysis of wind load effects in gust-fronts.* Proc., 12th Int. Conf. on Wind Engineering: 767–774.

Kwon, D.-K. and Kareem, A. (2009). *Gust-Front Factor: New Framework for Wind Load Effects on Structures.* Journal of Structural Engineering 135(6): 717-732.

Le, T.-H. and Caracoglia, L. (2017). *Computer-based model for the transient dynamics of a tall building during digitally simulated Andrews AFB thunderstorm.* Computers and Structures 193: 44-72.

Li, C. (1993). *A stochastic model of severe thunderstorms for transmission line design.* Probabilistic Engineering Mechanics 15(4): 359-364.

Lin, W. E., Orf, L. G., Savory, E., and Novacco, C. (2007). *Improved modelling of downburst outflows for wind engineering applications using a cooling source approach.* Wind and Structures 10,no4 : 315-346.

Mason, M. S., Graeme, S. W., and Fletcher, D. F. (2009). *Numerical simulation of downburst winds.* Journal of Wind Engineering & Industrial Aerodynamics 97: 523-539.

McCarthy, P. and M, M. (1996). *Severe weather elements associated with September 5, 1996 hydro tower failures near Grosse Isle. Manitoba, Canada.* Environmental Service Centre, Environment Canada: 21.

Oseguera, R. and Bowles, R. (1988). *A simple analytic 3-dimensional downburst model based on boundary layer stagnation flow.* NASA Technical Memorandum 100632.

Selvam, R. P. and Holmes, J. D. (1992). *Numerical simulation of thunderstorm downdrafts.* Journal of Wind Engineering & Industrial Aerodynamics 41-44: 2817-2825.

Shinozuka, M. and Deodatis, G. (1991). *Simulation of stochastic process by Spectral Representation.* Applied Mechanics reviews 44: 191-204.

Solari, G. (1987). *TURBULENCE MODELING FOR GUST LOADING.* Journal of Structural Engineering 113:1550-1569.

Solari, G., De Gaetano, P., and Repetto, M. P. (2015). *Thunderstorm response spectrum: Fundamentals and case study.* Journal of Wind Engineering & Industrial Aerodynamics 143: 62-77.

Solari, G. and Piccardo, G. (2001). *Probabilistic 3-D turbulence modeling for gust buffeting of structures.* Probabilistic Engineering Mechanics 16: 73-86.

Solari, G., Rainisio, D., and De Gaetano, P. (2017). *Hybrid simulation of thunderstorm outflows and wind excited response of structures.* Meccanica 52, Issue 13, 3197–3220.

Vermeire, B. C., Orf, L. G., and Savory, E. (2011). *Improved modelling of downburst outflows for wind engineering applications using a cooling source approach.* Journal of Wind Engineering & Industrial Aerodynamics 99: 801–814.

Vicroy, D. (1998). *Assessment of microburst models for downdraft estimation.* Journal of Aircraft 29.

Von Karman, T. (1948). *Progress in the statistical theory of turbulence.* Proc Natl Acad Sci USA 34:530–9.

Wood, G. and Kwok, K. (1998). *An empirically derived estimate for the mean velocity profile of a thunderstorm downburst.* 7th AWES Workshop.

Zhang, S., Solari, G., Burlando, M., and Yang, Q. (2019). *Directional decomposition and properties of thunderstorm outflows.* Journal of Wind Engineering & Industrial Aerodynamics 189: 71–90.

Zhang, Y. (1993). *Status quo of wind hazard prevention for transmission lines and countermeasures.* East China Electr Power 34(3): 28-31.

Zhang, Y., Hu, H., and Sarkar, P. P. (2013). *Modeling of microburst outflows using impinging jet and cooling source approaches and their comparison.* Engineering Structures 56: 779-793.